DEVELOPMENT OF A TEST SECTION FEATURING A FLAT PLATE CONDITIONED FOR THE STUDY OF FULLY DEVELOPED TURBULENT BOUNDARY LAYERS USING PIV

BY

JOSE RODRIGUEZ

THESIS

Submitted in partial fulfillment of the requirements
for the degree of Master of Science in Aerospace Engineering
in the Graduate College of the
University of Illinois at Urbana-Champaign, 2020

Urbana, Illinois

Adviser:

Assistant Professor Theresa Saxton-Fox

ABSTRACT

The purpose of this thesis is to describe the logic behind the extension of a test section in a facility that was designed for studying fully developed turbulent boundary layers in wall-bounded flow, primarily using Particle Image Velocimetry (PIV). The initial section will focus on providing motivation of why it can be of interest to study turbulence. The following section will provide a historical context of the development of the Navier-Stokes equations which attempt to mathematically model the behavior of fluid elements from a microscale. These fundamental equations will then get expanded to demonstrate how they fit with the modern look at turbulence. Finally, the rest of the document will build on these historical principles. The bulk of the thesis will cover the design methodology and some experimental data which proved a degree of success after the tunnel was assembled and instrumented. Concerns about stability regarding ensuring a structurally sound TS, and mitigating natural frequencies will be addressed. This will then be followed by plans for future experiments and some recommendations regarding areas of improvement.

ACKNOWLEDGEMENTS

While trying to connect the different stages of the evolution on the concept of Turbulent Flow, particularly in the introduction, a quote from Isaac Newton kept coming to mind, ”If I have seen further it is by standing on the shoulders of Giants.” Sure, Isaac Newton had a brilliant mathematical mind, but I do not feel this quote is limited to technical subjects. Giants in our lives can be the people that are there for us in a technical and non-technical setting. These people are able to help us stay sane, but most importantly happy and that enables us to grow and learn.

On that note, I want to thank Professor Theresa Saxton-Fox for all of her help through my time here at Illinois. It was a great experience being her first graduate student, and we both learned a great amount. We were both able to start the group together, and created a facility that seems promising. I am very excited to see the amazing experiments and papers that will come from it. I am very happy and glad you were my advisor.

Throughout my time in Illinois, right from the beginning I had mentors that eased my transition to graduate school in addition to Professor Saxton-Fox. Professor Jason Merret was another person I was fortunate to have met. I will always be grateful to the graduate committee of the Department of Aerospace Engineering at UIUC, for not only allowing me to be admitted to the college, but for providing funding opportunities from the beginning. Special thanks to the Air Force Research Labs, the United States Department of Defense and Dr. Brian Rice for allowing me to explore different areas of research. Dr. Srivathsan Ragunathan also convinced me to pursue an advanced degree, I am really thankful for his guidance.

To my parents, Jose, Laura and my brothers Israel and Dan I will always be grateful for all of the love and care you have shown to me through all these years. Not only did you instill and cultivate moral values, but you also encouraged the desire to keep learning. I have always told people that I learned the value of hard work from my Father, and how to love life and be positive about things from my Mother. Without you all, and my extended family I would not have been able to accomplish what I have today.

Alberto, Christiaan, and Mruthun, thank you. However, there are many more people and groups of friends that positively impacted my time here in Illinois and in life, and I apologize for not explicitly mentioning you. Just know that you are also very appreciated.

Table of Contents

List of Figures . . . . . **vi**

List of Tables . . . . . **viii**

Nomenclature . . . . . **ix**

1 Introduction **1**

1.1 Brief Development of the Boundary Layer Equations 2

1.2 Foundation of The Canonical View of Turbulence 4

1.2.1 Inner, Outer and Overlap Regions of The TBL 4

1.2.2 Energy Models of The TBL 6

1.3 Modern Visions of Scale Interaction 7

1.3.1 Hairpin Vortices 8

1.3.2 Amplitude Modulation 9

1.3.3 Conditional Averaging 11

1.4 Computational Approaches to Turbulence 12

2 Tunnel Design **14**

2.1 Background on Inherited 0.381x0.381-Meter Wind Tunnel 14

2.2 Efforts to Create a Canonical Turbulent Boundary Layer 15

2.2.1 Length Extension of Inherited Wind Tunnel 15

2.2.2 Importance of Maintaining a Zero Pressure Gradient in The Test Section 19

2.2.3 Effects of Leading Edge Geometry on ZPG and Flow Quality 20

2.2.4 Trailing Edge Design and Stagnation Point Location 24

2.3 Flat Plate Design for Manufacturability and Ease of Modification 25

2.4 Optical Access for PIV 27

2.4.1 General PIV Background 27

2.4.2 Optical Material Considerations and Minimization of Interference 33

2.5 Flexibility of Wind Tunnel 37

2.5.1 Acrylic Windows Versatility 37

2.5.2 Wind Tunnel Aperture for Different Boundary Conditions 39

3 Pressure Gradients **42**

3.1 Theoretical Estimates of The Pressure Gradient 42

3.2 Experimental Approach to Acquiring Pressure Gradients 45

3.3 Static Pressure Tap Geometry 47

3.4 Proposed Pressure Gradient Improvements 49

3.5 Boundary Layer Trip 50

4 Structural Integrity **52**

4.1 General Overview of Mass Properties 52

4.2 Beam Deflection and Buckling of Support Structures 55

4.3 Window, Roof, and Ceiling Vibration 59

5 Future Work and Recommendations 62
5.1 Refining Changes 62
5.2 Characterizing Experiments 62
5.3 Small on Large Scale Interaction 63

6 Conclusion 64

References 65

List of Figures

1 Da Vinci's Depiction of Turbulence [Da Vinci, 2012] . . . 1
2 Visual Representation of The Different Layers within a TBL . . . 5
3 Idealized Image of Hairpin Vortices and UMZs [Adrian et al., 2000] . . . 8
4 Hairpin Vortex Propagation [Zhou et al., 1999] . . . 9
5 0.381x0.381-meter (15x15-inch) Wind Tunnel Location at ARL [Jacobs, Jason, 2007] . . . 14
6 Normalized Velocity Profile for 3.65m Test Section . . . 16
7 Visual Representation of Turbulent Boundary Development as a Function of x . . . 16
8 Reynolds Shear Stress Number at x=2.39m . . . 17
9 Reynolds Momentum Number at x=2.39m . . . 18
10 Blasius Properties at Different Freestream Conditions . . . 19
11 Differing Classical Leading Edge Geometries [Davis, 1980] . . . 20
12 Overview of Parametric Optimization of Leading Edge Profile [Hanson et al., 2012] . . . 21
13 Leading Edge Profile for 3.65-meter Test Section . . . 22
14 Leading Edge CAD for 3.65-meter Test Section . . . 23
15 Trailing Edge CAD for 3.65-meter Test Section . . . 23
16 Entire Flat Plate CAD for 3.65-meter Test Section . . . 23
17 Trailing Edge Raiser with Protractor . . . 25
18 Component Joints on Flat Plate . . . 26
19 Sample of Joints Located on Flat Plate . . . 27
20 Generic Example of Laser Pulse vs Camera Aperture Pulse . . . 28
21 Incident Light vs Scattered Light Intensity [LaVision, 2020] . . . 29
22 Proposed Laser Beam Path to illuminate Flow . . . 30
23 Example of Interrogation Windows . . . 30
24 Potential Camera Placements for PIV . . . 31
25 Illustration Highlighting Fluid and Seeding Particle Discrepancy . . . 32
26 Seeding Particles and Agglomeration . . . 33
27 Isometric View of Compiled Wind Tunnel . . . 34
28 Aft Acrylic Windows in the Test Section . . . 35
29 Generic Example of Light Bending Through 2 Different Mediums . . . 36
30 Streamwise View of the Test Section for Optical Purpose . . . 37
31 Overhead View of the Test Section . . . 37
32 Streamwise Detailed View of The Hinges . . . 38
33 Cross Sectional View of The Hinges Profiles . . . 38
34 Latches and Hook with Opened Acrylic Windows . . . 39
35 Test Section Roof Option A . . . 40
36 Test Section Roof Option B [Parthasarathy, Aadhy, 2020] . . . 40
37 Additional Capabilities and Effects of Roof Option B [Parthasarathy, Aadhy, 2020] . . . 41
38 Pressure Tap Location on Current Test Section . . . 42
39 δ_{99}, δ^* at 4 Testing Conditions . . . 43
40 δ^* at 4 Freestream Conditions . . . 45
41 Model of Identical Wind Tunnel with Original Test Section [Jacobs, Jason, 2007] . . . 47
42 Classic Static Pressure Tap Design . . . 48

43 Pressure Tap Geometry Chosen for Current Test Section 48
44 Proposed Bleeding Options on Current Test Sections 50
45 Support Structures 52
46 Cross Sectional View of The Hinges With Labels on Supporting Beams 54
47 Main Support Components 55
48 Load Distribution on Main Support Structure 57
49 Deflection of Main Supporting Beams 58
50 Natural Frequency for Aluminum Floor/Ceiling 61
51 Natural Frequency for Acrylic Windows 61

List of Tables

1 Different Properties of Glass and Acrylic [Gere and Goodno, 2013] 35
2 Test Plan for Initial Pressure Gradient Characterization 46
3 Test Section Mass Properties 53
4 Material Properties for Wind Tunnel Support Systems [Gere and Goodno, 2013] 55
5 Loading of Main Support Legs 56
6 Deflection and MSE_b of Main Supporting Structures 59

Nomenclature

List of Abbreviations

$2D$	2-Dimensional
$3D$	3-Dimensional
APG	Adverse Pressure Gradient
ARL	Aerodynamics Research Laboratory
BL	Boundary Layer
CAD	Computer Aided Design
DNS	Direct Numerical Simulations
E	Modulus of Elasticity
FPG	Favorable Pressure Gradient
ft/s	Feet per Second
I	Moment of Inertia
In	Inches
K	Acceleration Parameter
Kg	Kilograms
LE	Leading Edge
LES	Large Eddy Simulation
m/s	Meters per Second
mm	Millimeter
Pa	Pascals
PIV	Particle Image Velocimetry
$RANS$	Reynolds Averaged Navier Stokes Equations
TBL	Turbulent Boundary Layer
TE	Trailing Edge
TSF	Theresa Saxton-Fox Research Group
$UIUC$	University of Illinois at Urbana-Champaign
WT	Wind Tunnel
ZPG	Zero Pressure Gradient

List of Symbols

Eu	Euler Number
Fr	Froude Number
Re	Reynolds Number
St	Strouhal Number
Stk	Stokes Number
U	Velocity-Streamwise Direction
V	Velocity-Wall Normal Direction
$<>$	Ensemble Average
β	Pressure Gradient Parameter
ΔP	Change in Static Pressure
δ	Boundary Layer Thickness
δ^*	Displacement Thickness, Turbulent
δ^*_{lam}	Displacement Thickness, Laminar
$\delta_{99,lam}$	Boundary Layer Thickness, Laminar
δ_{99}	Boundary Layer Thickness, Turbulent
ϵ_r	Energy Dissipation Rate
κ_v	Von Kármán Constant
μ	Dynamic Viscosity
ν	Kinematic Viscosity
ρ	Density
σ	Standard Deviation
τ_w	Wall Shear Stress
θ	Momentum Thickness
Re_τ	Reynolds Shear Stress
Re_θ	Reynolds Momentum Number
U_∞	Freestream Velocity
U_τ	Shear Stress Velocity
x	Streamwise Spatial Coordinate
y	Wall-Normal Spatial Coordinate
y^+	yU_τ/ν Inner Length Scale

1 Introduction

Fluid mechanics is part of every day life, from seeing the wind blowing alongside the trees outside your window, to the blood that flows through your veins. Wall bounded flow will transition from laminar to turbulent in many practical scenarios. From a qualitative viewpoint one of the first attempts to understand this behavior was done by Leonardo Da Vinci in 1508 [Lumley, 1992]. Da Vinci observed streamlines on a waterfall. Da Vinci illustrated the movement of the streamlines from the channel and their "impact" after reaching the seemingly stagnant body of water below. In Da Vinci's illustration he attempted to describe the aftermath of the impact by drawing out the vortices, figure 1.

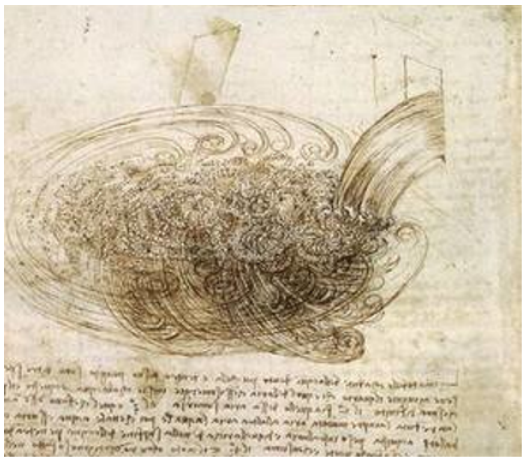

Figure 1: Da Vinci's Depiction of Turbulence [Da Vinci, 2012]

Da Vinci successfully identified turbulence, but he was centuries away from being able to quantify it, simply because he did not have the proper equipment that we have today. Transitioning to modern time, there has been a great amount of work conducted to quantify and predict turbulence, both experimentally and computationally.

Examples of turbulence include but are not limited to the following. The work conducted by [Azman et al., 2018] demonstrated how wind blows into urban areas. The skyscrapers act as roughness elements which lead to turbulence. Turbulence facilitates heat entrapment or a concept commonly known as the "urban heat island effect" [Azman et al., 2018]. A city is a hub for high energy usage and its main source of cooling are natural convection currents. Understanding how these roughness elements (skyscrapers) affect the diffusion of this heat is essential to lowering the temperature of these urban areas, especially in the hot summer months. Furthermore, the turbulent wind which stems from the atmosphere in both urban and rural areas, is responsible for the diffusion of pollutants. Turbulent flow can also be present on the surface of a pipe, car, airplane, rocket, ship through an automotive engine, etc. Furthermore, it is worth noting that for a commercial airliner, turbulent flow accounts for about 50% percent of the total drag, and for long pipe and channel flows it accounts for approximately 100% of the drag [Marusic et al., 2010]. Thus, in some situations it would be beneficial to mitigate the presence of turbulence but in others such as combustion, an increase in turbulence intensity favors the mixing of the reagents. Successfully understanding turbulence would enable scientists and engineers to take its behavior into account when developing new technologies.

1.1 Brief Development of the Boundary Layer Equations

The following sections will lightly cover the development of the classical equations that attempt to model flow, known as the Navier-Stokes equations. These sections will also discuss the Boundary Layer equations developed by Prandtl and his student Blasius, as a result of the discrepancies between the Navier-Stokes (N-S) equations and d'Alembert's Paradox. In the early 19th century Augustin-Louis Cauchy developed what is known as the Cauchy Stress Tensor. This is essentially a representation of the stresses on the different faces of an element in space. This idea was further coupled with the Navier-Stokes concept of the convective and diffusion characteristic of fluids. This can be seen below, relation 1.1, which is known as the Navier-Stokes equation. Index (i, j) is associated with U and x, they indicate the velocity and respective spatial coordinate. The straight forward addition of the *k* component could easily make these equations function in the 3-dimensional realm as well. Furthermore, ρ is the density, P is the pressure, ν is the kinematic viscosity of the fluid.

$$\frac{\partial U_i}{\partial t} + U_j \frac{\partial U_i}{\partial x_j} = -\frac{1}{\rho}\frac{\partial P}{\partial x_i} + \nu \frac{\partial^2 U_i}{\partial x_j^2} \tag{1.1}$$

The scope of this document will be limited to wall-bounded turbulence. This means that the flow travels over a surface and due to the 'no' slip boundary condition among other factors, a momentum and mass deficit begins to occur, which forms a shear layer forms above the wall known as a boundary layer. For many decades the concept of a boundary layer was not obvious to scientists. According to d'Alembert's derivation he found that a sphere in constant, incompressible flow had a net drag of zero, which did not agree with logic. The reason for this was because d'Alembert solved the incompressible flow equations in accordance to the inviscid flow theory which neglects the presence of a boundary layer, or a viscous region near the surface. This is known as d'Alembert's paradox, which was published in 1752. Furthermore, the presence of a shear layer or a boundary layer was not explicitly conceptualized until 1904 as a result of the studies conducted by Prandtl. More information on Prandtl's discovery will be provided later in this section. First, it is interesting to note that Osborne Reynolds popularized the concept of laminar and turbulence in pipe flow by conducting a series of experiments which noted the transition between uniform and consecutively seemingly chaotic flow in which he found the velocity to be non-uniform [Reynolds, 1883]. Information on this was published in 1883. Reynolds was known to be very meticulous and observant when he conducted his experiments. Reynolds denoted a non-dimensional variable known as Reynolds numbers which represents the ratio of inertial to viscous forces within a flow. Reynolds number is often denoted as ρ being the density of the fluid, μ being the dynamic viscosity of the fluid, L representing a characteristic length. The equation for the Reynolds number can be seen below 1.2.

$$Re_x = \frac{\rho U_\infty x}{\mu} \tag{1.2}$$

The characteristic length chosen depends on the scope of the experiment. Thus, this ratio can be used to represent a mirage of situations. For example, if one wanted to investigate ocean currents the characteristic length could be the depth of the ocean [Marusic et al., 2010]. Other situations can include using the chord of the wing of an aircraft or even the length of its fuselage as the characteristic length. For investigations on weather patterns the characteristic length can be the highest vertical length [Marusic et al., 2010]. The ratio from the Reynolds number represents different flow regimes, which allows for different experiments to be compared with each other by having this common variable. Furthermore, this iconic relation serves a benchmark to characterize the transition of flow. 500,000 is usually accepted as turbulent flow in the context of a pipe [Eckhardt et al., 2007]. The Reynolds number *Re* is just one example of

non-dimensionalization to parameterize the flow. In the later part of the 19th and 20th century there was an increase in these such as: Strouhal number *St* which is a ratio of denoting the unsteadiness of the flow, Euler number *Eu* which is a ratio of the pressure forces to the inertial forces, the Froude number *Fr* which is used to represent the ratio of the inertial forces to the weight of the fluid element.

In the early 20th century Prandtl was able to view and quantify the shear layer that was mentioned in the previous paragraph. This became known as the boundary layer theory (BLT) [Serrin, 1967]. Prandlt and his student Blasius found a method which enabled others to adopt non-dimensional variables to simplify the Navier-Stokes equations and develop similarity solutions. Blasius solutions assume: laminar, incompressible, a zero pressure gradient (ZPG) and steady flow over a flat plate. These similarity solutions can denoted by the following equations, 1.3 and 1.4. However, the leading 1/2 coefficient on the second unit of equation 1.3 is often changed. However, this would be offset by the representation of equation 1.4 [White and Corfield, 2006].

$$f(\eta)''' + \frac{1}{2} f(\eta) f(\eta)'' = 0 \tag{1.3}$$

$$\eta = y\sqrt{\frac{U}{\nu x}}, \tag{1.4}$$

y is the spatial coordinate of an arbitrary particle in the direction normal to the wall, and *x* is the position of the same particle in the direction streamwise to the mean flow, *U*. f' is the normalization of the local velocity (u/U) at the spatial coordinates (x, y). At the wall, where y=0, the f' value is also 0, but when η approaches infinity, then f' asymptotes to 1. The interested reader can refer to White for more information on Blasius' methodology [White and Corfield, 2006]. Shortly after Blasius, Von Kármán reasoned that the average velocity of a turbulent boundary layer was proportional to the logarithmic distance normal to the wall [Von Kármán, 1931]. This became known as the law of the wall, which then led to Kolmogorov's theory [Kolmogorov and Nikolaevich, 1962]. This will be explained further in the section 1.2. Factoring in the Reynolds number decomposition [Eckhardt et al., 2007], the following equation demonstrates the mean velocity followed by the perturbation or fluctuating velocity components.

$$U(x,y,z,t) = \overline{U}(x,y) + u'(x,y,z,t) \tag{1.5}$$

$$V(x,y,z,t) = \overline{V}(x,y) + v'(x,y,z,t) \tag{1.6}$$

$$W(x,y,z,t) = \overline{W}(x,y) + w'(x,y,z,t) \tag{1.7}$$

$$P(x,y,z,t) = \overline{P}(x,y) + p'(x,y,z,t) \tag{1.8}$$

Now, placing relations 1.5 to 1.8 back into 1.1 and assuming constant pressure and steady flow, these equations can be simplified into the following.

$$\overline{U}\frac{\partial \overline{U}}{\partial x} + \overline{V}\frac{\partial \overline{U}}{\partial y} = \frac{\partial}{\partial y}\left(-\overline{uv} + \nu\frac{\partial \overline{U}}{\partial y}\right) \tag{1.9}$$

In order to relate equations 1.1 to the similarity solutions represented by equations 1.3 and 1.4, the following boundary conditions must be applied to relation 1.9. Equation 1.10 is the continuity condition and the no-slip condition is shown by equation 1.11. The latter means that when the flow is in contact with the surface, it cannot slip, so there is no translation in the streamwise, spanwise or normal directions to the wall. In addition as the region of interest moves away from the wall or y goes to ∞ then the flow is undisturbed and it approaches the freestream velocity U_∞ or U, equation 1.12.

$$\frac{\partial \overline{U}}{\partial x} + \frac{\partial \overline{V}}{\partial y} = 0 \tag{1.10}$$

$$\overline{U}(x, y = 0) = \overline{V}(x, y = 0) = 0 \tag{1.11}$$

$$\overline{U}(x, y- > \infty) = U_\infty \tag{1.12}$$

1.2 Foundation of The Canonical View of Turbulence

The theory behind turbulence is still being debated. However, a generally widely accepted theory was pioneered by Lewis Richardson [Platzman, 1967]. Richardson was a mathematician and while attempting to numerically predict weather patterns he offered an interesting observation. Richardson hypothesized that the fluid elements over the boundary layer, contained longer whirls and that the fluid elements closer to the wall or the ground, had shorter whirls due to viscosity. In essence, he recommended the use of an energy cascade approach to understanding turbulence, which will be discussed later in this section. However, it is essential to mention pioneers of this field attempted to model turbulent flow the same way that Blasius modelled steady, incompressible flow. However, the diffusive terms of the Navier-Stokes equations, relation 1.1, are notoriously non-linear. When the perturbations of the flow that are shown by equations 1.5 to 1.8 are plugged into the N-S equations, they cause great difficulty in trying to solve the N-S equations. Modern computers are not able to fully solve these at practical Reynolds numbers.

The first part of this section will cover the concept of the inner, overlap or log region and the outer layer of the turbulent boundary layer (TBL), along with their respective equations. The second subsection will provide the canonical format of the energy power spectra for the TBL. The design of test section that this document describes strives for canonical turbulent flow, hence why this chapter provides the reader with some information on the concept.

1.2.1 Inner, Outer and Overlap Regions of The TBL

Figure 2 demonstrates the qualitative concept between the different layers. We will establish the logic of inner region. As mentioned in section 1.1, non-dimensional variables allow the parameterization of select flow structures. l=ν/u_τ is generally known as the inner length scale. We will say y^+= y/l to relate the spatial coordinate in the wall normal direction to the inner length scale. Generally the inner layer is said to be $0 \leq y^+ \leq 0.15Re_\tau$ [Marusic et al., 2010].

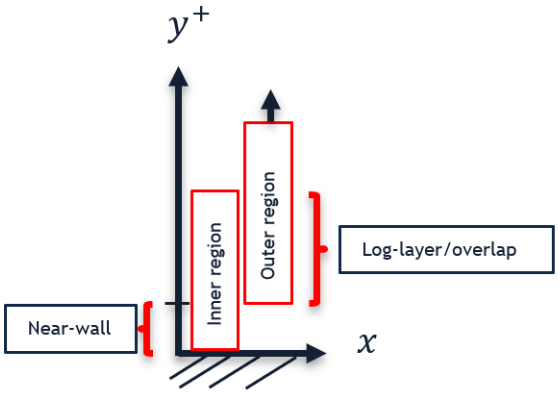

Figure 2: Visual Representation of The Different Layers within a TBL

Furthermore, the near-wall region is typically denoted as $0 \leq y^+ \leq 30$.

$$T_w = \mu \frac{\partial u}{\partial y}, y = 0 \tag{1.13}$$

$$U_\tau = \sqrt{\frac{\tau_w}{\rho}} \tag{1.14}$$

$$Re_\tau = \frac{\delta U_\tau}{\nu} \tag{1.15}$$

A great pioneer that set the tone for information of near-wall information within a TBL was Von Kármán. He established a theory which said that the velocity in this region is proportional to the logarithmic distance from the wall. Equations 1.16 and 1.17 coupled with the leading order of the boundary layer equation found in 1.1 produce equation 1.18.

$$\frac{\overline{U}}{U_\tau} = f(y^+) \tag{1.16}$$

$$\frac{-uv}{u_\tau^2} = g(y^+) \tag{1.17}$$

$$f^{''} + g^{'} = 0 \tag{1.18}$$

If relation 1.18 is integrated once, then one can arrive to:

$$f(y^+)^{'} = -g'(y^+) + f'(0) \tag{1.19}$$

Based on equation 1.16 then the right-most term of equation 1.19 is 1, since the local velocity when y^+ is zero is the velocity of U_τ. Now, for the outer layer the length scales are inherently different, so a new term for normalization must be established. We can start by naming a function similar to the η that was described earlier by Blasius. In fact η is often referred to as y/δ. This is done due to the fact that most of the characterization that Blasius conducted regarding

Boundary Layer Theory, was focused on the outer layer. The outer layer is classicaly defined as $30/Re_\tau < y/\delta < 0.15Re_\tau$ [Marusic et al., 2010]. The following relation 1.20 shows a function F which includes Re, and η. The σ_{n+1} are gauge functions as labeled by Hinch [Hinch, 1991].

$$\frac{U}{U_\infty} = F(\eta, Re)\ F_0(\eta) + \epsilon_1(Re)F_1(\eta) + \epsilon_2(Re)F_2(\eta) \tag{1.20}$$

Important assumptions that can be made about the additional perturbation terms or gauge functions is they disappear as Re approaches infinity. Similarly to formula 1.17, a new function for the outer layer is established in equation 1.21.

$$\frac{-uv}{u_\tau^2} = G(y^+) \tag{1.21}$$

Perhaps one of the most transcendental advances of the theory that was just mentioned is the reconciliation of these in the overlap or log-layer region of the TBL [Von Kármán, 1931], [Hinch, 1991]. One way of achieving this is by using the scaling terms of the inner layer on equation 1.20 through a normalized velocity gradient. Through this method, a high Re is also assumed, which means $l \leq y \leq \delta$. It is also essential to allow for the g and the G to be equal and constant within the overlap region. Equation 1.22 demonstrates with the velocity gradient in the far left. The κ_v is a constant that was used by Von Kármán to describe the equation for the log law which can be seen below, equation 1.23.

$$\frac{y}{U_\tau}\frac{\partial U}{\partial Y} = y^+ f'(y^+) = \frac{U_\infty}{U_\tau}\eta F_0'(\eta) + \epsilon_1 \frac{U_\infty}{U_\tau}\eta F_1(\eta) = \frac{1}{\kappa_v} \tag{1.22}$$

$$f = \frac{1}{\kappa_v} ln(y^+) + B \tag{1.23}$$

Relation 1.23, can further be manipulated and with the proper constants can be placed into the traditional equation [Von Kármán, 1931].

$$u = \frac{u_\tau}{\kappa} ln(y^+) \tag{1.24}$$

1.2.2 Energy Models of The TBL

Stemming from Richardson's hypothesis on the energy cascade model, Kolmogorov proposed a theory in 1941, which he later revised in 1962 [Kolmogorov and Nikolaevich, 1962]. This depended on the assumption that the flow-field was incompressible, and at moderately high Reynolds numbers, it described the local structure of turbulence mostly within the overlap region. The 1962 paper was a refined version of the 1941 paper by Kolmogorov, this was a result of Landau realizing an irregularity with regards to the original energy dissipation relation, ϵ.

$$\epsilon = \frac{1}{2}\nu \sum_{\alpha} \sum_{\beta} \left(\frac{\partial u_\alpha}{\partial x_\beta} + \frac{\partial u_\beta}{\partial x_\alpha} \right)^2 \tag{1.25}$$

ν is the kinematic viscosity of the fluid, u, x are analogous to the same terms found in the N-S. α, β are the same to i and j in the N-S, equation 1.1. The former two variables are shown here to parallel the iconic paper by Kolmogorov [Kolmogorov and Nikolaevich, 1962], and avoid confusion with this thesis. Furthermore, Landau noted a problem with equation 1.25. Under certain circumstances the large scale structures L and the internal scale structures l had a ratio of $\frac{L}{l} >> 1$. This meant the previous mentioned representation of ϵ would not suffice. As a result, Kolmogorov refined the original expression and devised an alternate relation that would allow the energy dissipation rate to exhibit an asymptotic behavior, and thus address Landau's concern. This can be seen below, equation 1.26, ϵ_r.

$$\epsilon_r(x,t) = \frac{3}{4r^3\pi} \int \epsilon(x+h,t)dh \tag{1.26}$$

This is under the assumption that the height h at which this relation is taken, normal to the wall is $h << r$ with r being the approximate radius of the eddy. This means that instead of assuming self-similarity of the statistical distributions through all of the inertial scales, there was in fact self-similarity at each cascade step [Kraichnan, 1976] and this was due to the spatial intermittency of the velocity differences. An alternate representation of the Kolmogorov scales can be defined by the following, equation 1.27.

$$E(\kappa) = C\epsilon^{2/3}\kappa^{-5/3}(\kappa * L)^{-\mu} \tag{1.27}$$

E represents the wave-number spectrum of kinetic energy, C is a non-dimensional value that depends on the Reynolds number, L is a length scale that essentially represents the macroscale or where the bulk of the kinetic gets injected into the turbulent boundary, which then proceeds to trickle down to the dissipative viscous length scales. κ represents a unit between the inertial range of the wave numbers with $L^{-1} << \kappa << \kappa_d$ with κ_d being the smallest length scales, or where the dissipative length scales are the strongest. Through Kolmogorov's discovery his main hypothesis argued that at sufficiently high Reynolds numbers, the mean statistics of turbulence do not vary and are dominated by ν and ϵ. In Kolmogorov's derivation he used the variables $\eta = (\frac{\nu^3}{\epsilon})^{1/4}$, he also introduced ϵ approximately equal to $\frac{(U_\eta)^3}{\eta}$, which was used to normalize $E(\kappa)$. The former representation of η is known as Kolmogorov's scale [Kolmogorov and Nikolaevich, 1962]. Normalizing $\frac{E(\kappa)}{\eta(U_\eta)^2}$ and plotting this against $log(\kappa)$ Kolmogorov was able to discover the presence of three regions within the turbulent boundary layer: outer region, inertial subrange (logarithmic) and the inner region (dissipative region) [Marusic et al., 2010]. This information was recovered by observing the inflection points of the plots, the inertial subrange is recognized as following the $(-\frac{5}{3})$ rule because of the slope usually observed.

1.3 Modern Visions of Scale Interaction

Section 1.2 discussed the classical view of TBL structures. Section 1.3 will explain some of the modern views on turbulence that have been made possible due to new advances in technology.

1.3.1 Hairpin Vortices

In 2000, Adrian et al, was able to demonstrate something Townsend had described as inactive pockets of turbulent flow [Townsend, 1980], [Adrian et al., 2000]. They conducted three experiments at distinct momentum Reynolds numbers $930 < Re_\theta < 6845$. Adrian et al, cited different pockets of flow as exhibiting a hairpin or horsehoe-like appearance [Adrian et al., 2000]. Figure 3 shows an idealized image of this concept, flow goes from left to right. The lower part of the image, whose color is blue, is meant to represent the wall. The brown, tan and white sections labeled I, II, and III, respectively are the uniform momentum zones (UMZ). The yellow objects, with are relatively thinner and smaller represent the individual hairpins, these are closest to the wall. Notice how as they propagate in the streamwise direction, they become larger, and for ease of visualization purposes they tend to change colors, and become more cream-colored. The cream-colored structures, or packets are made up of individual hairpins and eddies.

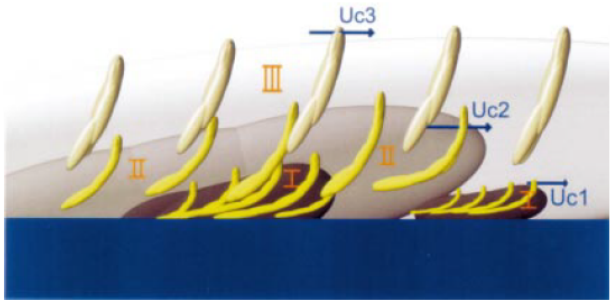

Figure 3: Idealized Image of Hairpin Vortices and UMZs [Adrian et al., 2000]

In addition, the different packets have a blue arrow and are labeled Uc1, Uc2, and Uc3 which symbolize the convective velocity experienced. The magnitude or order of the speed is the following Uc1<Uc2<Uc3. The smaller and slower moving hairpins are often overrun by the larger, faster compiled structures, also known as UMZs. On figure 3 just above the wall, the angle of inclination, relative to the head or the highest point of the hairpin, varies. These close to the wall hairpins contain a small angle then as they propagate streamwise, the angle of inclination rises to 45-90 degrees. Packets on the other hand, have a mean angle of inclination of 12 degrees. The UMZs are composed of hairpins. Figure 3 is an idealized representation of the hairpin vortices, meaning that they are simple ramp structures, in actuality they do not always look this way and may show negative ramp correlations particularly those UMZs near to the wall [Adrian et al., 2000], [Zhou et al., 1999].

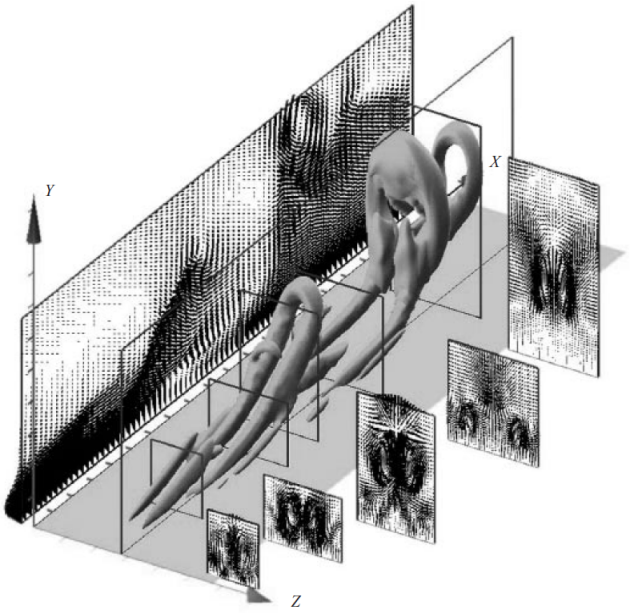

Figure 4: Hairpin Vortex Propagation [Zhou et al., 1999]

Figure 4 shows the development of a hairpin vortex in the streamwise direction. It is important to note that it is not symmetric. Under homogeneous shear flow it is possible to obtain symmetric hairpins [Theodorsen, 1955]. The reason for the shape of the vortex is a result of the counter rotating vortices that are a result of the momentum zones that surround the legs of the hairpin vortices [Marusic et al., 2010]. Typically, the center core of the hairpin moves in the streamwise direction while the outside is generally characterized by retarding flow. Some of the limitations regarding the development of this discipline is to be able to discern the differing length scales in the logarithmic region, but even more so in the outer layer. The theories that have been mentioned in this section are based on the classical theory regarding near-wall physics, y^+= 50-60. The near-wall convection velocities contain low reynolds numbers by nature, which makes DNS appropriate [Adrian et al., 2000]. Nonetheless despite the limitations, the findings by Adrian et al, have been instrumental in motivating a physical representation of the structures within the TBL and have allowed investigators to formulate different methods and mathematical procedures to keep exploring scale interaction within the TBL [Townsend, 1980], [Adrian et al., 2000]. It has ushered a period in which older theories have been confirmed with higher computational power, and improvements in experimental equipment such as PIV, have corrected some of these theories too [Zhou et al., 1999].

1.3.2 Amplitude Modulation

The previous subsection mentioned that a limitation of studying wall-bounded turbulence is the difficulty of discerning the diverse length scales. This subsection will discuss the approach by Mathis et al, known as amplitude modulation, in which the effect of the large scales on the smaller scales was investigated [Mathis et al., 2009]. This study was conducted via an experimental setup that included hot wires at an Re_τ of 7300. Mathis et al, found that the large scale structures within the log layer of the TBL seemed to affect the smaller scales in the form of amplitude modulation [Mathis et al., 2009]. They also discovered that as the Reynolds number increased, the effect by the amplitude modulation was more apparent. They looked at a spectogram that included the pre-multiplied spectra

$k_{xx}\phi_{uu}/U_\tau^2$, the data for this consisted of streamwise fluctuating velocity values. Two distinct regions were looked at, y^+=15, and y/δ=.06. The former region is associated with the viscous scaled energy structures near the wall, the latter region is assumed to be the result of superstructures, in the outer scale [Hutchins and Marusic, 2007]. The wavelength was defined as λ_x, with λ_x=$2\pi/k_x$. In order to begin the scale decomposition of the velocity signal they imposed the following conditions to a spatial filter that was imposed on the velocity data, equations 1.28 and 1.29. This was done to differentiate between the long and short wavelengths in the signal.

$$L : \lambda_x/\delta > 1 \tag{1.28}$$

$$S : \lambda_x/\delta < 1 \tag{1.29}$$

In order to analyze the difference between the modulating signal and the modulated signal they used the Hilbert transform which is seen in relation 1.30.

$$H(t) = H(\chi(t)) = \frac{1}{\pi} P \int_{-\infty}^{+\infty} \frac{\chi(\tau)}{t-\tau} d\tau \tag{1.30}$$

$H(t)$ is a convolution integral, P is the cauchy principal of the integral, and τ is the time shift. Furthermore, the decoupling of the raw velocity signal includes creating an envelope $E(U_s^+)$, for the modulated signal. While the U_L^+ is assumed to be the modulating signal, the fluctuating signal that is inherent of U_S^+ may also contain a wide range of amplitudes that could be inputted as a modulating signal. Thus this envelope can indicate all of the modulating effects. It is not only limited to the modulating signal that stems from the log region or where the outer peak was y/δ=.06, which is what they are primarily interested. In order to filter this out it was necessary to invoke the long wavelength spatial filter denoted by relation 1.28 [Mathis et al., 2009]. This then characterizes the modulating signal of the small-scales $E_L(U_s^+)$. ***R*** in equation 1.31 below is a way to express the degree of amplitude modulation, or the effect the superstructures have on the near-wall [Mathis et al., 2009].

$$R = \frac{\overline{U_L^+ E_L(U_s^+)}}{\sqrt{\overline{U_L^{+2}}}\sqrt{\overline{E_L(u_s^+)^2}}} \tag{1.31}$$

An interesting finding of this study was showing that the preconceived notion regarding near-wall processes to be autonomous can be challenged. They essentially decomposed the velocity signal of the log-region, and the near wall and showed a possible non-linear relationship between the two in the form of amplitude modulation. A unique connection between this section and the previous was regarding the superstructure attribute that was given to the outer peak. These are also regarded as VLSM or "very large scale motions" which are related to the idea of hairpins and packets that was demonstrated in the previous section [Hutchins and Marusic, 2007]. Thus both studies agree to some degree that near-wall structures, or hairpins are subject to the modulating effect of the superstructures in the log-region, [Mathis et al., 2009], [Adrian et al., 2000].

1.3.3 Conditional Averaging

The previous section explained the use of amplitude modulation in the context of data acquired from an experimental approach. The Hilbert transform was used after applying a spatial filter. This section will focus on a different study that used a method known as a sliding-window top-hat time average to differentiate between the large and small-scale fluctuations [Chung and McKeon, 2010]. Instead of using the Hilbert transform, conditional averaging was used [Chung and McKeon, 2010]. Furthermore, they did not use an experimental approach but rather a simulation. They employed the use of Large Eddy Simulations (LES), which will be discussed in section 1.4. The LES-predicted statistics were related to Re_τ of 2000 and 200,000.

The first step was to obtain the fluctuating velocity portion of the data. Equation 1.32 contains $U(t)$ which is the raw velocity signal. $\overline{U}(t)$ is the mean velocity, which leaves the fluctuating velocity component $u'(t)$.

$$u'(t) = U(t) - \overline{U}(t) \tag{1.32}$$

The fluctuating velocity component can be further decomposed conceptually into its small and large-scale parts, u_S ans u_L, respectively.

$$u'(t) = u_S(t) + u_L(t) \tag{1.33}$$

The sliding-window top-hat time averages are shown in the following relations.

$$u_L(x) = \frac{1}{\rho_c}\int_{x-\rho_c/2}^{x+\rho_c/2} u(x')dx' \tag{1.34}$$

$$\tilde{u_S}(x) = \frac{1}{\rho_c}\int_{x-\rho_c/2}^{x+\rho_c/2} u_s^2(x')dx' \tag{1.35}$$

ρ_c serves at the width of the sliding window [Chung and McKeon, 2010]. A low pass filter was invoked which dampened the frequencies higher than the inverse of ρ_c. Analogous to equation 1.31 the following formula was the effort to obtain a phase relation between the large-scale and small-scale fluctuations of the velocity signal.

$$R_\rho(y) = \frac{< (u_L - U)(\tilde{u}_s - < \tilde{u}_s >) >}{< (u_L - U)^2 >^{1/2} < (\tilde{u}_s - < \tilde{u}_s >)^2 > 1/2} \tag{1.36}$$

Now, to obtain information on the large-scale coherent regions, with regards to the cyclical or phase relationship between the large and small scales. Chung and McKeon used conditional averaging. The idea behind this is similar to that of UMZs with positive and negative fluctuating regions surrounding the hairpins [Marusic et al., 2010], [Adrian et al., 2000]. Equations 1.37 and 1.38 summarize the process.

$$< u_L | A_1 > (\Delta x), A_1 = u_L(x) - U < 0 \tag{1.37}$$

$$< \overline{u}_s | A_1 > (\Delta x) \tag{1.38}$$

Theoretically, event A_1 will occur nominally 50 % of the time, as a result of the circulating vortices or eddies that occur within the flow [Marusic et al., 2010]. But even more so, the largest takeaways from this study is that the small-scales near the wall are in sync with the larger scales, this was seen by information from equation 1.36 and conditional averaging. Taylors frozen turbulence hypothesis states that eddies at the same wall-normal location have the same convective velocity [Chung and McKeon, 2010]. However, this study showed that this was not the case for structures near the wall at $y/\delta < 0.08$, and for larger scales far away from the wall $y > 6/\delta$ [Chung and McKeon, 2010]. In fact, the latter saw that these UMZs exhibited a speed significantly lower to that of the mean. There was also evidence regarding locus of coherent regions of flow exhibiting an angle of inclination ranging 10-20 degrees, it was said this could be the main body of the hairpin vortex that was described in section 1.3.1.

1.4 Computational Approaches to Turbulence

Section 1.2 expressed an attempt to show the mathematical nature of the Navier-Stokes equations for incompressible flow, assuming zero pressure gradient flow over a flat plate. Applying order of magnitude analysis, naturally leads to attempting to understand the N-S equations asymptotically. These attempts can be refered to as analytical solutions. In present time there has been great advances in computational capacity which has allowed investigators to attempt to understand the behavior of fluids. This section will explore these avenues in the context of flow over a flat plate. The reason for this is because the subject of this document includes highlighting the design of a test section with a flat plate suited for studying fully developed TBLs.

In the late 1960s researchers were already trying to use computers to directly solve the Navier-Stokes equations. This approach was referred to as the Direct interaction equations or Direct Numerical Simulations (DNS) as we know them today [Orszag, 1969]. This method essentially composes a grid in which it takes into account the Kolmogorov dissipation scales and wave-numbers. The mesh size N must be able to account for the smallest scales of the Kolmogorov scale, which can be denoted as $N \geq (k_d * l)$. k_d represents the same quantity mentioned earlier in section 1.2.2. According to Orszag, using the IBM Model 360-91 which albeit is from the 1960s he estimated a fully resolved calculation of the Navier-Stokes with homogeneous turbulence would take around 3.2 million years. In 2018, it was estimated that if one wanted to fully solve a similar situation, it would take approximately 20 months [Rae et al., 1999], [Zhou, 2018].

Evolving from DNS, another popular computational technique known as Large Eddy Simulation (LES) was developed. The most computationally expensive portion of DNS are the smaller, dissipative scales. LES thus uses low-pass filtering through the use of subgrid-scale models to effectively filter out smaller scales and perform computations at higher Reynolds numbers [Geurts et al., 1994]. Geurts exemplifies various examples in which a filter can be applied to a DNS approach to conceive an LES model. Looking at the standard conservation of mass, momentum and energy equations. One can apply the following transformation on equation 1.18, to extract the desired large scale from the original DNS relation [Geurts et al., 1994].

$$\overline{f} = \int_{\Omega} G_{\Delta}(x, \zeta) f(\zeta) d\zeta \tag{1.39}$$

Ω represents the original domain, G the original kernel, Δ is the width of the kernel or the discretization of G. There are other models, such as Smagorinsky that have been widely used which expedite the computational speed of several models. However, these can contain deviant behavior with regards to the physics near a solid-

wall or within transitional flows [Rieth et al., 2014]. Reynolds-averaged Navier-Stokes (RANS) solvers employ time-averaged equations of motion. These use prescribed boundary conditions on the different flow problems. This method essentially represents the mean and fluctuating or turbulent flow as two separate equations, a sample of this can be seen as $U(x,t) = \overline{U}(\overrightarrow{x}) + U'(\overrightarrow{x},t)$ with $\overrightarrow{x}$ representing a vector of the fluid elements in the (x,y,z) directions. Separating these variables is known as Reynolds decomposition, which was exhibited in section 1.1. The accuracy of RANS is still a subject of debate. RANS needs prescribed boundary conditions near the wall, which can sometimes be trivial, it also is not always clear how much discretization is needed to effectively ease computational speed yet still capture the dissipative scales of the smallest eddies.

2 Tunnel Design

Now that a foundation regarding turbulence has been established we will move on to a new chapter. This chapter in part will discuss the basic technical specifications of the wind tunnel (WT) which was inherited to Theresa Saxton-Fox's (TSF) research group in 2018. The interested reader can refer to Jason Jacobs' PhD thesis for more information regarding the original facility [Jacobs, Jason, 2007]. More importantly, this chapter will justify the need for a new test section (TS), and the methodology behind the design. The purpose of this TS is to study fully developed TBLs, mainly through the use of PIV. This WT and the respective TS are located in the Aerodynamics Research Lab (ARL) at the University of Illinois at Urbana-Champaign (UIUC).

2.1 Background on Inherited 0.381x0.381-Meter Wind Tunnel

The inherited wind tunnel was originally put together through the help of different departments within UIUC. The inlet and test section stand were acquired from the permanent storage of the UIUC Mechanical Engineering Department. The cross section of the TS is 0.381x0.381-meter (15x15-inch), hence the title of this section. Furthermore, the exhaust fan was manufactured by Joy Manufacturing Company. This fan is a 1.21-meter (4-foot) diameter, 16-bladed, single stage. This fan is powered by a 120-Hp General Electric AX motor and controlled by an Eaton AF5000+ Dyanamatic variable frequency drive (VFD). A 2-piece diffuser is found downstream of the TS, and immediately upstream of the previously discussed fan. Furthermore, two 1.52x1.52-meter (5x5-foot) tunnel sections from an older wind tunnel that was previously found in the former Subsonic Aerodynamics Research Laboratory at the University of Illinois, were used in conjunction with a third diffuser to exhaust the flow outside into the atmosphere. The top portion of figure 5 depicts the WT used by TSF's group, but with the old TS.

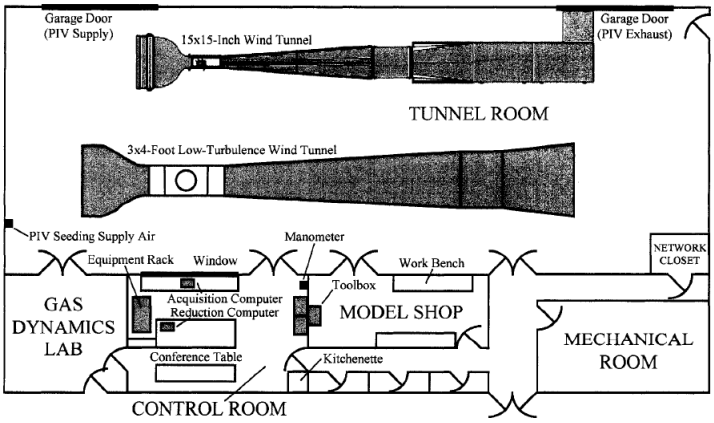

Figure 5: 0.381x0.381-meter (15x15-inch) Wind Tunnel Location at ARL [Jacobs, Jason, 2007]

The inlet is a 503 cm^2 (78 in^2), it is 10-cm (4-in) thick and includes several features that help diminish turbulent flow and allow for air to flow through the cross section in an evenly distributed manner. These features include: a honeycomb flow straightener, four 24-mesh stainless steel, turbulence-reducing screens. As a disclaimer, the tunnel pictured in Jacobs' thesis allegedly contains less flow straighteners than the one used in the TSF group. As a result the maximum WT speed has been significantly reduced from the time the WT was built to present day. Figure 5 depicts the proximity between upper wall and the original WT. The inlet also sits relatively close to the ground (not obvious on figure 5). When the tunnel was designed it was noted how these two features could contaminate the flow. This led to the execution of different experiments at varying air flow speeds that focused on the velocity and dynamic pressure

distributions of the cross section at various streamwise positions. According to Jacobs [Jacobs, Jason, 2007] across the cross section of the 1.21-meter (48-inch) long original test section the dynamic pressure had a $\pm$ 0.50% deviation from the calibrated mean pressure, and $\pm$ 0.25% variation in freestream velocity from the calculated mean. This is proven to be acceptable by Rae and Pope [Rae et al., 1999]. Furthermore, the aforementioned flow straighteners and screens created a streamwise turbulence intensity of approximately 0.16% in a freestream of about 73 m/s (240 ft/s).

2.2 Efforts to Create a Canonical Turbulent Boundary Layer

Section 2.2 will first justify the extension of the wind tunnel from 1.21-meters to 3.65-meters. Furthermore, this section will explain the design of the flat plate, and how it was made to emulate Blasius' semi-infinite flat plate theory. As a reminder, this theory assumed incompressible, steady flow over a flat plate, with a zero pressure gradient. Overall, the main goal was to design a flat plate that would allow for the development of a canonical TBL. For reference on Blasius and canonical views of turbulence please refer to sections 1.1 through 1.2.2.

2.2.1 Length Extension of Inherited Wind Tunnel

The previously mentioned 0.381x0.381-meter (15x15-inch) test section had a length of approximately 1.21-meters. Furthermore the equation for a fully developed turbulent boundary layer is commonly denoted as:

$$\delta_{99} = \frac{.37x}{Re_x^{1/5}} \tag{2.1}$$

Thus, the boundary layer thickness is directly proportional to the streamwise distance x (assuming the flow starts from x=0 and moves in the positive direction). Extending the tunnel would thus be beneficial for PIV. For reference Re_x is equation 1.2. The 2.1 relation can be derived from the Blasius similarity solutions in conjunction with the momentum integral energy equations assuming a constant freestream velocity [Guneshasa, Hasan, 2009]. Figure 5 has the old version of the tunnel, which on the image is labeled "15x15-Inch Wind Tunnel". Taking the constraints of where it sits and location of the walls. Other issues included: an angled column which supports the ARL's roof, the location of the garage door. Taking all of these into consideration it was decided by TSF's group to strive for a 3.65-meters long TS, at the very least. Knowing that the wind tunnel was going to be at least 3.65-meters in length, a MATLAB script was written to conduct preliminary analysis using the Blasius similarity solutions at around 30 m/s and with a length of 3.65-meters. It is true that the end goal of this facility was to be apt for experiments regarding turbulence. However it was best to first achieve the more simple Blasius-based flow, especially to insure a zero pressure gradient. After this was ensured, then the group could extrapolate from there to make more complex experiments. Figure 6 shows the preliminary results for the Blasius velocity profiles within the boundary layer through the length of the flat plate within the TS. After design and construction, it was planned that PIV data could be used in conjunction with the Blasius code. This could serve as a standard to compare the flow speed between the experimental and theoretical data, particularly at the LE, before the transition to turbulence occured [Reynolds, 1883]. The colorbar on the right side of figure 6 demonstrates the normalized velocity or u/U_∞. This plot has a freestream velocity of 30 m/s.

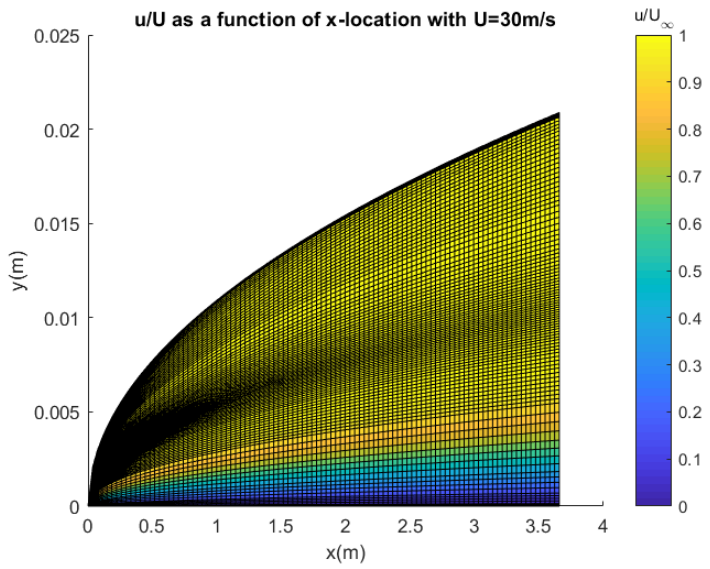

Figure 6: Normalized Velocity Profile for 3.65m Test Section

Figure 7 demonstrates the benefit of having a longer test section when the flow is turbulent. This plot was created using equation 2.1, thus figure 7 assumes the flow to be fully turbulent from the LE. Nonetheless, a flat plate without an initial fully turbulent LE would eventually cause the flow to become turbulent.

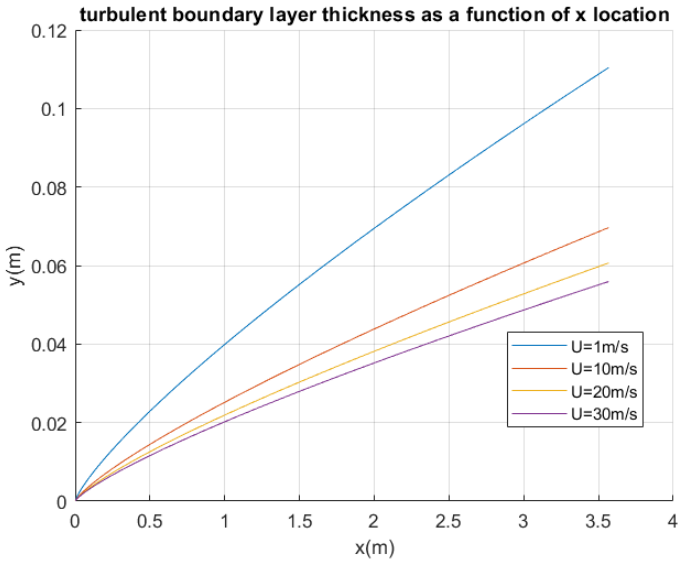

Figure 7: Visual Representation of Turbulent Boundary Development as a Function of x

It is popular to use trips to increase the transition rate towards turbulence, common objects are sand paper, square rods, circular rods or ziz-zag strips [Rengasamy and Mandal, 2017]. Interestingly, studies have demonstrated that turbulent flow have what is referred to as ”upstream memory” of what initially tripped the flow towards the turbulent regime [Schlatter and Örlü, 2012]. The skin friction coefficient, shape factor, and even the mean and fluctuating profiles seemed to contain significant differences based on what was used to trip the flow. Furthermore, Schlatter compared a set of experimental results with DNS simulations, and found differences. Going back Schlatter varied

different inflow conditions and this seemed to have been the reason for the discrepancies they saw in their test runs. In retrospect, it was found that having a $Re_\theta > 2000$ and placing the trip within the boundary layer eliminated the differing conditions when the fully turbulent developed boundary layer was observed. The proposed ideas for tripping the flow in the TSF facility will be discussed later.

Furthermore, the following relations describe how Re_θ, equation 2.3, is obtained. In a viscous flowfield where solid-fluid interaction occurs, θ is often regarded as momentum thickness [White and Corfield, 2006], equation 2.2. It is defined as perpendicular distance to the flow a stationary wall would have to be moved to provide the same momentum between the original location of the wall and a reference plane (reference-inviscid situation). This is related to momentum deficit, which was covered in section 1.1. The operating conditions of the wind tunnel were designed to be between 1 and 30 m/s, hence the bounds on figures 8 and 9. A general description of the flat plate, is that it was to be 3.65-meters in length, it contained 5 major pieces, all aluminum except for one which is all acrylic. This is the region where it was perceived to be the most important since it is where the canonical flow would be established, more of this will be described in subsequent chapters. The x-location for figures 8 and 9 was kept constant at 2.39-meters aft relative to the LE. This x-location is the midway point of the acrylic portion of the flat plate.

$$\theta = \frac{0.037x}{Re_\tau^{1/5}} \tag{2.2}$$

$$Re_\theta = \frac{\rho U \theta}{\mu} \tag{2.3}$$

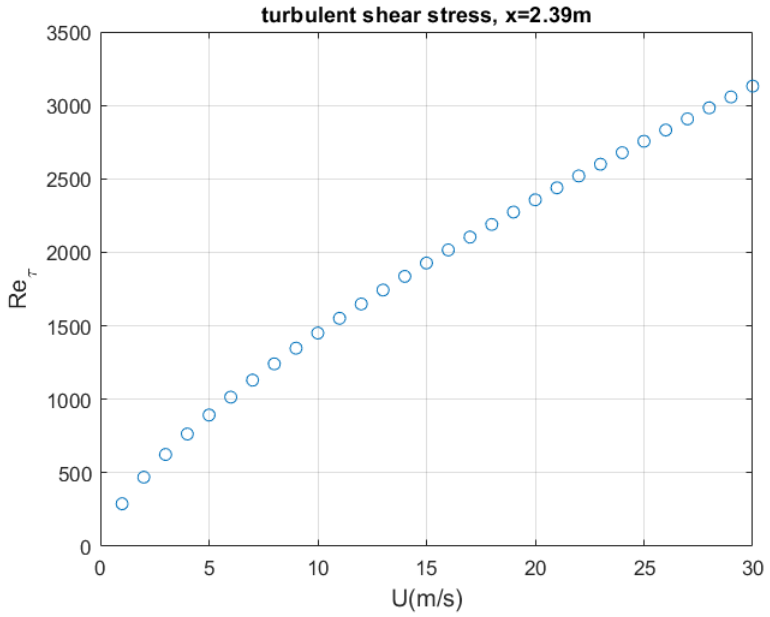

Figure 8: Reynolds Shear Stress Number at x=2.39m

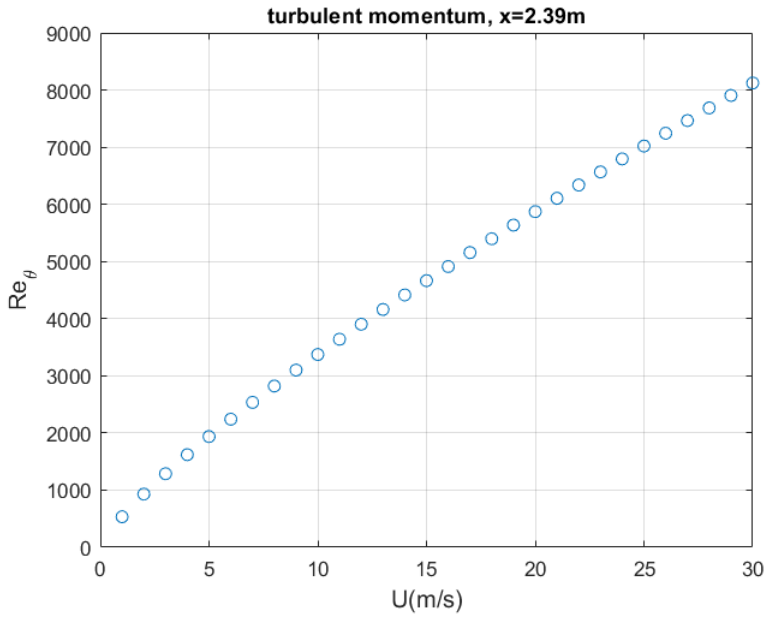

Figure 9: Reynolds Momentum Number at x=2.39m

Furthermore, displacement thickness δ^* is a quantity in which it is a hypothetical distance the wall would have to move in the normal direction to the wall to allow the same flow rate to occur if the conditions of the flowfield were inviscid, equation 2.4. This quantity is for a fully developed turbulent boundary layer.

$$\delta^* = \frac{0.048x}{Re_\tau^{1/5}} \tag{2.4}$$

The following plots on figure 10 show δ_{99}, δ^*, and θ at different speeds that are within range for TSF's WT. These plots are also representative of the WT's length. Once again it is fairly obvious that as the length of the flat plate grows, the boundary layer thickness also grows.

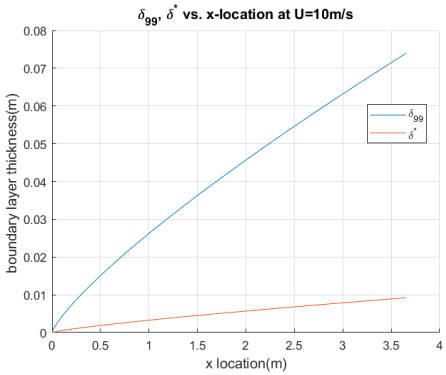

(a) Blasius Properties at U=10m/s

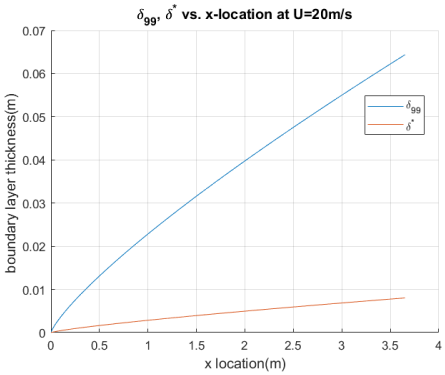

(b) Blasius Properties at U=20m/s

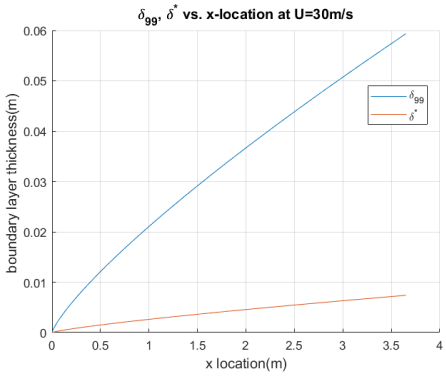

(c) Blasius Properties at U=30m/s

Figure 10: Blasius Properties at Different Freestream Conditions

2.2.2 Importance of Maintaining a Zero Pressure Gradient in The Test Section

Expanding on section 1.2 which provided an overview on the canonical view on turbulence. Some of the important realizations included: the shear stress varies with the normal distance away from the wall [Townsend, 1961], the production of turbulence that occurs in the log-layer, which is approximately equal to the dissipation rate of turbulent energy, which is generally denoted as ϵ [Kolmogorov and Nikolaevich, 1962]. Furthermore, β can sometimes represent the pressure gradient parameter [Monty et al., 2011].

$$\beta = \frac{\delta^*}{\tau_w}\frac{dP}{dx} \tag{2.5}$$

The δ^* is the non-dimensional displacement thickness, dP is the differential static pressure, and the dx is the displacement in the streamwise direction. Disseminating $\beta * dP/dx$ as a ratio relative to τ_w one can translate this into the pressure gradient force versus the wall shear stress [Clauser, 1954]. Assuming a constant β is often used to characterize "equilibrium boundary layers" [Clauser, 1954], [Monty et al., 2011], [Hinze, 1972], [Bradshaw et al., 1967]. When conducting experiments you have controlled variables, this allows for the introduction of classical theory to serve as a stepping stone for more complex phenomena, inadvertently adding a non-zero pressure gradient can potentially induce unexpected events in your flow. For example, the presence of a favorable pressure gradient would increase the acceleration of the fluid, and thus a different rate of the shear stress away from the wall would ensue relative to that of the zero pressure gradient (ZPG) [Finnicum and Hanratty, 1988]. Thus, as a form to cross-check or to compare

results one must keep similar controlled values with respect to contemporary and past investigations. A ZPG boundary layer tends to increase the turbulence intensity along with an increasing Reynolds number [Mathis et al., 2009], an adverse pressure gradient does the same, thus it is important to alienate these two things if one wants to independently analyze the effects of each on the boundary layer. Furthermore, from observing the Navier-Stokes equations it is straightforward to observe how the shear stress would vary if there was a pressure gradient. .

2.2.3 Effects of Leading Edge Geometry on ZPG and Flow Quality

As it was noted previously in section 2.2.2 it is important to establish a ZPG, before moving to more complex questions. In the context of a wing, the profile of the airfoil mandates the pressure above it and below. When the flow first sees the obstacle, it arrives at the stagnation point, which as it moves in the streamwise direction, a boundary layer forms. Thus, the stagnation point in conjunction to the profile is important in determining the pressure gradient over the surface of the wing. The stagnation point, and thus the coefficient of lift can be manipulated by the geometry and position of the TE, or the flap angle. Analogously a flat plate in a wind tunnel, works very similarly. This section will focus on the design of the flat plate, primarily led by the LE profile.

Thus, the challenge was to create a flat plate that would emulate Blasius, and contain a sharp LE that would allow for a ZPG. There is a vast amount of studies quantifying the effects of the LE on the quality of the flow downstream of the flat plate. The LE determines the pressure coefficient of the upper and lower surfaces of the flat plate [Davis, 1980]. A relatively thick leading edge would raise the possibility of flow separation. This event would lead to figuring out how to reattach the flow prior to commencing the development of the turbulent boundary layer, given that the length of the flat plate is finite, this would reduce the quality of the experiment as a whole, since the turbulent boundary layer thickness is a function of the x-location, as seen in equation 2.1. Very sharp leading edges have a tendency of succumbing to non-uniform flow and/or disturbances in the flow [Goldstein, 1985], [Goldstein and Hultgren, 1987]. Furthermore, Morkovin [Morkovin, 1969] found that instability at the LE can negatively effect the transition of the flow between the laminar and the turbulent phases. Granted, being that turbulence is being studied and a fully developed boundary layer is wanted, the issue with transition is not of primary concern. However, it is still good practice to mitigate instability, if possible. Thus, the task in finding an appropriate leading edge was important. Research has taken different approaches, earlier studies relied on using classical geometric shapes and modifying their respective dimensions [Davis, 1980]. They used elliptical nose and double arc profiles. In the late 1990s the onset of the increase of computational capacity led to the use of numerical solutions to explore more complicated techniques such as parabolas and super ellipses [Haddad and Corke, 1998]. Conventional leading edge geometries can be seen on figure 11. The featured leading edge geometries include, elliptical nose (leftmost) and double arc nose profiles (other two contours).

Figure 11: Differing Classical Leading Edge Geometries [Davis, 1980]

These three contours have two similar features. There is an apparent discontinuity at the front tip of the each design.

Thinking of the leading edge of a flat plate as a component that would span the test section, it could arguably be represented as flow over a cylinder that experiences a positive/negative coefficient of pressure, which can lead to flow separation. Translating that logic to the aforementioned discontinuity, could not only cause flow separation but also disturbances which could potentially be propagated aft of the LE location [Goldstein, 1985],[Goldstein and Hultgren, 1987]. The additional common feature is the discontinuity at the juncture between the leading edge profile and the 'constant thickness' portion of the flat plate, which is not terribly obvious on figure 11, but the reader can infer that this location is reached immediately to the right of each LE profile, assuming flow is going from left to right. The "constant thickness" feature can be denoted as the "flat plate" on figure 12.

The design of the leading edge of the flat plate for the TSF facility was motivated by a technique that was demonstrated by Hanson [Hanson et al., 2012]. Computational work was done to parametrically optimize the leading edge of a flat plate with regards to different features of the flat plate such as the flap length. This study was followed by wind tunnel testing to verify some of the computational results. As it was mentioned in the preceding paragraph, most flat plate leading edges use classical geometries, which are mostly symmetrical. However, Hanson's study used an asymmetrical configuration of modified super ellipses. Hanson's thought to use a modified super ellipse (MSE) is not new, this term was actually made popular by Haddad [Haddad and Corke, 1998]. In an effort to establish a physical view of the terminology surrounding the flat plate geometry, please refer to figure 12.

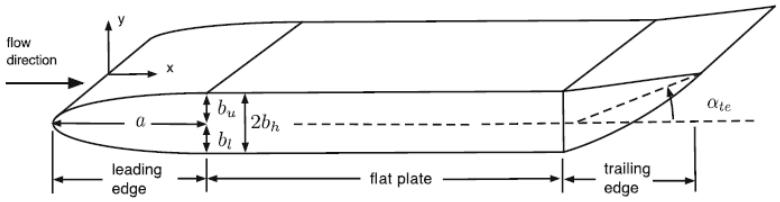

Figure 12: Overview of Parametric Optimization of Leading Edge Profile [Hanson et al., 2012]

The aforementioned study conducted their study by varying the b_u and b_l ratios along with the respective lengths of the "flat plate" and "trailing edge", relative to figure 12. The optimization procedure also varied the α_{te}, this quantity shifts the stagnation point at the leading edge, according to theory an angle in the positive direction (counterclockwise) would shift the stagnation point towards the top portion of the flat plate, in the direction streamwise to the flow. α_{te} is the angle that the mid section of the constant thickness region of the "flat plate" on figure 12 makes with the centerline of the trailing edge [Hanson et al., 2012]. Furthermore, the mathematical relations that characterize the modified super ellipse which were used to couple these dimensions are the following. The MSE profile with the optimal performance was not symmetric. The study defined the differing upper and lower profiles as, MSE_u and MSE_l, respectively. According to the parametric study they also recommended a $b_u/2b_h$ to be $1/3$.

$$\left(1 - \frac{x}{(AR * b_h)}\right)^{m(x)} + \left(\frac{y}{b_h}\right)^{n} = 1, \quad 0 < \frac{x}{b_h} < AR \tag{2.6}$$

$$m\left(x\right) = 2 + \left[\frac{x}{AR * b_h}\right]^2, \quad n = 2 \tag{2.7}$$

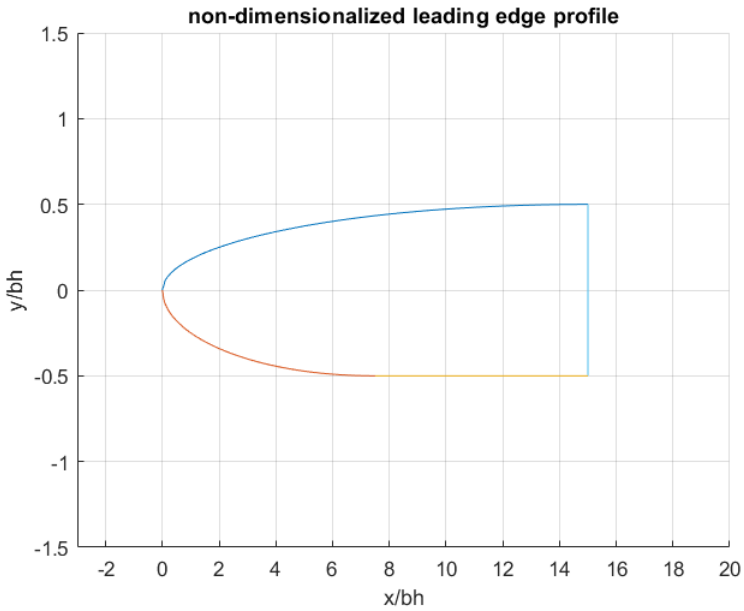

Figure 13: Leading Edge Profile for 3.65-meter Test Section

Figure 13 is the leading edge profile normalized by half of the constant thickness dimension of the flat plate. The LE profile, was designed by taking relations 2.6 and 2.7, while assuming an MSE_u of 30 and MSE_l of 15. In addition, the study recommended that the thickness of the flat plate should be 0.67% of the chord, however this amounted to 24.51-mm (0.9648-in), instead the flat plate thickness that was built actually has a nominal thickness of 25.4-mm (1 inch). The reason for this was the difficulty in acquiring material of this thickness along with the complications in custom making them in the UIUC aerospace machine shop. It was decided it was best to sacrifice a "perfect thickness" rather than end up with a flat plate that had a varying thickness from the machine converting it from 25.4-mm to 24.41-mm. According to Hanson, with reference to figure 12. a had to be 10% of the entire chord of the flat plate, the length of the trailing edge is also recommended to be 15% of the chord, this served as a baseline for how long the features of the flat plate should be. The leading edge length is a function of the distance between the tip and the location where the curvature ends and where the constant thickness commences. On figure 13 these two points are represented as coordinate (0,0) and $x/b_h \approx 12$. Thus, in the physical model, the leading edge length was 152.4 $\pm$.03-mm (6-inches) and the trailing edge length was 548.64 $\pm$.03-mm (21.6-in). Figures 14 and 15 show the CAD of the leading edge and trailing edge, respectively. SolidWorks was the software which was used to produce the physical model of the flat plate. Figure 14b shows the dowel slots which held the LE in place. This tunnel contained a 0.381x0.381-meter (15x15-inch) cross section, which means that the flat plate by default had to have a width of 0.381-meters, in the spanwise direction. However, the electronic discharge machine (EDM) that was used to machine the leading edge profile had a constraint which prompted the leading edge to be carved in two different pieces, hence the dowels. The trailing edge (TE) is theoretically a triangle that converges at zero but a radius of curvature had to be established that was based off the limits of the same EDM machine that was used. The leading edge and trailing edge profiles were created using MATLAB scripts, the discretization or resolution of the points that are used to create each contour depended on the size step that the user desired. However, the machine which was used had a specific limit of discretization points, which meant that curves had to be smoothed out. Draftsight was the software used to collapse the curves and SolidWorks was used as the middle software to create the 2D curves created by MATLAB into

a 3D product. This procedure of simplifying the curves evidently led to a degree of roughness which is planned to be quantified using a profilometer.

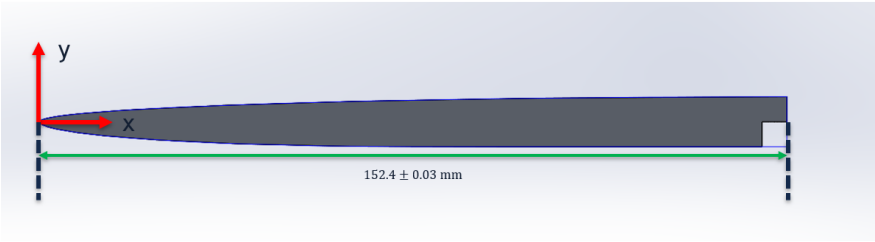

(a) Streamwise View of LE Profile

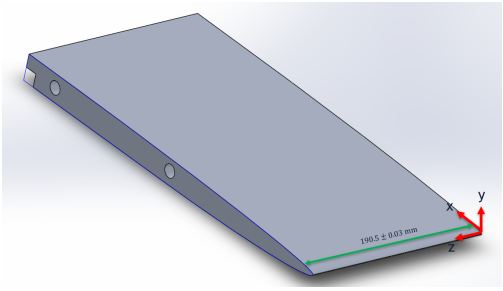

(b) Isometric View of LE Profile

Figure 14: Leading Edge CAD for 3.65-meter Test Section

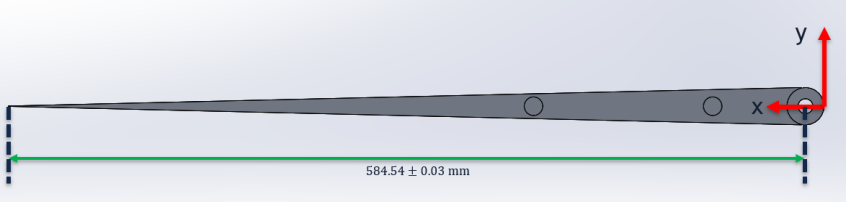

Figure 15: Trailing Edge CAD for 3.65-meter Test Section

Figure 16 depicts the flat plate as a whole. Sections 1, 2, 4, and 5 are 6061 aluminum alloy, while section 3 is acrylic.

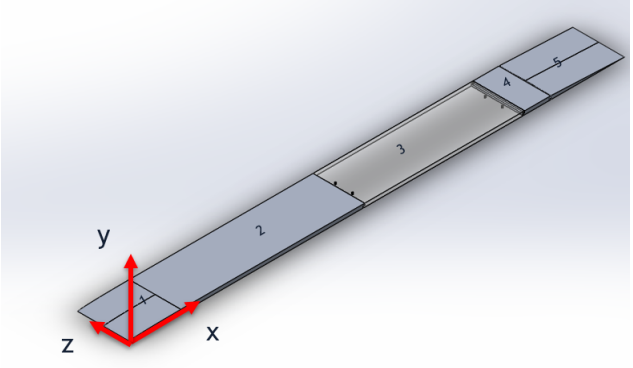

Figure 16: Entire Flat Plate CAD for 3.65-meter Test Section

2.2.4 Trailing Edge Design and Stagnation Point Location

The preceding paragraph described the methodology in designing the flat plate, which was driven from the desired length of 3.65-meters and the LE profile. It was also, said that the stagnation point at a zero angle of attack can be mandated by the position of the TE. In other words this position can be described by α_{te} on figure 12. This is similar to how an airfoil can have a different coefficient of lift as a function of the flap angle. This leads to a change in the pressure distribution over the surface of the airfoil. Now imagining that the airfoil is not symmetric but rather the LE resembles the profile specified in the preceding chapter, then a viable way of altering the pressure distribution of said non-symmetric airfoil would be to alter the flap (or TE) angle, assuming a zero angle of attack. Hanson showed that increasing the trailing edge flap in the counter-clockwise direction tends to shift the stagnation point downstream [Hanson et al., 2012]. It is also important to note that the range of trailing edge deflection was 0 to 2.55 degrees, a moderate amount. Fransson [Fransson et al., 2004] similarly to Hanson was able to show that increasing the flap angle in the counter-clockwise direction had a significant impact on the leading edge suction peak of a flat plate. Fransson ran his study for a 1-meter plate at 5m/s, and the optimal trailing edge deflection angle was 1 degree, a moderate amount as well.

For a more in depth look on the mathematical nature of the behaviour of flow at LE based on the TE of a flat plate refer to Stewartson [Stewartson, 1969], in which they discuss this behavior using Goldstein's theory on inflow conditions and their implications in the boundary layer [Goldstein and Hultgren, 1987]. One of the main takeaways includes that as the thickness of the trailing edge approaches zero, then the velocity that comes immediately aft of it also asymptotes to the freestream velocity. Thus, an inherent optimization problem is to make the trailing edge of the flat plate as thin as possible while taking into account structural integrity and machining capabilities. This is also seen in commercial airfoils [Satyanarayana and Davis, 1978], [Perry and Mueller, 1987].

Now, returning back the attention to the TSF facility. A tool was created to raise the trailing edge of the TSF flat plate, this can be seen on figure 17. The direction of flow on this image is from left to right. The following method was used to pinpoint the center of the trailing edge, which was denoted as the zero angle. First, the bolt is the dark grey circle near the middle semi-circle created by the protractor. This bolt was the hinge which is connected to the triangular piece of the TE, this piece can be seen on figure 15, where the coordinate axis is located. A line was drawn using the center location of the bolt as a reference to mark the centerline of the flat plate, fore of the bolt, which can be seen on figure 17. The 5 dashed dots on the TE at the right side of the image indicate the locations in which the thickness of the plate was measured then the half distance was taken for each of these places. This was done using a caliper. Then a straight line was drawn to indicate the centerline of the TE. Finally, the protractor was placed to measure the angle of inclination of the flap relative to the middle part of the flat plate, establishing the zero angle of deflection. The support that is able to keep an angle of inclination, is also visible on figure 17. There is an identical TE lifting mechanism on the opposite side of the TS. Both are the identical in height and provide two points of support for the trailing edge, to maintain stability and mitigate vibration. Figure 18 also shows this TE raising mechanism however in this image it is purposefully not making contact with the TE, to allow the reader to see its purpose.

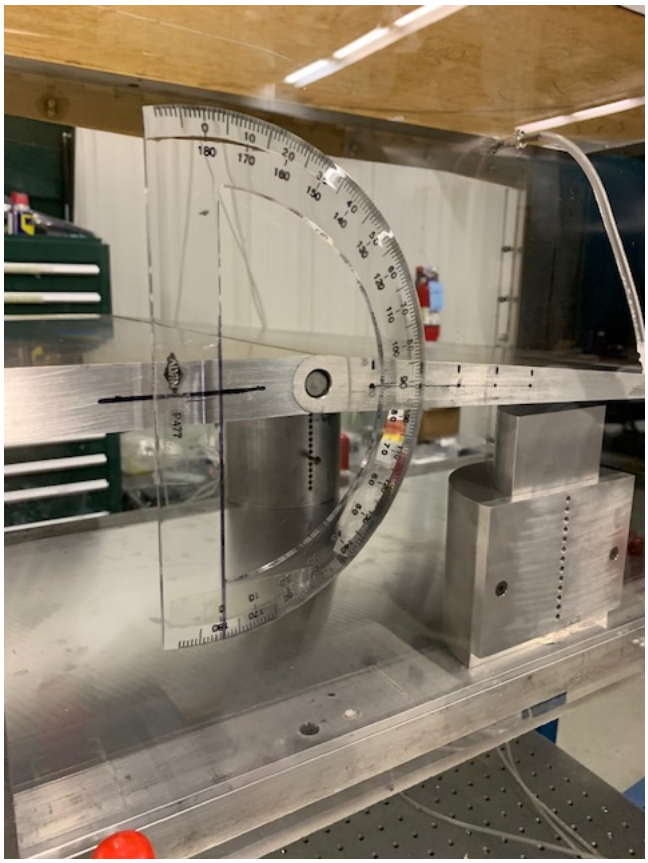

Figure 17: Trailing Edge Raiser with Protractor

2.3 Flat Plate Design for Manufacturability and Ease of Modification

Section 2.2 as its title suggests focused on the theoretical considerations of the LE and TE profiles. In this subsection, we will discuss the manufacturing process of the full plate, as well as the design considerations to enable the plate to be substituted or modified in the future. Figures 14 and 15 show the LE and TE respectively; it was mentioned that these profiles had to be quite precise in order to obtain the proper flow conditions when the tunnel is running. These pieces were manufactured using an EDM machine. From figure 16 the second and third pieces, aluminum and acrylic respectively, are the longest pieces. These were made using a standard mill, given their length, approximately 1.36 and 1.18-meters, respectively. The first piece is aluminum, during the grinding process, it is relatively simple to cut, acrylic is more brittle. This was the reason it was opted to use an easier-to-find thickness of 25.4-mm.

Shifting our attention to the support of the flat plate, which are made obvious on figure 18. The c-stand was designed to hold up the flat plate and this stand is fixed to the floor of the test section. Now, from under the c-stand are slots in which a 1/4-20 machine-threaded bolt can reach into the flat plate. The c-stands can be seen on figure 18, one is traced in a green dashed line, 1 and 3 are considered the legs, and 2 which runs spanwise is the table. Between the flat plate and the c-stand lies room in which washers can be placed to improve the height and level the flat plate if necessary. The green circled area of image of figure 18 shows slots. These allow flexibility for the entire flat plate to move in the streamwise direction (flow is from left to right on these images). In addition, as depicted on figure 16

the flat plate was made into different parts, partially to prepare for a future experiment that could require a shift or swapping of components. The flat plate has 3 different joints which allow swapping of parts. The three red circles on the top portion figure 18 shows these.

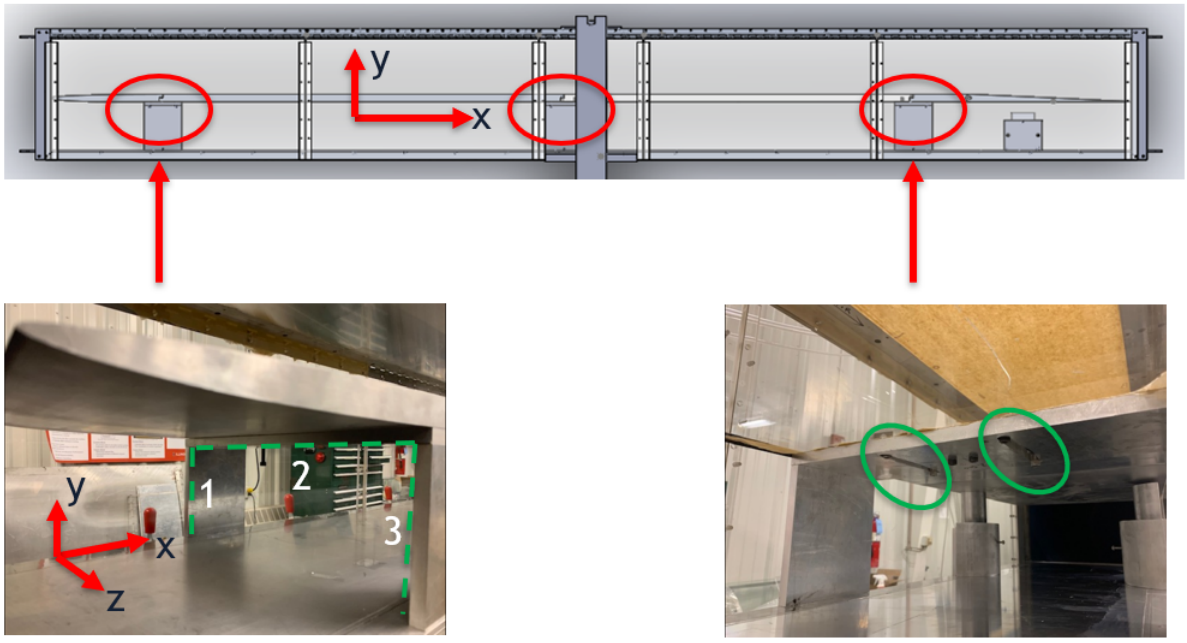

Figure 18: Component Joints on Flat Plate

Furthermore, protruding into the top side of the flat plate was avoided to not disturb the flow. The screws on figure 18 were not completely fastened into their respective positions for the purpose of the reader being able to see where they are located. This also makes it obvious how easy it is to remove these screws and unclasp the flat plate from the c-stand support structures. The red arrow on figure 19 shows how the fourth component attaches to the preceding acrylic portion of the flat plate, or component 3 on figure 16. For reference, on figure 19 the side which the reader can see is the top side of the flat plate which sees the flow, and the fluid moves from left to right. The blue arrow shows part of the circle which facilitates the adaptation of a hinge-like structure to be added aft of it. The position of the trailing edge depicted in the previous images is expected to remain static during the duration of the standard characterization experiments. However, other potential experiments may need to replacing the trailing edge to place a dynamic flap to induce an unsteady perturbation to the pressure gradient. This would mean the last portion of the flat plate would have to be swapped for a flap that would allow a servo or another mechanism to shift the piece using the current hinge line as the same axis of rotation in a periodic or unsteady fashion. In order to do this the bolts that connect the c-stand to the flat plate would have to be removed. Now for the TE or component 5 on figure 16 it is recommended to remove not only the wedge (figure 15) but the entire piece (including figure 19), otherwise the only way to remove this would be to extract the hinge rod which could pose problems.

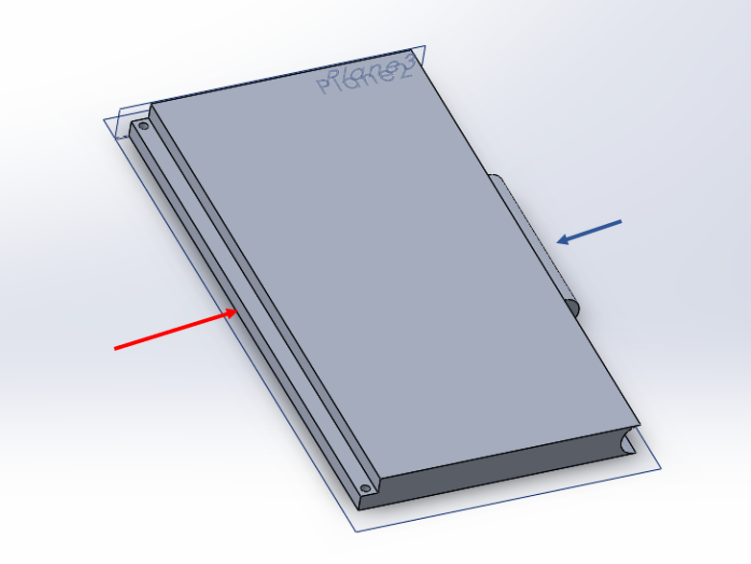

Figure 19: Sample of Joints Located on Flat Plate

The c-stands are not only a robust support system for the flat plate but they can also serve as a guide to place additional static pressure taps for the wind tunnel. Figure 18 shows a broad view of the flat plate sitting in the middle of the test section. The most opportune location to take pressure measurements or orientate the field of view for optics is in the centerline, due to the distance away from the sidewalls whose boundary layer can contaminate results. If in the future pressure taps were to be placed flushed to the portion of the flat plate which sees the flow this could be possible, bringing them from underneath and through the thickness of the flat plate in the y-direction. The flat plate reaches both sides of the test section's walls in the spanwise direction. Since the top portion of the flat plate is the region of interest, the location or the tubing that comes along with the pressure taps could either trace the underside of the flat plate in the spanwise direction along the C stands and have it exit out the tunnel onto the pressure transducer. Furthermore, as in the same way an airfoil, the pressure distribution is a result of the top and bottom surfaces. With this in mind, the c-stands can cause an adverse effect on the flow within the WT, but the thickness which is perpendicular to the flow is only 12.7-mm for both the c-stand's legs and table.

2.4 Optical Access for PIV

The main diagnostic technique for this WT is PIV. This section will deliver background information on the primary steps to take when starting PIV, as well as the overall physics behind the method. It will then be followed by the steps taken in order to enable this TS for PIV from different angles, while reducing potential obstacles to the field of view.

2.4.1 General PIV Background

Particle Image Velocimetry (PIV) was the successor of Laser Doppler Velocimetry (LDV) which deduced velocity measurements by taking the doppler shift in a laser beam. LDV was popularized in 1965 by Bell Labs. This was a prominent method in the experimental fluid mechanics community for several decades, it was also used in studying

turbulence [Lyn et al., 1995] among a plethora of other problems related to fluid mechanics. An even older predecessor of both methods is hot-wire anemometry. This uses a hot wire which cools as the flow passes on it. There is a relationship between the resistance of the wire and flow speed. The exact origin of this technique is not well known but it is believed to have occurred between 1900-1920 [Comte-Bellot, 1976]. PIV uses high-powered lasers, such as Nd:Yag laser, which is a solid-state laser. Modern lasers allow double pulses, this refers to the time between each pulse. This time can range from milliseconds to nanoseconds. The required time between the pulses depends on the speed of the flow which you are trying to measure. The slower the speed, the longer the delay can be within pulses, which means the light beam will increase (or recharge). The available power of the laser at each pulse, has a direct effect on the resolution of your images. When the trigger occurs some lasers can have a pulse up to 100 Hz, others may be at 10 Hz. The desired frequency is a function of the speed of the flow and of the delay between the pulses. The actual value of the frequency depends on the laser as well, other lasers used in PIV are known as Nd:YLF lasers. Figure 20 is used as a basic example of how the laser and camera aperture work in unison to obtain quality images at such high rates. The top plot exhibits the advantage of having a double pulse laser, as it can essentially provide an impulse within different frames, relative to when the camera's aperture is open. Also, it is necessary to take notice of how small the time between pulses is, as it was said before, these instruments operate at a fast rate. The lower image on figure 20 represents the duration in which the camera has its shutter open. Relative to the upper image it can be seen that the laser pulse is very small compared to the aperture time. Thus, the greater concern is with regards to the ability for the laser to have enough energy when it pulses. The x-axis for both plots is in milliseconds. The y-axis on the top image can be thought of as a fractional value of the actual power over the available power of the laser for the top plot. Depending on the timing between pulses (does not have to be 9-nanoseconds), the power available will change.

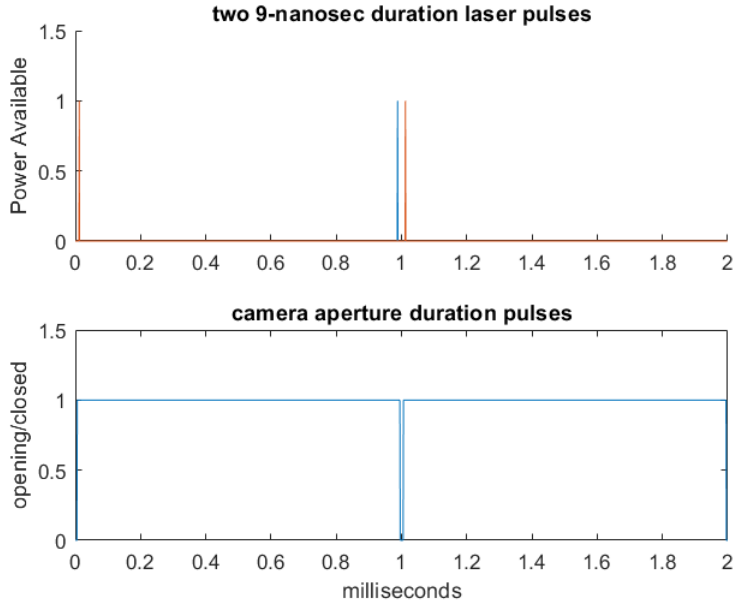

Figure 20: Generic Example of Laser Pulse vs Camera Aperture Pulse

There are different ways which light can scatter involving different mediums, for example Rayleigh [Young, 1981], and Mie scattering [Wiscombe, 1980] among other types. For reference, PIV uses Mie scattering, it contains more intensity than Rayleigh scattering. Figure 21 is a common plot which denotes the incident light angle θ as a function

of the intensity of the light that is being scattered. Note that at 180 degrees the intensity is the greatest, this is known as forward scattering. The scattering of light at 0 degrees is referred to as backward scattering. The arbitrary intensity values, are on the log-scale.

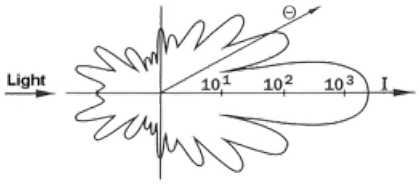

Figure 21: Incident Light vs Scattered Light Intensity [LaVision, 2020]

Figure 22 shows a generic illustration of one of the ways the laser would be able to create a laser sheet in the TSF TS. First, figure 22, shows a view into the cross section of the wind tunnel, essentially the flow is going into the page. The laser beam starts on the lower left region of the figure, the first two mirrors are flat mirrors, meaning they simply redirect the light coming from the laser to be placed overhead so it can illuminate the centerline of the tunnel which is the location that the flow would be the less disturbed from the presence of the sidewalls. The third mirror would be a cylindrical mirror to collimate the beam into a laser sheet. The movement of the flow would then be captured by the camera on the right-hand side of the image. The angle between the laser sheet and the position of the cameras is at 90 degrees. The principle of Mie scattering lies on the fact that when light encounters a sphere or any type of material it bends or scatters the light. What the camera sees is the bending of light, as a result during an experimental run, it is good practice to darken or blacken out the area of interest in which the camera is taking images of. This mitigates the light from bending around unexpected items which can then shine into the camera sensor, and contaminate results. In addition to the mirrors in figure 22, an iris can also be used to re-orientate or seemingly intensify the light beam. An iris effectively does this by using the differing density gradient within the laser beam. After a satisfactory laser path is established, seeding particles are then used to essentially become illuminated by the laser, and these are flow tracking particles from which the cameras take pictures of, these are the objects which act as the central piece for the Mie scattering technique. The size of the particles depend on the flow velocity that they are going to be placed into. The flow speed inherently mandates the rate at which these particles will move as a function of time, if you have a faster flow you will need smaller particles if you want to maintain a reasonable field of view [Ragni et al., 2011]. However, your particle that must also large enough to produce a reasonable incident refraction of light, this provides a low signal-to-noise ratio [Melling, 1997].

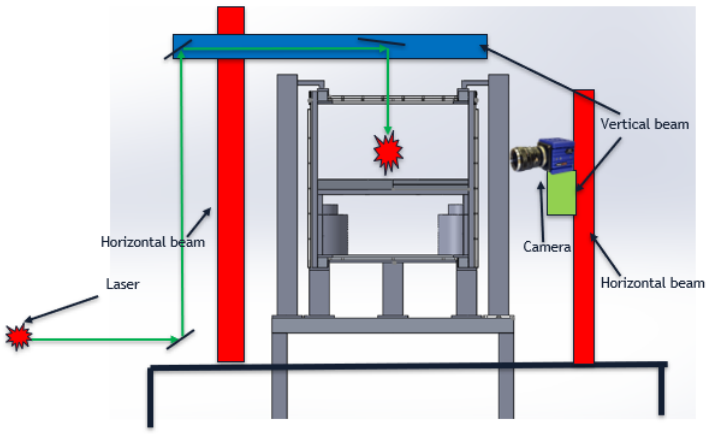

Figure 22: Proposed Laser Beam Path to illuminate Flow

More will be said about the tracing particles. However, it is important to bridge what has been said regarding: lights, cameras, and particles to the notion of interogation windows (IW) that the camera sees during experimental runs. A simple example of this can be seen in figure 23. It is self evident that the IWs must overlap each other to some degree to form a continuous set of data, whether it is spatially or temporally resolved.

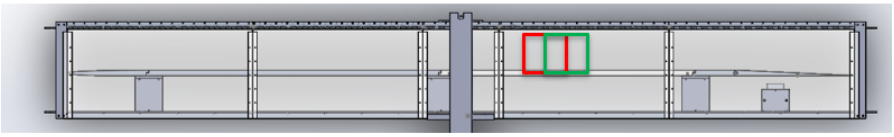

Figure 23: Example of Interrogation Windows

Figure 24 shows the amount of cameras needed to configure a 2D PIV, stereoscopic and tomographic PIV setup, respectively. From Figure 21 based on the angle of the scattered light relative to the incident light source, there is a plethora of options to situate cameras to successfully observe what is going on within the test section. A takeaway from figure 24 is that by placing the cameras in the b and c position creates a thickness that straddles the centerline where the collimated laser sheet is. In the figure the a, b and c orientations allow for quantification of the flow in the spanwise direction while image d allow the same as c but the sheet changes directions. For figure 24 the c and d setups allow for ability to quantify velocity vectors in the z direction, essentially a 3D view of velocity. As part of the PIV procedure, once the field of view and region of interest are pinpointed, the cameras and scheimpflug angle can calibrated [Louhichi et al., 2007]. The scheimpflug angle is a function of the location where the front of the lens is pointed along with the camera's sensor. On figure 24 the blue box contains the sensor, this is located at the front of the box (closes to the TS) right before the black cylinder object, which is the lens. The camera depicted in this figure is a LaVision product, Imager sCMOS [LaVision, 2020].

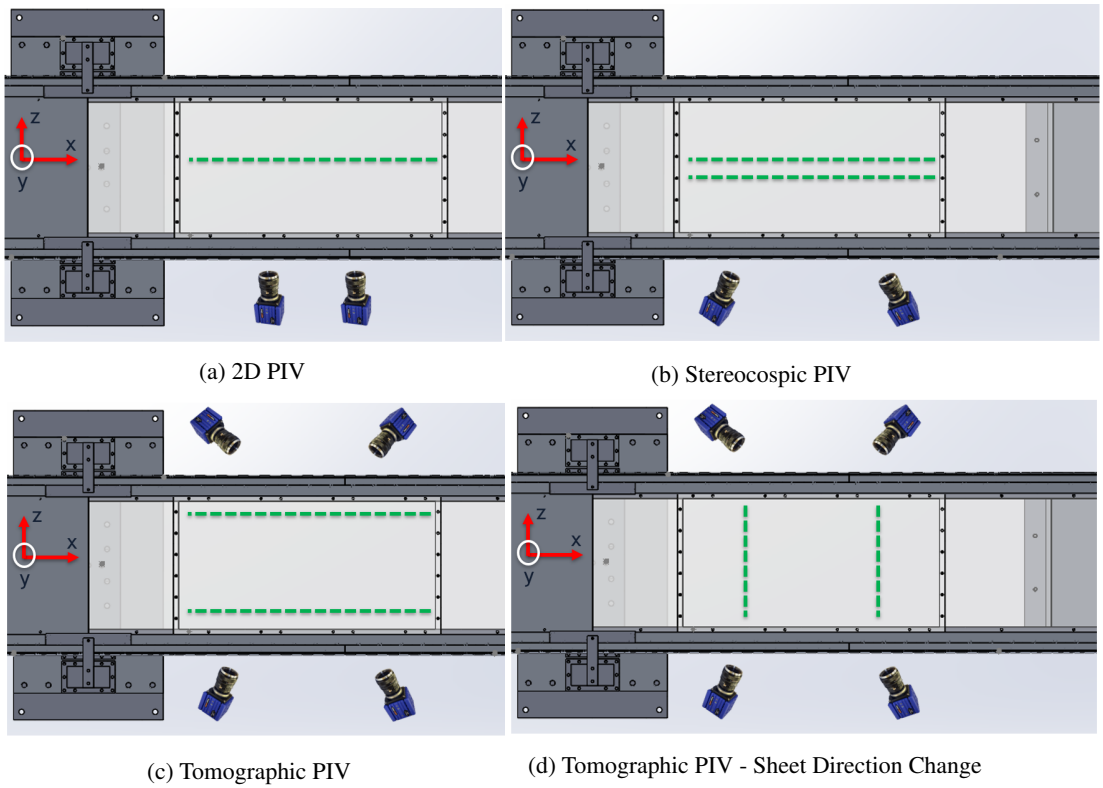

(a) 2D PIV

(b) Stereocospic PIV

(c) Tomographic PIV

(d) Tomographic PIV - Sheet Direction Change

Figure 24: Potential Camera Placements for PIV

Furthermore, as it was mentioned above there are different constraints that mandate what are the proper seeding particles to use in order to effectively trace the flow. Naturally, the seeding particles that are used to emulate fluid elements will never contain the exact density or speed and shape of them. One can begin to understand the relationship between the relative velocity discrepancy between the fluid element and seeding particle by observing the following relation. This is known as the Basset-Boussinesq-Oseen equation [Ragni et al., 2011] given as

$$\frac{\pi d_p^3}{6}\rho_p\frac{d\hat{U_p}}{dt} = -3\pi\mu d_p\hat{V} + \frac{\pi d_p^3}{6}\rho_f\frac{d\hat{U_f}}{dt} - \frac{1}{2} * \frac{\pi d_p^3}{6}\rho_f\frac{d\hat{V}}{dt} - \frac{3}{2}d_p^2(\pi\mu\rho_f)^{\frac{1}{2}}\int_{t_0}^{t}\frac{d\hat{V}}{d\zeta}\frac{d\zeta}{(t-\zeta)^{\frac{1}{2}}} \tag{2.8}$$

with d_p, ρ_p, $\hat{U_p}$, being the effective particle diameter, density and velocity vector of the particle. Furthermore, ρ_f and $\hat{U_f}$ are the same quantities but for the fluid elements. The first and second terms of equation 2.8 show the acceleration force and viscous resistance of the of the seeding particle per Stokes law. The third term represents the acceleration of the fluid which leads to a pressure gradient, and the fourth is the fluid displacement due to inertia, and the fifth term is the unsteadiness forces which are created by acceleration [Ragni et al., 2011]. For incompressible flows especially turbulence it is difficult to analytically solve this equation, due to the uncertainty of what the appropriate flow velocity should be for different scenarios, especially when turbulence comes into play. However, it is interesting to note that this is one way that the difference between fluid elements and seeding particles can be represented. Figure 25 is a visual schematic of the relative velocities between the fluid and the actual fluid elements that have been discussed.

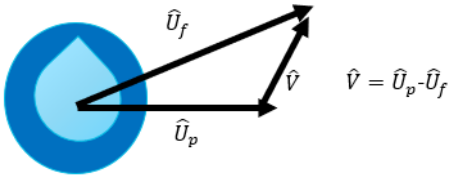

Figure 25: Illustration Highlighting Fluid and Seeding Particle Discrepancy

To further extend the comparison between different seeding particles, one can use Stokes number which is commonly used. As it was described in earlier paragraphs this is a non-dimensional quantity that is composed of different characteristic lengths and or time scales that are dependent and can be adapted to different situations. Stokes number Stk can be represented as a dimensionless ratio of the particle relaxation time and the relaxation time of the fluid, τ_p, τ_f respectively. δ is the the boundary layer thickness. μ_f is the dynamic viscosity of the fluid.

$$Stk = \frac{\tau_p}{\tau_f} \tag{2.9}$$

$$\tau_f = \frac{\delta}{U_\infty} \tag{2.10}$$

$$\tau_p = \frac{\rho_p d_p^2}{18\mu_f} \tag{2.11}$$

In supersonic and hypersonic flows the density of the seeding particle must be much greater than the density of the fluid, this is a result of the flow undergoing rapid changes in acceleration [Ragni et al., 2011]. However, in incompressible flows this ratio must be closer to 1, it is actually quite common to use smoke and oil particles as seeding particles [Hambleton et al., 2006], [Raffel and Kost, 1998]. The figures shown below were taken at a research facility managed by the Air Force Research Labs, at AEDC, at Mach 5 flow. The gray blotches are seeding particles, as seen through PIV. Both images are up to scale but the one on the left had a higher content of humidity which caused the particles to bunch up. These larger structures negatively affect the quality of the images as the flow features are not seen as clearly. This issue is more common with high-speed flows since they typically use 'dry' compounds such as silicon dioxide and titanium dioxide [Ragni et al., 2011]. The red incidents signal regions of high intensity for the camera which can damage its sensor.

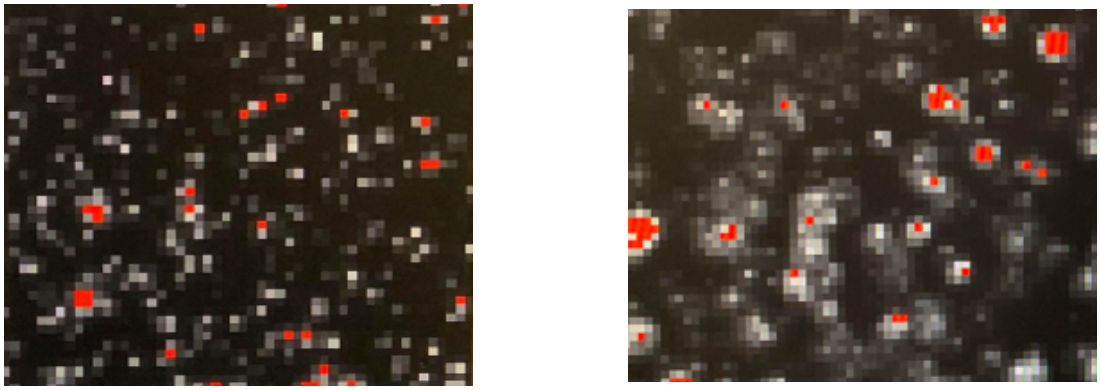

(a) Non-Agglomerated Particles

(b) Agglomerated Particles

Figure 26: Seeding Particles and Agglomeration

The information presented in this sub section only scratches the surface of what is in literature, there is an entire community dedicated to studying the optimal type of seeding particles that should be used for different situations. In summary, setting up for PIV is a recursive process, mirrors must be set up, the laser has to have its power rated, then the camera must be calibrated with the calibration block present at the centerline or wherever the field of interest is. This includes having the schleimpflug and the camera sensor properly orientated. The frequency of the cameras aperture and the laser pulse must be synchronized, this is also dependent of the flow speed and the length of the experimental run. Furthermore, the seeding particle and mechanism has to be configured. The location and frequency of emission for the chosen seeding particle also depends on the flow feature you are studying. For example, in turbulence the flow is not uniform, which is an inherent property of turbulence, thus properly placing seeding particles into these types of boundary layers can also be challenging. PIV is a method that has to go through a trial and error period before the first successful run occurs. These are just some of the main, high level tasks that must occur before running a PIV experiment.

2.4.2 Optical Material Considerations and Minimization of Interference

This subsection will explain the reason for the materials used to allow for PIV. The design decisions that were taken to minimize interference from non essential objects to optics, such as the support structures. The following image shows an isometric view of the tunnel to highlight the different materials that were used to build the TS. It is easy to identify the flat plate in the middle of the TS, for reference the isolated flat plate is located on figure 16. The x coordinate identifies the streamwise direction, the y is in the wall-normal direction, and the z coordinate is in the spanwise direction. Starting from the left, the region of the fourth window is the region of interest where most of optical equipment will be directed towards. This is further obvious by the acrylic piece of the flat plate and the entire aft piece of the roof is also acrylic, featuring an acrylic insert that stands out located on the roof. Now, going back to figure 22, the light beam goes through air until after the third mirror. It is safe to assume that the incident of light between the air and across the mirror is monotonous or negligible assuming a homogeneous mixture of air, which by standard conditions is 78, 21, 0.9, and 0.04 percent nitrogen, oxygen, argon and carbon dioxide, respectively [North Carolina State Climate Office, 2016]. However, as the light crosses through the glass the thermal, optical and mechanical properties of the medium in which the light crosses the medium play a significant role. In this case, acrylic was used, there is an incident angle between the air and the acrylic. In addition, the reflection of the laser light from

the selected surface can affect the quality of the image that the camera obtains. If the reflected rays are too intense they can also damage the camera sensor.

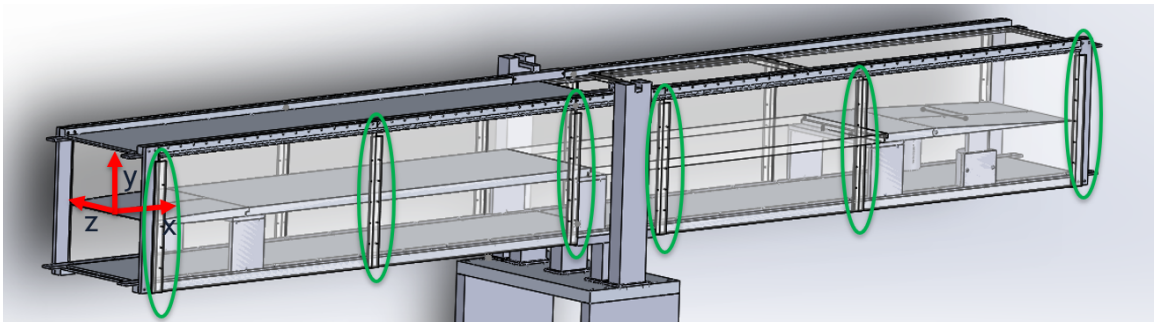

Figure 27: Isometric View of Compiled Wind Tunnel

There are different ways in which these problems can get mitigated. Three of these techniques include choosing a material that: absorbs the beam energy of the laser, pulls the specular reflection of the incident beam away from the camera, and/or efficiently transmits the beam energy [Paterna et al., 2013]. Paterna's study conducted these three approaches to reducing the specular reflection using a variety of different materials among these was acrylic both as reflecting material and a transmitting one. Initially the acrylic portion for the TSF group's flat plate was going to be aluminum, so the surface was going to be painted black. This way the flat plate could absorb the energy and not have regions of high intensity negatively impact the quality of the images or damage the camera's sensor. Specular reflection is the theory that for every wave of light that hits a surface a normal ray to the surface is created. Eventually the diffusion of such rays, or light that is not accounted for can saturate the camera sensor or cause regions of high intensity within the images. This type of reflection can be substantially reduced by ensuring a smooth surface, with wrinkles less than 50-nm which can be verified by using a profilometer [Paterna et al., 2013]. For the set up used in TSF's lab several 25.4-mm (1-inch) flat quartz-glass mirrors were purchased from Thorlabs and were Nd:Yag rated. These items were intended to reflect the laser beam and eventually collimate it prior to it entering the test section. Glass was the optimum material with regards to the reflection reduction coefficient in the reflecting materials section that were tested [Paterna et al., 2013]. A 16-bit camera is scheduled to be used by the TSF group, however the previously mentioned study used a 12-bit camera. The glass was also the material that was able to scatter light with the least amount of saturation reaching the camera's sensor, according to Paterna [Paterna et al., 2013]. Furthermore, as it is depicted on figure 27 the windows, aft roof and insert, and the third piece of the flat plate (as shown on figure 16) are acrylic.The purpose of these is to transmit the collimated laser beam into the test section then have them illuminate the particles so the camera can take images of the flow structures that are forming when the wind tunnel is executing an experiment. In the transmitting materials of Paterno's campaign acrylic came in second with regards to glass. Glass could have been used in the TSF wind tunnel design, however a requirement of this wind tunnel was to allow for all of the side walls to be able to be used with optics simply for flexibility in allowing different types of experiments. It is true that the flat plate pieces upstream of the acrylic piece of the flat plate are aluminum but in the previous section it was discussed how simple it was to detach them. The aluminum portions could terefore be replaced with more PIV-apt materials, or even painted black. The entire flat plate and its stands could also be removed and maybe a study revolving a set of propellers or an airfoil could take place. If the wake off an object were to be studied a longer field of view may be needed, and this test section allows it. The ceilings and roofs in all of the locations can also be removed and easily replaced by different materials. For example if the fore roof and floor were to be replaced with acrylic this could also easily be done.

When the tunnel was inherited the diffuser and the settling chamber were already present so the ends of the test section were designed in such a way that they could easily be adapted to these set pieces. This mandated the dimensions of the windows, in order to properly have an air tight facility and have them open easily by the hinge, the windows had to be 17.5-mm in thickness. From the LE, the first and fourth (per figure 27 acrylic windows were nominally 0.859-meters in length and 0.411-meters in height, these also had a specific profile that allowed for them to be inserted into the support structure of the TS. Figure 28 depicts the gap (red circle) which required the 17.5-mm thickness (green circle), and it also shows the flexibility in the opening of the windows.

Figure 28: Aft Acrylic Windows in the Test Section

Table 1 below shows the different variables that were taken into consideration when the sidewalls were chosen, fracture toughness, density and cost. The first row's acronym $F.T$ is the fracture toughness of each respective material. Fracture toughness deals with crack propagation [Geandier et al., 2003]. The logic behind acquiring this information was that during machining the hole for a pressure tap or tapped holes for the hinge line, a crack could potentially occur. The total weight of the materials was also taken into consideration to decrease the load the middle support structure had to carry, this will be discussed in greater in detail in chapter 4. The densities of each respective material are also tabulated below.

Property	Silica-Glass	Acrylic
F.T $mpa * m^{1/2}$	0.75	1.2
$\rho \frac{kg}{m^3}$	2200	1400
$\$USD/cm^3$	5757	10
Refractive Index	1.46	1.49

Table 1: Different Properties of Glass and Acrylic [Gere and Goodno, 2013]

Another consideration that favored the selection of acrylic was the higher heat capacity in allowing for the insertion of pressure taps by a rapid spinning mill. Using glass inserts instead of all acrylic was also taken into consideration. However, viewing an experiment from different angles and thru different mediums such as glass and acrylic would create a change in index of refraction. This could introduce issues. Even inserts to ensure an air tight facility were made of acrylic, these can be seen on figure 27 circled in green. Furthermore, going back to figure 22, the laser light goes from air into the medium (acrylic) before it goes into the test section. Light contains photons which interact with electrons through the medium, if the latter contains regions of high density of electrons then the photons will move

more slowly. Now, absorption by the medium occurs when the incoming photon contains enough energy to properly excite the electron. The electron is thus elevated to the next higher state, and any light that is not absorbed or reflected at the surface will be transmitted. Thus, a lower refractive index is favorable, but a higher rate of transmission can mean that the medium has a higher absorption index and a lower amount of reflection occurs at the surface. Typically acrylic can have a transmission percentage up to 93 percent, and silica-glass can have this figure up to 92 percent [Gere and Goodno, 2013]. Figure 29 is a generic representation of the incident ray and the effect of refraction.

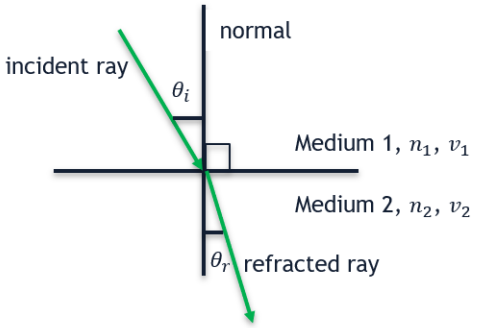

Figure 29: Generic Example of Light Bending Through 2 Different Mediums

Figure 29 shows several quantities, such as n_1, n_2, v_1, v_2, the n stands for the index of refraction for medium 1 and medium 2, v is the speed of light depending on the medium. The respective θ_1 and θ_2 represent the angle in which the light bends respective to the normal. The following formulas show the mathematical relationship between these variables, this law is also known as Snell's law [Paterna et al., 2013]. The interested reader can refer to Griffiths [Griffiths, 1968] for more information on how the laser light acts as an incident light and scatters through the presence of air molecules or other materials and objects.

$$\frac{n_1}{n_2} = \frac{v_2}{v_1} \tag{2.12}$$

$$n_1 \sin\theta_1 = n_2 \sin\theta_2 \tag{2.13}$$

It has been mentioned prime requirement of the design of this test section was to minimize optical interference, mainly to allow for flexibility to accommodate different experiments in the future. Figure 30, shows the CAD without the acrylic windows. This is done to differentiate between these and the supporting structures. Flow goes from left to right, the middle of the image depicts the upper part of the main support system, which will be discussed later in the chapter 4. It is beneficial that the test section does not contain any supporting beams apart from the middle piece and the ends which connect to the diffuser (right end) and the settling chamber (left end) of the wind tunnel. The red vertical dimension details the height of optical access between the upper surface of the flat plate and the hinge from which the acrylic windows latch on. Now, these measurements are solely for this configuration meaning that the flat plate is present in the test section and is supported by the c-stands. Now, the distance shown by the green arrow between the floor and the roof, in which the flow is free to develop is 381-mm which was mentioned at the beginning of this chapter.

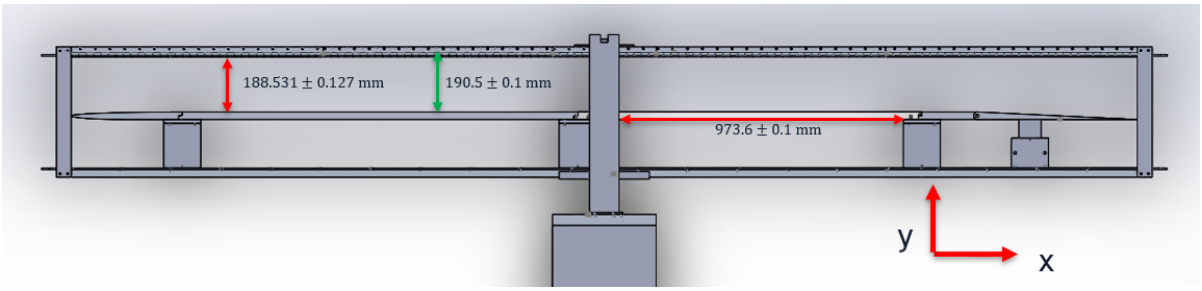

Figure 30: Streamwise View of the Test Section for Optical Purpose

In figure 30, one sees how the c-stands, or the supports of the flat plate, do not impede the optics that can be used for potential campaigns in this test section. For example, figure 24d shows a potential experiment which would focus on analyzing flow mechanics in the spanwise direction, contrasting to the streamwise focused experiments that are assumed by figure 24a, 24b and 24c. The main support beam in the middle does indeed impede some of the acrylic plate from being used, however the vast majority is still available. The main limiting factor for the acrylic region of the flat plate is not necessarily the main support, but the start of the ceiling upstream of the key test area, and the main aft limitation is the start of the TE piece, as demonstrated in figure 31. These are limiting factors because they are not acrylic, but rather 6061 aluminum alloy, which is not an ideal material to use for optics.

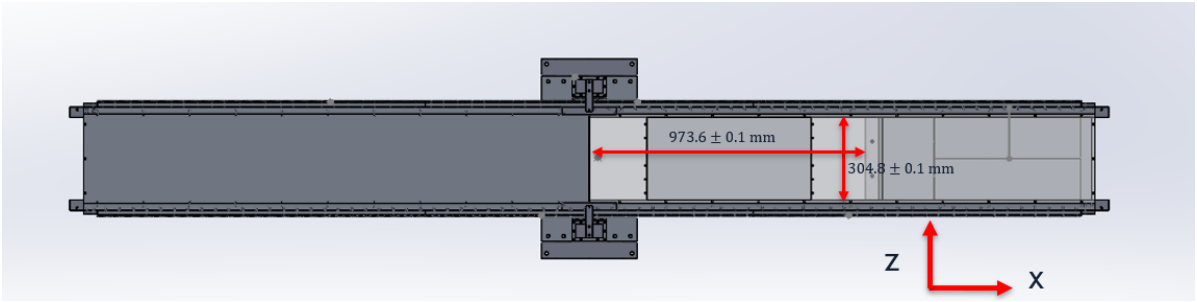

Figure 31: Overhead View of the Test Section

2.5 Flexibility of Wind Tunnel

2.5.1 Acrylic Windows Versatility

A somewhat unique feature of this test section is the flexibility with regards to reaching within the test section to either modify or replace an experimental set up. Figure 32 is a comprehensive image detailing the hinge lines or the axis from which the windows can open. The middle window does contain a hinge line but it is not really accessible due to the middle support structure. A relatively strong middle support was essential but it was also a requirement to allow for a simple way to open and close most of the windows, hence why this small, seemingly random window is present. Counting from the left the first and fifth windows are identical in size, same situation for the second and fourth windows. Acrylic is a brittle material and when it is cut it is sometimes difficult to machine to the precise or desired measurement. It was concerning that the windows would not meet side-by-side in a perfect manner. As a result acrylic pieces were made to bolt on to the windows so that it would lower the probability of air escaping during

operation. These can be seen circled in green on figure 27. The isometric angle makes them more visible.

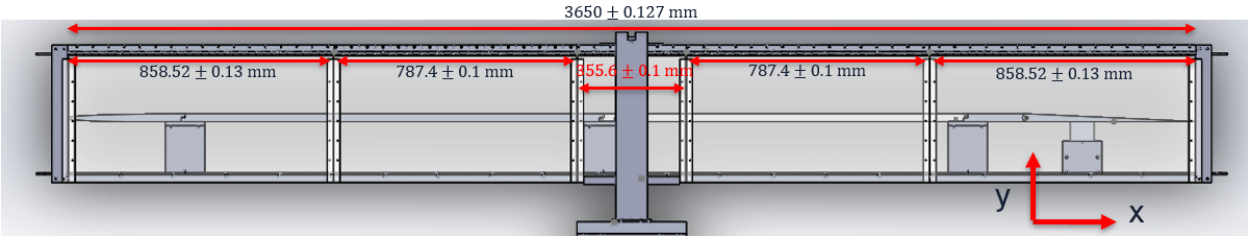

Figure 32: Streamwise Detailed View of The Hinges

Figure 28 shows windows four and five opened, so treating the angle between the hinge and the window when it is closed as depicted on figure 32 as zero, the window can easily open past 180 degrees. Once again, figure 28 shows the gap which mandated a specific profile for the windows to allow the window to fit, and thus minimize the escape of air from within the test section, mitigating the presence of a pressure gradient. Figure 33 below shows the profile of the windows. It shows the cross section of the WT and the view is facing downstream.

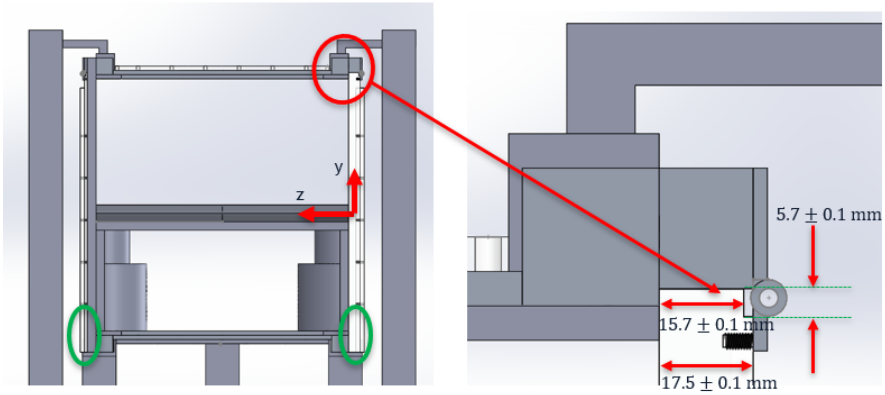

Figure 33: Cross Sectional View of The Hinges Profiles

A concern regarding operation dealt with the windows vibrating or possibly opening and closing while the wind tunnel was running. Vibration and the natural frequency of the windows will be addressed in chapter 4. Furthermore, a latch system was purchased from mcmaster. Each window was assigned two latches (except for the middle window). These latches contained a hook which can be seen on figure 34a and this enabled the use of supplemental ropes to raise the windows to facilitate getting into the test section. The heaviest window which are the largest and longest on figure 32 were approximately 7.25 kgs, each window had two latches and each latch was designed to withstand 227 kgs, so the latches chosen were definitely strong enough to hold the windows open. The latches were placed an even distance from each other relative to the middle location of the window. Figure 34c shows some of the acrylic window covered with paper to protect the surface from being scratched. Furthermore, on figure 34a the main body of the toggle latch is screwed on to the acrylic, machine screws were used because of their greater strength. The complement of the main body was screwed to the main supporting beams, at a 90 degree angle relative to the toggle latch, which is red on figure 34a. Figure 34b shows hooks that were placed on the support beam and these allow the orange bungee cords to be attached across to the other side which were hooked on to the latch as it can be seen on figure 34c. In addition, these screws also allowed for the pressure tubing to be raised so they are above the floor, to avoid damage and a tripping

hazard, but more importantly they go out of the region of interest when the cameras and lasers are acquiring data, so in essence they serve a dual purpose. These hooks are designed to withstand 11.3 kgs.

(a) Toggle Latch Setup

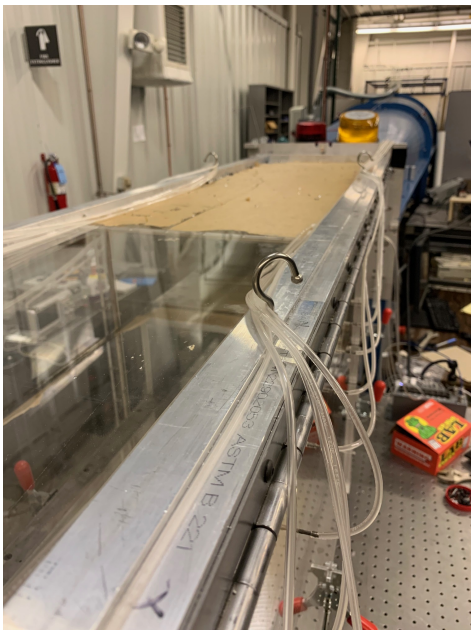

(b) Screw-in Hooks for Window Opening

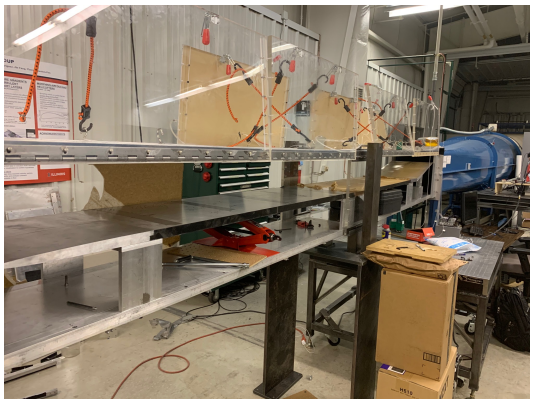

(c) Opening of Windows

Figure 34: Latches and Hook with Opened Acrylic Windows

2.5.2 Wind Tunnel Aperture for Different Boundary Conditions

This subsection exemplifies another region of flexibility regarding the alteration of a boundary condition. Figure 31 provides an overhead view of the wind tunnel and at the region of interest in the aft region of the roof, there is an outline for a hole. This aperture allows for the inclusion of different boundary conditions. This test section's main goal was to allow the study of turbulent boundary layers, and the flat plate was designed to allow a negligible pressure gradient while the flow is intended to be tripped at the leading edge to induce a a fully developed turbulent boundary layer. The purpose of this was to establish a canonical flow scenario which would serve as a baseline for future or more complex experiments. Now, in order to allow for this initial canonical flow pattern to form, the acrylic insert that can

be fitted into the hole as shown on figure 31 is shown below. Figure 35a depicts the dimensions of the insert, this view acts as if you were standing on the acrylic flat plate piece within the test section looking out. The acrylic insert is thick enough to adequately be flushed with rest of the acrylic roof piece. Figure 35b shows the acrylic insert positioned in its respective location when the tunnel is in operation. Figure 36a is an insert that was designed by Aadhy Parthasarathy, another graduate student working with TSF. The insert is mounted with two actuators that pneumatically induce the flexure of sheet metal which results in having a dynamic adverse and favorable pressure gradients. The sheet metal can be seen under the setup, it is a dark grey color that almost seems like the shadow of the rest of the components. In the figure the slots in which the actuators are able to move are also visible. The insert on figure 36b, if used, replaces the acrylic insert which is shown on figure 35a. In this configuration the laser sheet would most likely come from the side windows. This would be require a change to the set up displayed on figure 22. Fortunately, virtually the entirety of the sidewalls are acrylic which allow for many degrees of freedom to devise another way to implement PIV.

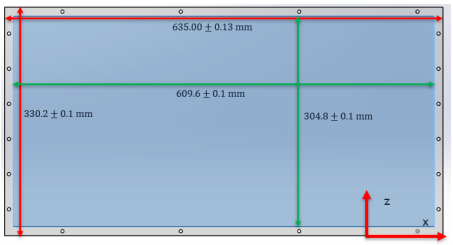

(a) Acrylic Insert

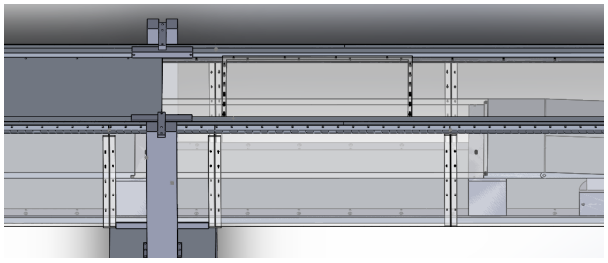

(b) Acrylic Insert in The Test Section

Figure 35: Test Section Roof Option A

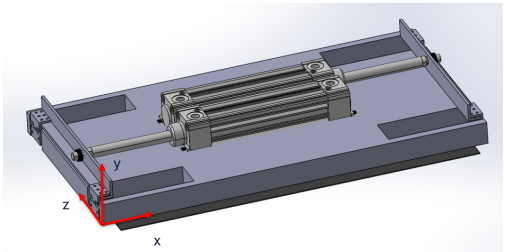

(a) Dynamic Pressure Gradient Insert

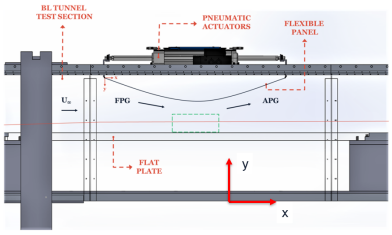

(b) Temporally Varying Pressure Gradient

Figure 36: Test Section Roof Option B [Parthasarathy, Aadhy, 2020]

FPG and APG, stand for favorable and adverse pressure gradient, respectively. The deformation rate of the ceiling on figure is at 1.7-m/s. For plot 37a, the y^* is y-spatial coordinate non-dimensionalized by the boundary layer thickness, δ. Plot 37b also shows the swift variation in the acceleration parameter K this can induce [De Graaff and Eaton, 2000]. Chapter 3 will discuss K.

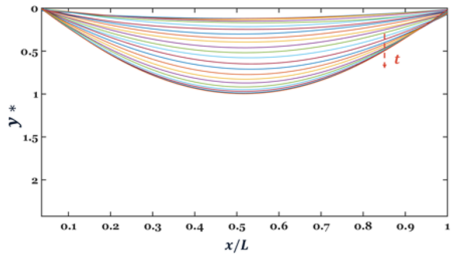

(a) Vertical Deformation Rate (.109s)

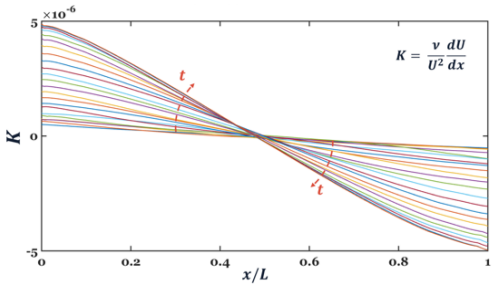

(b) Predicted K Variation Over Time (.109s)

Figure 37: Additional Capabilities and Effects of Roof Option B [Parthasarathy, Aadhy, 2020]

3 Pressure Gradients

Prior to this chapter, the need to achieve a ZPG on the TS region above the upper surface of the flat plate has been expressed several times. Before the experimental values are shown, the methodology behind obtaining theoretical estimates will be addressed. This will be followed by the information of the procedure in obtaining experimental values. This will include the instrumentation that was used to acquire static pressure measurements along the length of the TS. This was done to verify that there was a ZPG, or at least a negligible one. The end of this chapter will show ideas on tripping the boundary layer at the LE, which would help us further ensure a fully developed boundary layer.

3.1 Theoretical Estimates of The Pressure Gradient

The end goal for the design of this TS, is to study fully developed TBLs using PIV. This will be possible by tripping the BL at the LE. However, achieving a ZPG, per Blasius' prescribed flow conditions was the first task at hand. Hence, there was no BL trip on the flat plate for the characterization experiments described in this chapter. Thus, it was assumed that all four surfaces in the cross section experienced an identical development of the boundary layer (flat plate surface, two sidewalls and ceiling). For reference refer to figure 38. Flow goes from left to right in the streamwise direction. This image shows the location of the static pressure taps on the actual WT and TS. They are signaled by the red dots. The logic behind their location will be discussed in chapter 3.2.

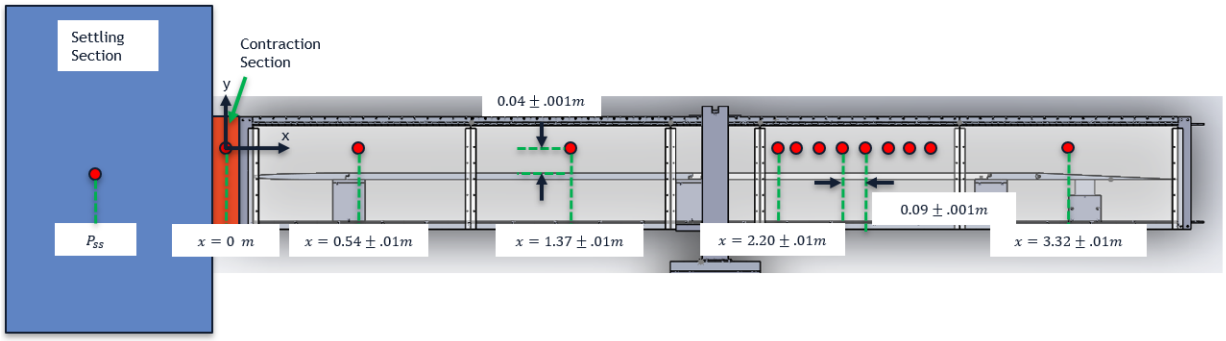

Figure 38: Pressure Tap Location on Current Test Section

In literature, the critical Reynolds number for flow over a flat plate to transition from laminar to turbulent is estimated at 500,000 [White and Corfield, 2006], the location of the transition was found using equation 1.2, $\rho U_\infty x/\mu$. The laminar boundary layer growth was characterized by, $\delta_{99,lam}$ which is equation 3.1 below. This was then superimposed by equation 2.1, $.37x/Re_x^{1/5}$, per the respective x location of the critical Reynolds number.

$$\delta_{99,lam} = \frac{4.91x}{\sqrt{Re_x}} \tag{3.1}$$

Section 2.2.1 explained the concept of displacement thickness. Equation 2.4 was the displacement thickness for a fully developed TBL. Equation 3.2 is the same quantity but for laminar flow. Similar to the boundary layer thickness the transition between the two quantities was also characterized by the critical Reynolds number of 500,000. The following plots show these quantities at different freestream speeds. The introduction to this chapter said that the

experimental pressure gradients would be compared to theoretical ones. The first three plots on figure 39 parallel the experimental flow speeds, which will be addressed in section 3.2. The fourth speed is highest velocity the WT is capable of achieving.

$$\delta^*_{lam} = \frac{1.72x}{\sqrt{Re_x}} \tag{3.2}$$

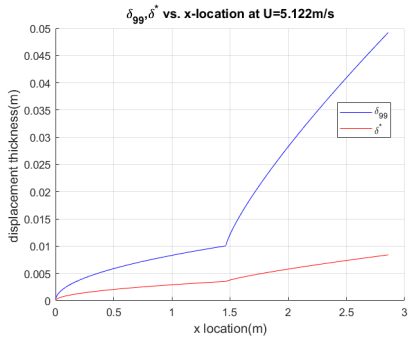

(a) δ_{99}, δ^* at U=5.122 m/s

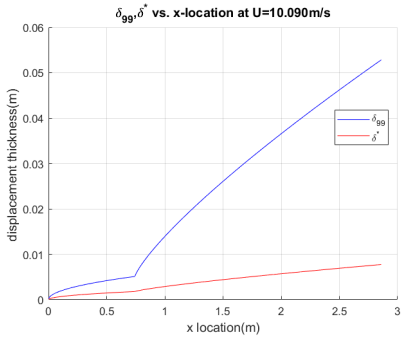

(b) δ_{99}, δ^* at U=10.090 m/s

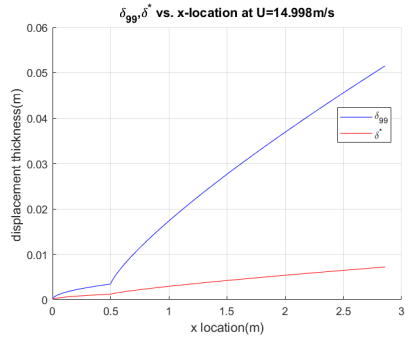

(c) δ_{99}, δ^* at U=14.998 m/s

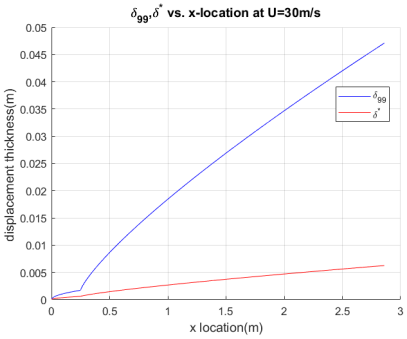

(d) δ_{99}, δ^* at U=30 m/s

Figure 39: δ_{99}, δ^* at 4 Testing Conditions

Since all of the freestream speeds are at the same order of magnitude, the y-axis or the thickness scales are similar. The inflection point, denotes the transition between the laminar and turbulent flow regimes as established by the critical Reynolds number of 500,000. The characteristic shape is constant through the three plots for both the boundary layer thickness, and the displacement thickness. The plots on figure 39 resemble the natural tripping of the boundary layer. Going from plots a, b, c and d on figure 39, the transition between laminar and turbulent flow shifts upstream as the freestream velocity increases. Furthermore, the x-axis represents the length from where x=0 to 2.86-meters, or the second to last pressure tap on figure 38. The pressure distribution was analyzed over this range because it includes the region of interest (ROI). The ROI lies where the acrylic portion is, or the fourth window on figure 38. The reason behind choosing the last pressure tap at the region of interest was because our concern was with eventually establishing canonical turbulence at the acrylic portion of the flat plate, since this is where the cameras will take images.

The A_1 and A_2 of equation 3.3 refers to the cross sectional area that flow sees from one streamwise point to another. With the former being the starting point of the region of interest. Based on equation 3.3 a reduction in A_2 relative to A_1 would inherently call for a pressure drop, ΔP, assuming the flow is steady and incompressible [Rae et al., 1999].

$$\Delta P = \frac{\rho U_\infty^2 (1 - \frac{A_2^2}{A_1^2})}{2} \tag{3.3}$$

Now, as a reminder, in wall-bounded flow viscous flow causes streamlines to shift upwards in order to comply with the conservation of mass principle. Displacement thickness is the distance that the wall would be needed to shift in the normal direction, relative to the reference plane, to allow for the same mass flow under inviscid conditions. The displacement thickness and the dimensions of the test section, allow us to find the values of A_2 and A_1 on equation 3.3.

As a reminder, the TS contains a 0.381x0.381-meter cross section, while the flat plate has a nominal thickness of .0254-m. The centerline in the x-direction of the flat plate sits at the middle portion of the WT which means that the upper half of the flat plate is in the positive y-axis location. This was important for computing the A_2 and A_1 values since the original cross section was reduced based on the actual cross sectional area on account to the presence of the flat plate and the displacement thickness. Now, in order to make the theoretical estimate more precise, on figure 38 the flat plate can be seen extending from inlet to outlet, its entire length can be seen through the acrylic windows. The flat plate does not go into the contraction section. This means that when the flow begins to develop a boundary layer, it does not build up on the flat plate immediately. The actual distance between the pressure tap on the contraction section and the LE was taken into account. This was important when the values for A_1 and A_2 were computed. Once these values were computed and the proper flow conditions were applied to equation 3.3 then the pressure drop, ΔP was computed. This value was then inputted into equation 3.4 which is the acceleration parameter K.

$$K = -\frac{\nu}{\rho * U_\infty^3} \frac{dp}{dx} \tag{3.4}$$

ν is the kinematic viscosity, ρ is the density which for this flow regime is incompressible, U_∞ is the freestream flow velocity, and the dp/dx is simply the pressure gradient. dp/dx, is ΔP from equation 3.3 divided by the distance from the second static pressure tap on figure 38 to the last pressure tap, 2.86-meters. The pressure gradient can be negligible if the K value is below 1.6E-06 [Patel, 1965], otherwise values higher than this can cause the flow to deviate substantially from the log-law which was mentioned section 1.2.1. The original form of equation 3.4 was shown by DeGraaf et al, and Patel, [De Graaff and Eaton, 2000], [Patel, 1965]. It does not contain dp/dx as it can be seen in formula 3.4, instead the K relation is $K = (\nu/U_e^2)/(dU_e/dx)$, and U_e representing the freestream velocity. The change between this equation and the 3.4 was the assumption that the flow is steady and laminar. Thus, this is a limitation of equation 3.4. This limitation stems from the fact, that there is a transition from laminar to turbulent flow between the first and last pressure tap location considered.

Figure 40 contains plots comparing the displacement thickness for fully TBLs and naturally transitioning BLs as well. The experiments which will be addressed in section 3.3 only included the latter situation. However, as a way of reference the following plot is presented. The cyan color line is the displacement thickness estimate for a fully developed turbulent boundary layer, with the trip at the LE. The dashed and joint red line is the naturally transitioning plot from laminar to the turbulent flow regime per the 500,000 Reynolds number.

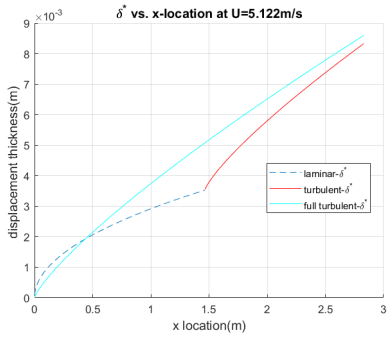

(a) δ^* at U=5.122 m/s

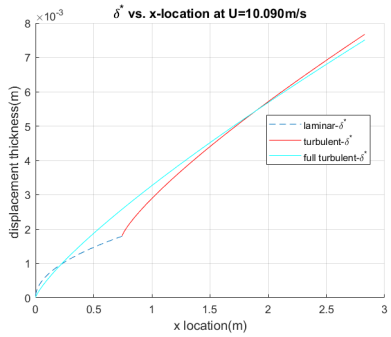

(b) δ^* at U=10.090 m/s

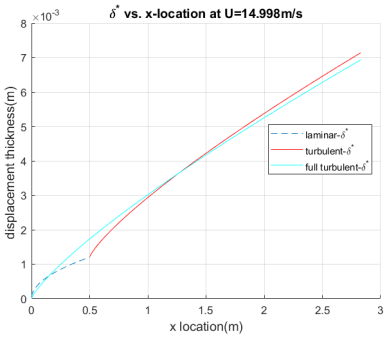

(c) δ^* at U=14.998 m/s

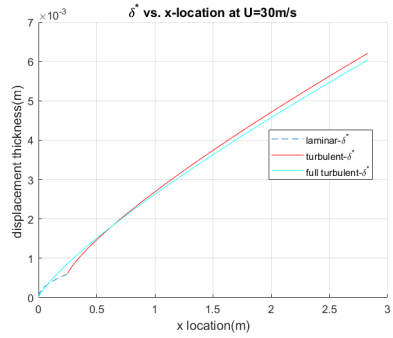

(d) δ^* at U=30 m/s

Figure 40: δ^* at 4 Freestream Conditions

3.2 Experimental Approach to Acquiring Pressure Gradients

Now, to explain the acquisition of pressure readings from a high viewpoint. When the wind tunnel starts, air begins to travel downstream. The streamlines run alongside adjacent walls which then flow into orifices where the static pressure taps are, these streamlines then flow into plastic tubes. Then the flow reaches tubulation located on the top face plate of the pressure transducers. The air then compresses a crystal within each of the channels. These compressions emit a voltage output which is then calibrated and transferred as a reading to the host computer at a rate specified by the trigger signal. These calibrations are inscribed within the memory of the pressure system. A typical method of acquiring a pressure reading, is through the use of static pressure measurements. A 9116 Netscanner pressure system was used for this campaign. These types of instruments provide a 10BaseT/100BaseT Ethernet communications for their host port, they communicate using the TCP/UDP/IP protocols as mentioned in their manual [Measurement Specialties, 2007]. These pressure scanners are capable of maintaining an accuracy up to $\pm 0.05\%$, they are capable of doing this through various simultaneous calibration capabilities. The face plate has inputs which can enable the pressure system to check for leaks as well. Furthermore, there are 16 channels each can read pressure, each orifice also has the ability to obtain reference pressure reading simultaneously to the active static pressure. However, for the purpose of these initial characterization experiments ambient conditions were used as a reference. The pressure range for this system is 2.5 kPa to 5200 kPa, it also requires a supply pressure of 550 kpa to 862 kPa. The acquisition rate chosen was 100 Hz, the voltages, pressure readings, timing sequence, freestream speed were compiled using NI LabVIEW.

The following table shows a set of experiments which were conducted on the test section. These runs were executed

without using a boundary layer trip on the flat plate, so a non-artificial transition from laminar to turbulent flow was assumed to have ensued.

	K-parameter					
Ideal: K=1.6E-06		Theory K=2.96E-06		Theory K=1.51E-06		Theory K=1.01E-06
Angle (degrees)	$U \approx 5.122 \pm .029\ m/s$	% Difference	$U \approx 10.090 \pm .038\ m/s$	% Difference	$U \approx 14.998 \pm .019\ m/s$	% Difference
1 ± 0.5	9.24E-07	68.78	2.83E-07	81.26	1.69E-07	83.27
4 ± 0.5	7.77E-07	73.75	2.40E-07	84.11	1.37E-07	86.44
6 ± 0.5	6.83E-07	76.93	1.81E-07	88.01	1.03E-07	89.80
9 ± 05	6.02E-07	79.66	1.24E-07	91.79	6.12E-08	93.94
-1.5 ± 0.5	8.64E-07	70.81	3.27E-07	78.34	1.94E-07	80.79
-3 ± 0.5	6.31E-07	78.68	3.27E-07	78.34	1.87E-07	81.49
-4 ± 0.5	4.06E-06	-37.16	2.12E-06	-40.40	1.44E-06	-42.57
-7.5 ± 0.5	5.77E-06	-94.93	3.25E-06	-115.23	2.31E-06	-128.71

Table 2: Test Plan for Initial Pressure Gradient Characterization

The left hand side of table 2 dictates the angles at which each run was executed. These refer to the angle between the middle part of the constant thickness section(s) of flat plate and the centerline of the TE, as shown on figure 17, section 2.2.4 described convention of positive and negative angles. Each angle was studied at 3 different velocities $5.122 \pm .029$ m/s, $10.090 \pm .038$ m/s, and $14.998 \pm .019$ m/s. For each case, data was acquired at 100Hz for approximately 50 seconds. At the top left corner one can find an threshold value for K [Patel, 1965]. All of the boxes in green mean that the pressure gradient at the angle and respective flow speed is negligible [Patel, 1965]. Conditions were assumed to be at STP, the University of Illinois' Aerodynamics Research Lab is a temperature controlled room, it sits at 233-meters above sea level. Each run was executed from left to right on the same row, meaning the angle was kept constant and the flow speed would ramp up, then once a steady condition was shown by the LabVIEW code, data recording would take place for about 50 seconds. Incompressibility, and steady flow were assumed. With regards to equation 3.4 the dx was constant. This was kept 2.86m, which represented the distance between the first static pressure tap taken into account for this calculation, and the last pressure tap on the region of interest (relative to the streamwise direction). The region of interest for this particular configuration is once again the acrylic portion of the flat plate.

$$U_\infty = \sqrt{\frac{2(P_{ss} - P_{ts})}{\rho(1 - \frac{A_{ts}^2}{A_{ss}^2})}} \tag{3.5}$$

A_{ss} represents the area of the settling section which can be seen in the far left of the following image. The value is $3.925 m^2$ (or $6084 in^2$). Figure 41 shows the original test section, which was 1.21m (48-inches). Now, the value for A_{ts} is $.145 m^2$ or ($225 in^2$). The stagnation or settling chamber had a pressure tap which served as P_{ss} in equation 3.5, meanwhile similarly the contraction section, P_{ts}, also had a pressure tap.

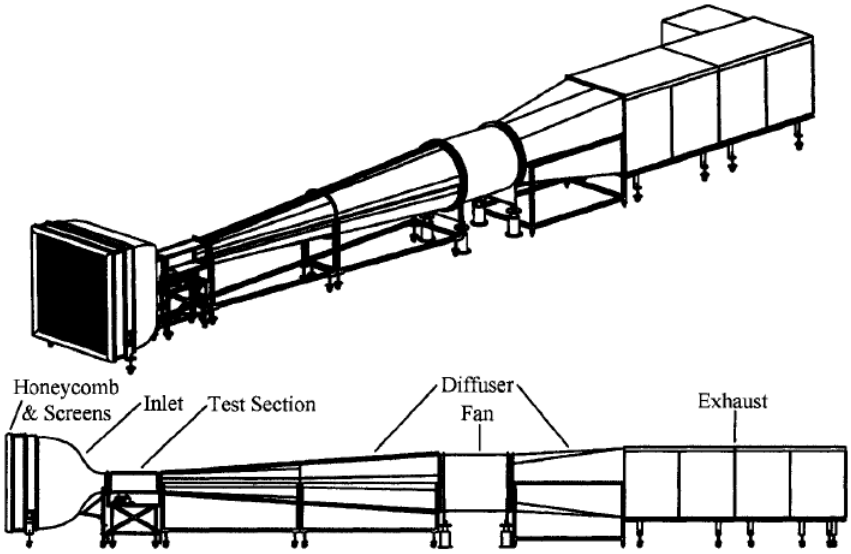

Figure 41: Model of Identical Wind Tunnel with Original Test Section [Jacobs, Jason, 2007]

Now with regards to the the pressure tap locations on figure 38. Starting from the left of the figure in the blue box is the settling section, this is not up to scale. However, immediately to the right in orange is the contraction section, followed by the scaled version of the test section. On windows 1, 2 and 5 there was a pressure tap placed in the middle of each window. The half distance between the top of the flat plate and the ceiling was halved and this is how the vertical location of the pressure tap was found, which was approximately .04m. The other side of the wind tunnel, has the exact amount of pressure taps, so what is seen pictured on figure 38 should be doubled. The fourth window contains 8 pressure taps that are spaced evenly, at approximately 0.09m in between. The methodology in which the pressure tap holes were drilled will be explained in the next section.

3.3 Static Pressure Tap Geometry

The previous two sections have expressed the importance of acquiring pressure measurements. This section will describe the way the static pressure taps were installed into the sidewalls of the TS. The number of pressure taps in the fourth window on figure 38 was obtained by averaging the pressure sensor per unit length according to different studies that looked at incompressible flow on a flat plate for both laminar and turbulent flow [Monty et al., 2011], [Oweis et al., 2010]. Once the average number of taps per unit length was acquired via these studies, then the characteristic length used in the actual tunnel was the length of the acrylic window where the region of interest on the flat plate is, which is the 787.4 ± 0.1-mm as depicted on figure 32. Earlier in this section it was mentioned that a pressure transducer was used to obtain static pressure readings, connected via tubes to static pressure holes. These static pressure holes were flushed to the sidewall of the test section, there are generally two methods of doing this, one is to drill a constant diameter hole through the entire thickness of the sidewall then have this connected to tubing that carries this reading through to the pressure transducer [Tavoularis, 2005]. This method can be seen on figure 42 below. The most significant downside to this is the counter-rotating vortices which are a result of the freestream flow making contact with the corners and subsequently the walls of the hole. This then causes an 'artificial' increase in the

static pressure that gets sent to the pressure transducer via the tubing. This configuration causes regions of high speed which then entail the increase of static pressure [Tavoularis, 2005]. On figure 42 the light blue arrow goes from left to right which represents the direction of the freestream velocity, the vorticities are in the through hole. The 17.5-mm dimension is the thickness of the acrylic window, and the reference view is an overhead view of the wind tunnel as depicted on figure 31. Figure 42 is not up to scale.

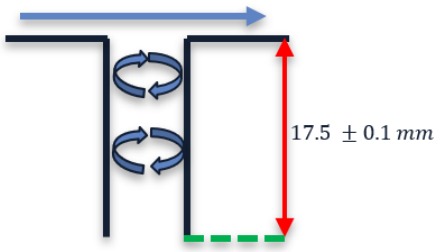

Figure 42: Classic Static Pressure Tap Design

A proposed solution to the issue with a static pressure increase would be eliminated with an infinitely small diameter. However, machining with a thin drill bit collapses upon making contact with the acrylic surface. In addition, during operation such small holes could become susceptible to impurities which would lead to blockages. The second method, which was the one adopted for this facility includes having a varying diameter through hole.

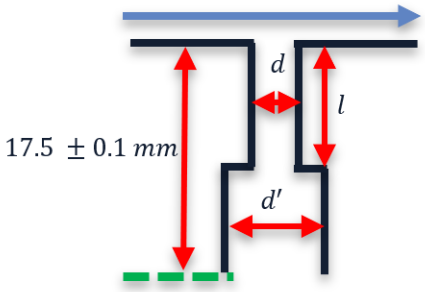

Figure 43: Pressure Tap Geometry Chosen for Current Test Section

Figure 43 depicts this geometry with the reference view being identical to that of figure 42 and ultimately figure 31. The actual dimensions of d, $d^{'}$, and l will serve as a bridge between the actual dimensions and the relations that are commonly used in literature to describe the methodology. In literature the studies that surround the different lengths and diameters are appropriately denoted as ratios. A quantity that is often used to compare the efficiency of different types of pressure taps is with the following relation, $\Delta P/\tau_w$. The relation for the denominator can be recalled at equation 1.13, this is the shear stress at the wall $\mu\partial u/\partial y$. The former or overall relation is usually plotted against a non-dimensional variable often known as the following $d^+ = d/\nu/u_\tau$ with d being the diameter of the hole that sits flush inside the TS as it was shown on figure 43. u_τ can be seen equation 1.14, $\sqrt{\tau_w/\rho}$, and ν is the kinematic viscosity of the fluid. Important takeaways from literature include as the Reynolds number increases the $\Delta P/\tau_w$ vs d^+ also increases [Tavoularis, 2005]. Studies recommend that the d should be between 0.5-mm and 3-mm. For static

pressure taps, it is also recommended that the l/d ratio should be above 1.5 using the same standard of comparison of $\Delta P/\tau_w$ vs d^+ [McKeon and Smits, 2002], as the error seen by the $\Delta P/\tau_w$ reaches an asymptote or levels off above a ratio of 1.5. Other recommendations from literature included that the l/d should not be below 5 as this often caused negative values with regards to the $\Delta P/\tau_w$, which indicated some sensitivity to shallower holes [Livesey et al., 1962]. The l/d ratio should not exceed 15 as this can cause a slower response through the tubulation and into the sensor of the pressure transducer [Franklin and Wallace, 1970]. Taking these recommendations and knowing that the thickness of the the wall was approximately 17.5-mm, the l/d ratio was chosen to be 7.14, with the d being 1-mm, this was done due to the feasibility of finding a 1-mm drill bit. The use of a 0.7-mm diameter was attempted but it was not robust enough to successfully drill into the acrylic. The outer diameter of the tubulation that is present on top of the faceplate of the pressure transducer was 1.59-mm (1/16-inches) and the outer diameter of the pressure tap or d' was 1.96-mm (.077-in). It is recommended that the d'/d relations should be above 2, however, due to the difficulty in finding appropriate tubing, this was the chosen dimension. A professional grade drill press was used to ensure the 7.14 l/d ratio. The d' dimension on figure 43 represents a 304 stainless steel piece which was cut at a length of roughly 19.05-mm. This length was done to ensure a sufficient amount would stick out of the acrylic wall in order allow for it to be fitted by the Tygon PVC tubing which would then transport the air into the pressure transducer, once it came out of the wind tunnel. The stainless steel piece was grinded down and smoothed on the exterior surface to prevent burrs especially on the corners, then the holes which were protruded on the acrylic section were also adequately cleaned out. After this, both sides of the acrylic wall were wiped down with acetone, then the 304 stainless steel pieces were placed into the d' slot as depicted on figure 43. Once this occurred they were mated to the acrylic using 5-minute epoxy glue and they were left untouched to allow for proper drying of the adhesive.

3.4 Proposed Pressure Gradient Improvements

The following section is a note on bleeding, although it is seemingly not necessary for this wind tunnel given the K values that were obtained. However, it is also an important topic that will likely be used at some point during the life of this wind tunnel, either directly to the test section, or a test article that may or may not be placed into it one day. Table 2 shows that the presence of a flat plate significantly improved the acceleration parameters, K. At a set angle, as the air speed increases, the experimental K values become smaller. For the positive angles, all of the positive angles and speeds were below the 1.6E-6 threshold and this is consistent with the recommendation placed by Hanson [Hanson et al., 2012], which was not to use negative flap angles if the objective was to reduce the pressure gradient. Now, in actuality the K-parameters that are seen on table 2 do not represent the actual conditions which will be observed during the actual testing campaigns. A tripped BL at the LE, will lead to a higher BL thickness and a higher displacement thickness. Thus, it may be needed to bleed the TS. Bleeding is a concept that refers to artificially eliminating the slow moving flow at the surface in which the fluid meets the wall. A robust technique that has been around to help with this issue for decades involves the creation of porous flat plates. The holes can be connected via tubes to a vacuum or other devices that could accurately measure the amount of mass flow which is being removed from the test section [Brunk, 1957]. One of the main issues with this is the size of the holes have to be small as to not induce such a large reduction of mass, which would lead to a pressure gradient and thus, defeat the purpose for the modification. However, the small dimension of the holes can lead to plugging. Knowing the exact location of the stagnation point at the LE would facilitate an estimate of where to place a series of bleeding regions or holes to expel mass flow here. The green circle on figure 44 shows the benefit of bleeding the TS at the LE, relative to the alternate option of bleeding at different areas along the length of the TS (red arrows).

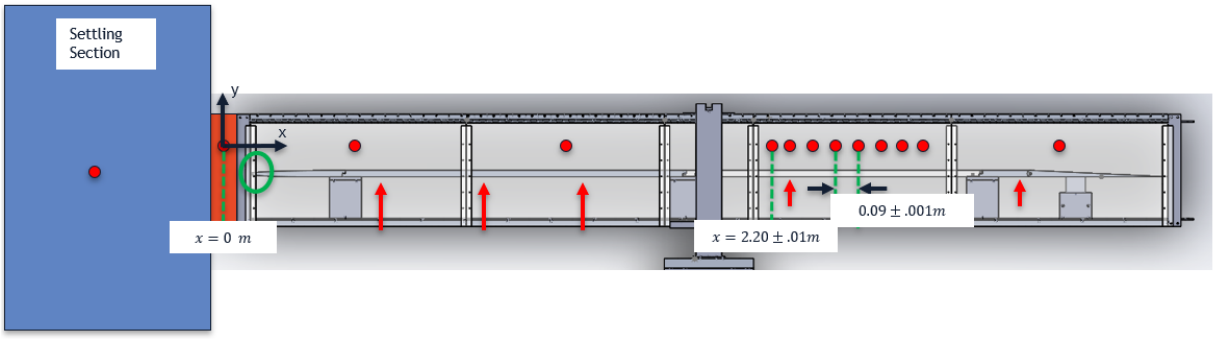

Figure 44: Proposed Bleeding Options on Current Test Sections

The benefits of having a lower number of holes would lessen the possibility of having a potential variation in the bleeding rate. Also, maintaining a constant bleed rate along the length of the TS, in conjunction with the natural BL growth along the flat plate could become complicated. There are many experimental and numerical studies that have been conducted to asymptotically simulate bleed-off [Eppler, 1978]. This information would be helpful on simulating the number, and size of holes needed to properly conduct the bleeding procedure.

3.5 Boundary Layer Trip

At the beginning of chapter 1 and 2, we mentioned how part of the goal for this facility was to study fully developed turbulent boundary layer. This inadvertently means that in order to obtain canonical turbulent flow features as prescribed by the information in section 1.2, a boundary layer trip at the LE would prove useful. The region of interest is between 2.20 and 2.83-meters relative to figure 44. For all of the conditions tested, it is apparent that this region is well past the inflection point signaling the transition to the turbulent flow regime, per figure 39. As has been mentioned several times before, this is through a natural transition from laminar to turbulent on account of the 500,000 Reynolds number. However, the LE is sensitive to perturbations which can be represented in the quality or the turbulence intensity in the aft region of the flat place in this case. There is vast amount of articles in literature which explore different avenues on the proper way of tripping the flow to artificially thicken fully developed turbulent boundary in zero pressure gradients as Klebanoff highlights [Klebanoff and Diehl, 1951]. This study actually had their experiments conducted at approximately 9-30-m/s (30-100-ft/s) on a 3.66 flat plate, very similar to the capabilities of the WT in the ARL facility, however they had a larger cross section and a variable ceiling. This study used rods of different diameters to sit perpendicular to the incoming flow, however, it was difficult to obtain undistorted flow features. They were however successful with using mesh grids that would cover the spanwise length of the flat plate and slightly hover over the LE. These mesh grids would make a 0.5 degree angle with the LE tip. The other method was using sandpaper in which one side could adhere to the flat plate. Other studies have shown that using different types of transition devices such as spherical transition trips [Gibbings et al., 1986].

Sato, [Tani and Sato, 1956] conducted a parametric study highlighting a ratio between the height of the roughness element k and the thickness of the boundary layer δ_k at a specific position x_k relative to the LE where their test were conducted. This campaign was studied using a freestream speed, U_∞, of 10-m/s and 20-m/s, once again similar to the capabilities of the TSF facility at ARL. The k/δ_k studied was 0.15, and 0.64. These variables can be seen represented

below on equation 3.6. The ν represents the kinematic viscosity. They found that: the use of roughness elements at a reasonable size (less than 1), caused the flow to separate, then upon reattachment a transition occured which was characterized by different fluctuations, some of these were sinusoidal and/or intermittent. Alternatively, they found that if the disturbance is small enough, the flow could still reattach itself, downstream as a laminar flow. Nonetheless, the differing ratios have a significant impact in the characterizing oscillations in frequency of the turbulent flow, and the roughness elements also have an evident effect on the necessary Reynolds number to cause the transition after reattachment occurs. Nevertheless, sinusoidal fluctuations were most apparent among the larger ratios.

$$\delta_k = 5.16\sqrt{\frac{\nu x_k}{U_\infty}} \tag{3.6}$$

For the facility described in this document, the use of sandpaper will be used. Given the setup of the current test section, this would avoid heavy modification to the side walls in order to place a row of objects slightly above the LE. Otherwise, it could be difficult to perfectly align, for example a rod perpendicular to the flow. Furthermore, roughness elements through the use of sandpaper have shown to be successful in tripping the flow by various studies in the community [Klebanoff and Diehl, 1951], [Gibbings et al., 1986]. The sandpaper which will first be tested, will be P16, which is what Klebanoff used, the nominal size of these roughness elements is 1.27-mm, which is consistent to the height of the objects that were used by Saito, which ranged between 0.9 and 2.0-mm [Tani and Sato, 1956]. Some studies place a rod at a position aft of the LE, however, when using sandpaper, since the grains are more sparse it is common to cut a certain thickness and have it span up to 1/6 of the entire streamwise length of the flat plate, while covering the entire width, or 0.381-meters in the case of our TS [Klebanoff and Diehl, 1951].

4 Structural Integrity

This chapter will first enumerate the major components that make up the TS, as well as their respective weight and materials. Then it will describe the methodology that was taken to ensure that the materials which make up the main supporting structures were strong enough to avoid dangerous deflection. There will be a quick note at the end of the chapter about avoiding reaching the natural frequency of the objects that are exposed to the flow.

4.1 General Overview of Mass Properties

Figure 45 shows a glimpse of the main support structure at the bottom center of the image, followed by the long beams in the streamwise or x direction. When this tunnel was being designed, it was concerning that it could be possible the weight of the tunnel would cause deflections or support structures to sag. As a result it was essential to create a table that would allow us to quantify the mass properties of the major components of the wind tunnel. The left column are the different components broken down by section, followed by the weight of each component, and then the number of times the component was used, followed by the material used.

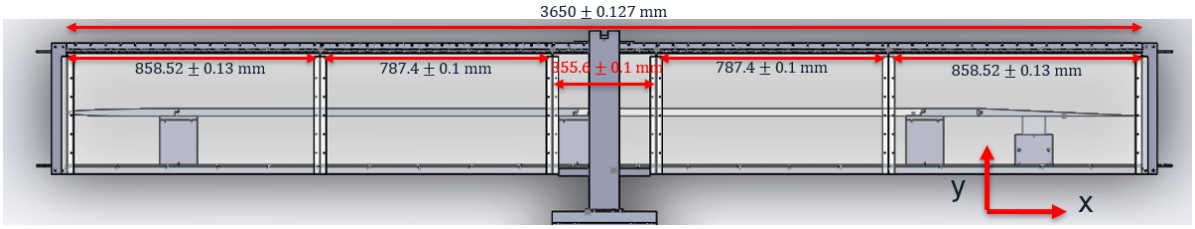

Figure 45: Support Structures

Weight of Different Componets			
Components	**Weight (Kg)**	**#-Items**	**Material**
Optics			
Large Window	7.58	4	Acrylic
Medium Window	6.98	4	Acrylic
Small Window	3.1	2	Acrylic
Acrylic Sealer	0.12	12	Acrylic
Large Hinge	0.61	4	Cast Alloy Steel
Medium Hinge	0.56	4	Cast Alloy Steel
Small Hinge	0.25	2	Cast Alloy Steel
Add-On Bar	1.24	6	6061 Al
Flat Plate & Accessories			
Flat Plate-1	4.09	1	6061 Al
Flat Plate-2	35.43	1	6061 Al
Flat Plate-3	13.71	1	Acrylic
Flat Plate-4	5.02	1	6061 Al
Flat Plate-5	7.24	2	6061 Al
C-Stand Leg	0.66	6	6061 Al
C-Stand Support	1.65	3	6061 Al
TE Lifting	2.48	2	6061 Al
WT-Main Support			
Chamber Cxn	0.81	4	6061 Al
1-Inch Beam	3.21	8	6061 Al
1/4-Inch Beam	3.596	8	Cast Alloy Steel
Ceiling & Floor - Al	20.39	3	6061 Al
Acrylic Roof	6.23	1	Acrylic
Acrylic Insert	4.43	1	Acrylic
Main Support - Steel			
Legs	92.15	2	Cast Alloy Steel
Upright Support	24.84	2	Cast Alloy Steel
Main Support Structure	59.79	1	Cast Alloy Steel
Mid Plate Lower Handle	5.27	2	Cast Alloy Steel
Mid Plate Upper Handle	4.99	1	Cast Alloy Steel
Mid Plate Bar	2.21	1	Cast Alloy Steel
Main Support Foot	10.73	2	Cast Alloy Steel
Total	**627.588**		

Table 3: Test Section Mass Properties

Referring to table 3: the large window is the largest window that can be found on figure 45 (858.52 ± 0.13-mm), the medium and small window follow the same logic. The information on hinges are also those that belong to each respective window. Now the add-on bar was designed to create a gap between the ”1-Inch Beam” and the hinge, in order to allow for thickness of the window to be able to fit as it is shown on figure 46 in the zoomed in portion of the image. The add-on bar can be seen immediately above the window and behind the hinge line. The physical gap was also circled in red on figure 28. The hinge line which evidently holds the window in place had machine screws protrude through the add-on bar and into the ”1-Inch Beam” which can be located immediately to the left of the add-on bar on figure 46 in the zoomed in image.

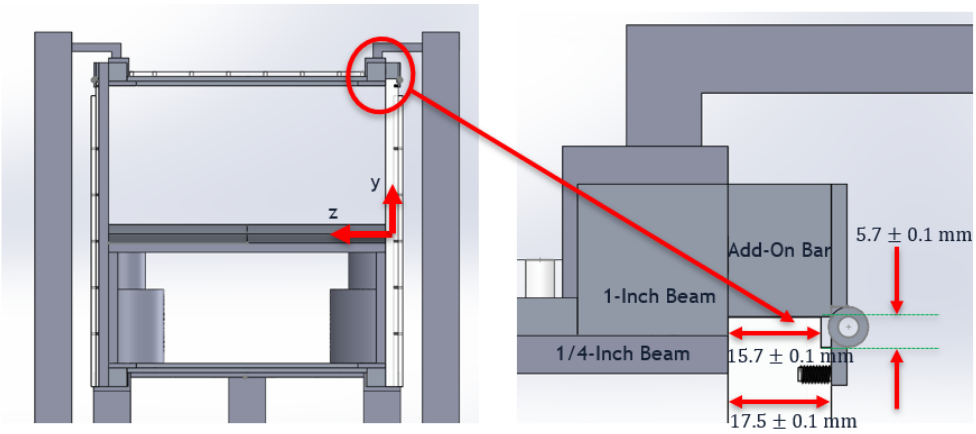

Figure 46: Cross Sectional View of The Hinges With Labels on Supporting Beams

The flat plate order on table 3 follows the same order as it was shown on figure 16. The c-stand leg(s) are the vertical structures that hold the flat plate into place, these can also be seen on figure 45. The c-stand support can be seen more clearly on figure 18 on the left side of the image. These are the most obvious immediately under the flat plate, in the spanwise direction. The TE lifting mechanism is also seen in the far right under the flat plate on figure 45, this was added after the c-stands and the flat plate (including the TE) was put into place. Its function is not essential to the support of the flat plate, but rather of holding the TE at a select angle, and keeping it from falling under its own weight.

Moving on to the next section, wind tunnel (WT) main support. The chamber connection ”Chamber Cxn” can be located far left and far right aluminum piece on figure 45, they run vertically. These connect the large acrylic window to the inlet on the left side, and the diffuser on the right side of the wind tunnel. The ”1-Inch Beam” location was described earlier in this section. The ”1/4-Inch Beam” are the longest beams which can be also seen on figure 45. They are the ones that span the farthest to the left and to the right of the test section. Their cross sectional view can be seen immediately under the ”1-Inch Beam” on figure 46 in the zoomed portion of this figure. It is also important to note that the beams that were described are held at the middle and bolted to the middle part of the test section, or the main support structure. This is more obvious on figure 31, the overhead view of the TS. The exposed ends are bolted to the inlet and diffuser, respectively. Due to these being the longest members of the test section and their importance regarding joining the test section to these ends, it was important to select the proper material as well as conduct a weight analysis to make insure that a catastrophic deflection would not occur. These will be discussed in section 4.2. The aft ceiling, aft floor and fore floor are aluminum and identical in material and dimensions they were only orientated in different ways. For this weight analysis it was assumed the roof insert was the acrylic one that was shown in section 2.5.2. Up to this point there has been mention of the main-support system, however there has not been a clear figure depiction of it. The following figure addresses this.

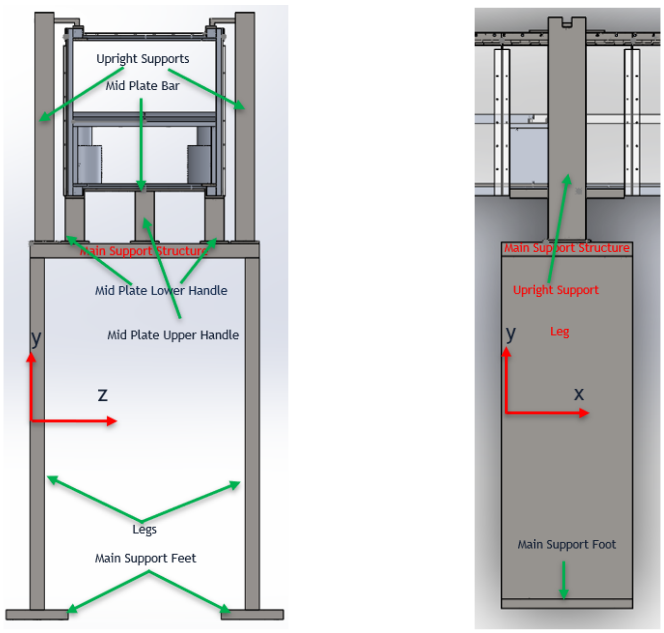

(a) Spanwise View of Support System (b) Streamwise View of Support System

Figure 47: Main Support Components

4.2 Beam Deflection and Buckling of Support Structures

In addition to the concern about the deflection "'1/4-Inch Beam(s)", the deflection of the main support structure on figure 47 was also studied, along with the buckling of the legs in the same figure. The predominant materials were pointed out on table 3, the modulus of elasticity, E, can be found in the following table.

Material	E, Modulus of Elasticity (GPa)
Aluminum 6061 Alloy	68.9
Cast Alloy Steel	200
Acrylic	2.9

Table 4: Material Properties for Wind Tunnel Support Systems [Gere and Goodno, 2013]

The approach to estimating the deflection and buckling of the beams was a bottom-up approach. For example, on figure 47a the legs evidently receive a force that is along the y-direction. Using table 3 the mass of the legs, and the feet were subtracted to obtain the critical force, P_{cr} that would cause the leg upright beam to buckle. This quantity was found using relation 4.1 which denotes the critical loads a beam for buckled mode shapes, with n=1,3, and 5, [Gere and Goodno, 2013]. L_b is the length of the beam which in this case is the length of the leg which is 935$\pm$0.1-mm, I is the moment of inertia. In order to ensure a stable central support system this calculation was assumed that the entire weight of the test section could be held up by this. However, in actuality the inlet and diffuser are bolted to the ends of the '1/4-Inch' beams whose ends were shown on figure 45. The total assumed force that is being held up by the one leg under this calculation is approximately 2062.9 newtons.

$$P_{cr} = \frac{n^2 \pi^2 EI}{4L_b^2} \tag{4.1}$$

The following table is the result is the result of assuming a buckled mode shape of $n = 1, 3$ and 5. The right-most column on table 5 is the critical load divided by the actual load, P of 2066.2 newtons.

Buckling Mode	Critical Load, P_{cr} [N]	Margin of Safety P_{cr}/P
$n = 1$	2.46E+06	1.19E+03
$n = 3$	2.21E+06	1.07+E04
$n = 5$	6.15E+07	2.98+E04

Table 5: Loading of Main Support Legs

The next concern was the deflection of the main support structure, it was assumed to be a simple pinned beam at each end, which means the ends could not travel in the y and z directions, nor in the x direction since it is simplified to a 2D problem. First, the equation for deflection, v_{dist}, was derived assuming a uniformly distributed load on account of the mass of the main support structure itself, with it being made of cast iron steel it could not be negligible. q is the uniform load that is experienced over the length, x of the main support structure, L_b.

$$v_{dist}(x) = \frac{-qx}{24EI}(L_b^3 - 2L_b x^2 + x^3) \tag{4.2}$$

Now, figure 47a shows the main support structure undergoing loads from the mid plate upper and lower handles, and the upright supports, these were simulated as point loads, with the force occurring at their center of gravity in the y-direction. The following image describes different regions that were taken into account when developing equations 4.3 to 4.9.

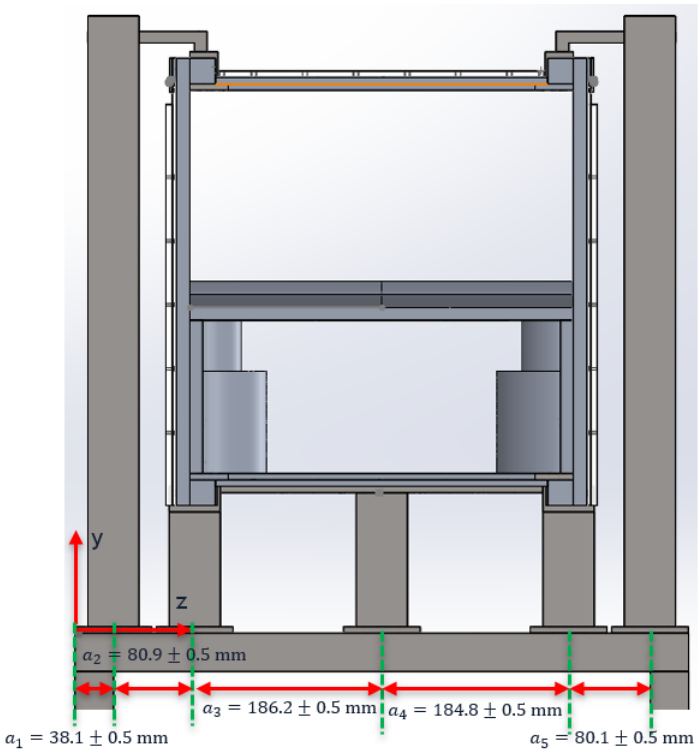

Figure 48: Load Distribution on Main Support Structure

$$C = -\frac{R_a L_b^3}{6L_b} + \frac{P(L_b - a_2^3)}{6L_b} + \frac{P(L_b - a_1^3)}{6L_b} \tag{4.3}$$

$$v_1 = \frac{R_a x^3}{6EI} + \frac{Cx}{EI} \qquad 0 \le x \le a_1 \tag{4.4}$$

$$v_2 = \frac{R_a x^3}{6EI} - \frac{P(x - a_1)^3}{6EI} + \frac{Cx}{EI} \qquad a_1 \le x \le a_2 \tag{4.5}$$

$$v_3 = \frac{R_a x^3}{6EI} - \frac{P(x - a_1)^3}{6EI} - \frac{P(x - a_2)^3}{6EI} + \frac{Cx}{EI} \qquad a_2 \le x \le a_3 \tag{4.6}$$

$$v_4 = \frac{R_a x^3}{6EI} - \frac{P(x - a_1)^3}{6EI} - \frac{P(x - a_2)^3}{6EI} + \frac{Cx}{EI} \qquad a_3 \le x \le a_4 \tag{4.7}$$

$$v_5 = \frac{R_a x^3}{6EI} - \frac{P(x - a_1)^3}{6EI} - \frac{P(x - a_2)^3}{6EI} + \frac{Cx}{EI} \qquad a_4 \le x \le a_5 \tag{4.8}$$

$$v_6 = \frac{R_a x^3}{6EI} - \frac{P(x - a_1)^3}{6EI} - \frac{P(x - a_2)^3}{6EI} + \frac{Cx}{EI} \qquad a_5 \le x \le L_b \tag{4.9}$$

Properly segmenting these relation according to the proper x values from 0 to L_b, then adding the proper intervals allows for deflection curves to be plotted. The maximum point of deflection was 4.73E-07-mm. Typically a method that is used to see if a beam is undergoing a deflection that could risk its structural integrity is to take the length of the beam and divide it by 180 [Quimby, 2008], we will call the maximum allowed deflections $\delta_{allowed,i}$. For this case $i = 1$ that value was 3.83-mm. $\delta_{max,i}$ will be the maximum point of deflection, in this case $i = 1$ this value is 4.73E-07-mm. This gives us a margin of safety (MSE_b) of 8.10E+06. Equation 4.11 summarizes this idea.

$$MSE_b = \frac{\delta_{allowed,i}}{\delta_{max,i}}, i = 1, 2, 3, 4, 5 \tag{4.10}$$

Thus, $\delta_{max,i}$ refers to the maximum deflection experienced by the select beam under the respective loads it had to carry. i is the index value indicating which maximum deflection the MSE_b is referring to. The beams that were analyzed are the following: main support structure, 1/4-Inch Beam - Fore Floor, 1/4-Inch Beam - Fore Ceiling, 1/4-Inch Beam - Aft Ceiling, 1/4-Inch Beam - Aft Floor, *i*= 2, 3, and 4, respectively. The location of physical beams can be recalled using figure 45. The $\delta_{max,2}$ deflection was based on the c-stand taken as a point load, and the weight of the beam itself was taken as a distributed load. The $\delta_{max,3}$ deflection is higher than the previous due to the higher weight of the aluminum roof and the weight of the acrylic windows. The $\delta_{max,4}$ deflection is lower than the previous due to the lower weight of the acrylic roof. The shapes of the deflection curves can be seen below on figure 49. The actual values for the maximum deflection can be found on table 6 below as well.

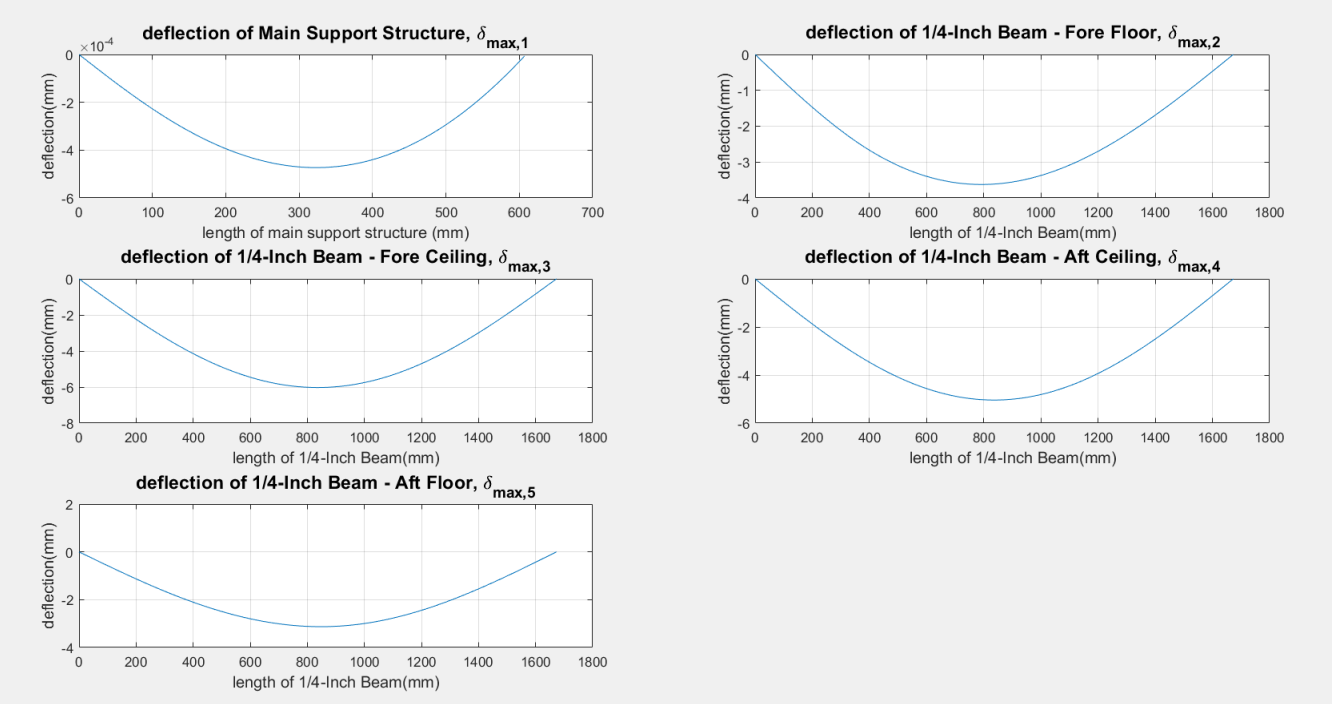

Figure 49: Deflection of Main Supporting Beams

Beam	$\delta_{allowed,i}$ [mm]	$\delta_{max,i}$ [mm]	MSE_b
Main Support Structure	3.83	4.73E-07	8.10E+06
1/4-Inch Beam - Fore Floor	9.39	3.63	2.59
1/4-Inch Beam - Fore Ceiling	9.39	6.03	1.56
1/4-Inch Beam - Aft Ceiling	9.39	5.04	1.86
1/4-Inch Beam - Aft Floor	9.39	3.13	3.00

Table 6: Deflection and MSE_b of Main Supporting Structures

Thus, all of the beams seemed to be within the margin of safety with regards to deflection. However, it is imperative to ensure that beams are stable. A stability issue could also be translated to the quality of the experiments. For example, if the ceiling pieces formed some type of tent or triangle, this could create a pressure gradient.

4.3 Window, Roof, and Ceiling Vibration

As with virtually all wind tunnels or even objects in flow, there is an inherent natural frequency. Fluid mechanics can be sensitive to different frequencies. As such, the surfaces that were exposed to flow were of interest. Given that the driving force of the tunnel is flow that gets propagated in the streamwise direction, the vibrations studied were transverse [Warburton, 1954]. Warburton defined transverse waves as the vibrations that occur perpendicular to the direction of the propagation of the waves. In the context of the test section these vibrations would be those that affect the acrylic windows, roof and ceiling pieces. The following expression was developed by Warburton [Warburton, 1954].

$$\lambda_f^2 = G_x^2 + G_y^2 \frac{a^4}{b^4} + \frac{2a^2}{b^2}[\sigma_p H_x H_y + (1 - \sigma_p) J_x J_y] \tag{4.11}$$

With regards to equation 4.11, taking a rectangle in 2-dimensions (2D), a would be the longer side relative to b. Furthermore, it was assumed that the windows, roof and ceilings were fixed on all four sides, and this can be confirmed by looking back at figure 45. Values of λ_f represent the non-dimensional natural frequency factor [Warburton, 1954]. m, n are the number of nodal lines in the x and x, as spatial coordinates. G_x, H_x, and J_x are functions of m. Furthermore, G_y, H_y, and J_y are functions of n. σ_p is Poisson's ratio. These will be shown below and they are in frequency expression. The following three relations are for the case when m and n both are equal to 2.

$$G_x = G_y = 1.56 \qquad m, n = 2 \tag{4.12}$$

$$H_x = H_y = 1.248 \qquad m, n = 2 \tag{4.13}$$

$$J_x = J_y = 1.248 \qquad m, n = 2 \tag{4.14}$$

The following relations are for when m and n are both equal to 3, 4, 5, etc.

$$G_x = m - \frac{1}{2} \qquad m = 3, 4, 5, ... \tag{4.15}$$

$$G_y = n - \frac{1}{2} \qquad n = 3, 4, 5, ... \tag{4.16}$$

$$H_x = m - \frac{1}{2}^2 [1 - \frac{2}{[(m - \frac{1}{2})\pi]}] \qquad m = 3, 4, 5, ... \tag{4.17}$$

$$H_y = n - \frac{1}{2}^2 [1 - \frac{2}{[(n - \frac{1}{2})\pi]}] \qquad n = 3, 4, 5, ... \tag{4.18}$$

$$J_x = m - \frac{1}{2}^2 [1 - \frac{6}{[(m - \frac{2}{2})\pi]}] \qquad m = 3, 4, 5, ... \tag{4.19}$$

$$J_y = n - \frac{1}{2}^2 [1 - \frac{6}{[(n - \frac{2}{2})\pi]}] \qquad n = 3, 4, 5, ... \tag{4.20}$$

All of these coefficients then get coupled into the equation 4.11, which produces the non-dimensional frequency factor, λ_f. This value can then be placed into the following relation [Warburton, 1954], which produces the actual frequency, f, which is tied to the prescribed n and m modes.

$$f = \frac{\lambda_f h \pi}{a^2} \sqrt{\frac{Eg}{48\rho_g(1 - \sigma_p^2)}} \tag{4.21}$$

In relation 4.21 the h is the thickness of the plate, E is Young's Modulus, ρ_g is the weight per unit volume, and g is the acceleration due to gravity. With this information the following plots were produced, which can be used later to verify that the harmonic frequencies which are produced by the WT do not coincide adversely with what is on the plots.

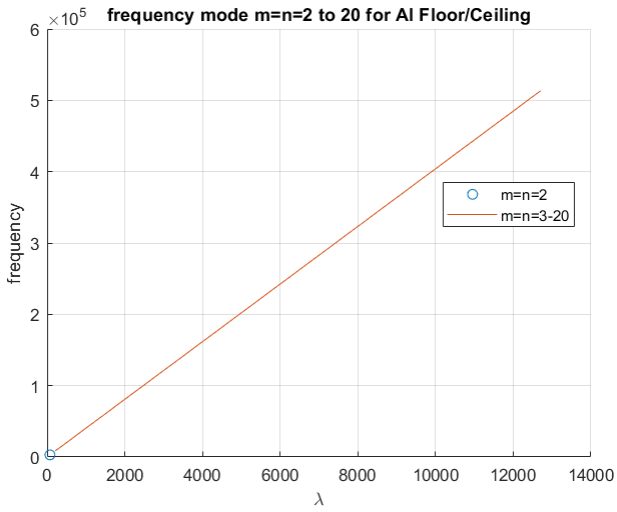

Figure 50: Natural Frequency for Aluminum Floor/Ceiling

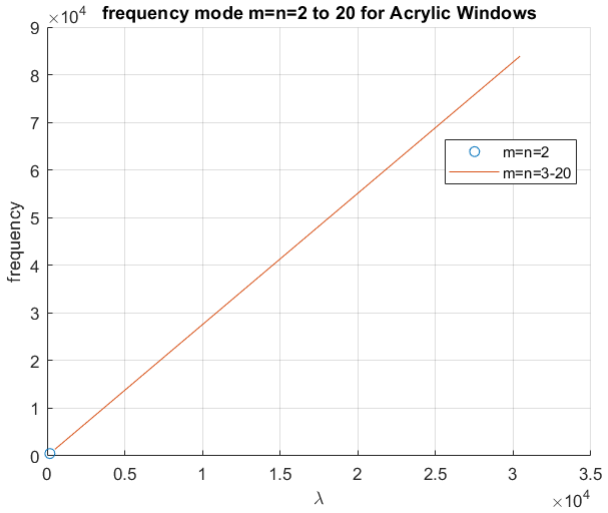

Figure 51: Natural Frequency for Acrylic Windows

5 Future Work and Recommendations

5.1 Refining Changes

The first pressure tap that was taken into account to compute both the experimental and theoretical K values or acceleration parameters of table 2 the pressure tap in the contraction section. Now, between the contraction section and the LE there would theoretically be stagnation losses, this was addressed by manipulating the location of displacement thickness that fed into the theoretical values for K. However, in order to address these changes a more robust method could be through the use or Rae and Pope's equation, 5.1, which can be seen below [Rae et al., 1999]. K_1 is the stagnation pressure losses correction coefficient. On the left side, is the dynamic pressure coefficient, which brings up another recommendation, which is to acquire a pitot tube to add an additional degree of confirmation the freestream velocity that stems from the LabVIEW code.

$$q_\infty = \frac{(p_{ss} - p_{TS,taps})(\frac{A_{TS,taps}}{A_{TS}})^2}{1 - (\frac{A_{TS,taps}}{A_{ss}})^2 - K_1} \tag{5.1}$$

Furthermore, there was a great amount of care that was taken in machining the flat plate. However, it is difficult to have a perfectly smooth surface and noting how receptive the LE flow can be to perturbations, it would be wise to acquire a profilometer to quantify the surface roughness of the flat plate. Applying to this tool to the acrylic portion of the flat plate, would also help with knowing to what degree there could be unexpected reflection of incident light into the camera [Paterna et al., 2013].

In addition, the deflection plots and information on displacement in chapter 4 was not only for insuring structural integrity but to mitigate the ceiling from causing a geometrically induced pressure gradient as a result of the cross sectional area change. A commercial leveler was used to ensure that the flat plate, roof and ceiling were leveled. However, there are more sophisticated devices that may be looked into to ensure that it is the case. Based on table 3 it was self evident that the acceleration parameters were relatively sensitive to the angle of TE, this leveler could also help verify the true zero angle of the TE, relative to the upstream part of the flat plate..

5.2 Characterizing Experiments

Furthermore, after the refining changes are executed. It would also be of great benefit to conduct PIV studies at the LE of the flat plate. Then compare these experimentally acquired velocity data to the theoretical values of figure 6, the Blasius data. Visualizing the LE with PIV may be challenging due to it being close to the inlet as shown on figure 45. However, figure 19 and section 2.3 exhibited how simple it is to swap out and shorten the flat plate if needed. It would also be necessary to obtain the turbulence intensity which can be acquired using the following relations. The fluctuating $u_i^{'}$ quantities can be decomposed by subtracting the mean velocity in each respective direction *x,y,* and z. The turbulence intensity can then be found be found and non-dimensionalized by simply dividing u^* and U^*.

$$u^* = \sqrt{\frac{1}{3}(u_x'^2 + u_y'^2 + u_z'^2)} = \sqrt{\frac{2}{3}k^*} \tag{5.2}$$

$$U^* = \sqrt{(U_x + U_y + U_z)} \tag{5.3}$$

Furthermore, equation 1.14, U_τ must also be solved for using actual PIV data. Knowing the shear stress at the wall is fundamental in verifying that the pressure gradient is truly zero. It is also another method to ensure that the canonical log-law is being followed [Von Kármán, 1931]. By obtaining velocity measurements near the wall, or even the boundary layer thickness other essential quantities such as Re_τ can also be obtained. Another prominent feature of canonical TBLs is the (-5/3) law obtained by Kolmogorov, this can be achieved by observing the energy dissipation rate in the inertial subrange region [Kolmogorov and Nikolaevich, 1962].

5.3 Small on Large Scale Interaction

After characterization is finalized, one of the first planned experiments for this test section involves introducing small scale disturbances into the already fully developed TBL using a wire or string that is present perpendicular to the direction of the flow. This wire would be held through tension above the surface of the flat plate. These disturbances would be imposed into the flow by what is known as the Von Kármán vortex street. They would appeal to the idea of modulated and modulating signals which was discussed in section 1.3. Equations, 5.4 and 5.5 are fundamental to this problem. The former is the Strouhal number St. This is a ratio between the inertial forces which are a result of the unsteadiness of the flow, to the changes in velocity between two points [White and Corfield, 2006]. f_n in this scenario is the frequency by which the disturbances propagate or move aft of the obstacle that causes it. d is the characteristic length or in this case the diameter of the wire. U_∞ is the freestream velocity.

$$St = \frac{fd}{U_\infty} \tag{5.4}$$

Equation 5.4 shows that the Strouhal number is linearly proportional to the shedding frequency, prior to the critical number of 0.2 [White and Corfield, 2006]. Then the Strouhal number becomes independent of the Reynolds at this region. The *St* remains constant as the *Re* increases. Then the plateaued region is followed by a dip in the Strouhal number. After this slight drop there is an exponential increase of St, which seems exponential in nature, this region is highly unstable. In general, shedding frequencies are a function of the inherent large scale instability of the wake or shear layer that forms aft of the body, or the wire in the context of this proposed experiment. There are natural frequencies which are associated with the structure of a cylinder. These can be excited from an external trigger such as from the force of the fluid. The fluid causes a transverse vibration onto the wire. The following relation 5.5 identifies the frequencies, f_n. K_n are the different nodes (1,2,3..) pertaining to the natural frequency of a wire in tension [Doebelin, 2010]. T is the tension which holds the wire in place. m_w/l_w represent the mass per length of the wire. The information from relation 5.5 will be studied in conjunction to the harmonic frequencies the WT emits during operation.

$$fn = K_n \frac{\sqrt{\frac{T}{\frac{m_w}{l_w}}}}{2l_w} \tag{5.5}$$

6 Conclusion

The task at hand was to lead the design, development and assembly of a 3.65-meter test section. Some main requirements were to design it in such a way that would allow access into the wind tunnel, and permit a high degree of optical access to facilitate PIV. This wind tunnel may service different types of experiments which may call for the need to swap different components. All of these concerns were addressed by having windows that can easily be lifted as shown on figure 34. All of the sidewalls are acrylic which are compatible with PIV, thus giving a high degree of freedom with regards to the different configurations an experiment can be set up, this is exemplified in figure 24. The flat plate, roof and ceilings are easily removable. Section 2.5.2 shows the ability to change some of the boundary conditions with regards to the acrylic insert. Structurally, the design as a whole was sturdy in theory, as can be seen in chapter 4, and physically it proved the same.

The main technical design requirement was to design a test section that would allow for the establishment of a fully developed TBL from a canonical viewpoint. The first step was to design a flat plate in such a way that would emulate the Blasius solutions. A 3.65-meter flat plate was planned to be tripped at the LE. This would develop a fully developed TBL, at a thickness which would facilitate PIV cameras in capturing the physics within the TBL. A flat plate and the respective LE was designed to allow incompressible, zero pressure gradient flow. This also featured a TE, with the intention that the stagnation point at the LE could be manipulated to determine the most favorable location for the boundary layer to form. Unfortunately, the effects of COVID-19 greatly affected the plans regarding characterization experiments since there was not enough time to setup and execute PIV between the time the test section was finished and the state-mandated quarantine. However, static pressure measurements were taken and the pressure gradient within the test section seemed to be negligible as determined by [Patel, 1965], [De Graaff and Eaton, 2000].

References

[Adrian et al., 2000] Adrian, R. J., Meinhart, C. D., and Tomkins, C. D. (2000). Vortex organization in the outer region of the turbulent boundary layer. *Journal of Fluid Mechanics*, 422:1–54.

[Azman et al., 2018] Azman, F. N., Lotfy, E. R., Abbas, A. A., and Harun, Z. (2018). Flow structure in modern cities: Wind tunnel investigation. *Jurnal Kejuruteraan*, 30(1):39–46.

[Bradshaw et al., 1967] Bradshaw, P., Ferriss, D., and Atwell, N. (1967). Calculation of boundary-layer development using the turbulent energy equation. *Journal of Fluid Mechanics*, 28(3):593–616.

[Brunk, 1957] Brunk, W. E. (1957). Experimental investigation of transpiration cooling for a turbulent boundary layer in subsonic flow using air as a coolant.

[Chung and McKeon, 2010] Chung, D. and McKeon, B. J. (2010). Large-eddy simulation of large-scale structures in long channel flow. *Journal of Fluid Mechanics*, 661:341–364.

[Clauser, 1954] Clauser, F. H. (1954). Turbulent boundary layers in adverse pressure gradients. *Journal of the Aeronautical Sciences*, 21(2):91–108.

[Comte-Bellot, 1976] Comte-Bellot, G. (1976). Hot-wire anemometry. *Annual review of fluid mechanics*, 8(1):209–231.

[Da Vinci, 2012] Da Vinci, L. (2012). *The notebooks of Leonardo da Vinci*, volume 1. Courier Corporation.

[Davis, 1980] Davis, M. (1980). Design of flat plate leading edges to avoid flow separation. *AIAA Journal*, 18(5):598–600.

[De Graaff and Eaton, 2000] De Graaff, D. B. and Eaton, J. K. (2000). Reynolds-number scaling of the flat-plate turbulent boundary layer. *Journal of Fluid Mechanics*, 422:319–346.

[Doebelin, 2010] Doebelin, E. (2010). *Instrumentation design studies*. Crc Press.

[Eckhardt et al., 2007] Eckhardt, B., Schneider, T. M., Hof, B., and Westerweel, J. (2007). Turbulence transition in pipe flow. *Annu. Rev. Fluid Mech.*, 39:447–468.

[Eppler, 1978] Eppler, R. (1978). Practical calculation of laminar and turbulent bled-off boundary layers.

[Finnicum and Hanratty, 1988] Finnicum, D. S. and Hanratty, T. J. (1988). Effect of favorable pressure gradients on turbulent boundary layers. *AIChE journal*, 34(4):529–540.

[Franklin and Wallace, 1970] Franklin, R. and Wallace, J. M. (1970). Absolute measurements of static-hole error using flush transducers. *Journal of Fluid Mechanics*, 42(1):33–48.

[Fransson et al., 2004] Fransson, J. H., Brandt, L., Talamelli, A., and Cossu, C. (2004). Experimental and theoretical investigation of the nonmodal growth of steady streaks in a flat plate boundary layer. *Physics of Fluids*, 16(10):3627–3638.

[Geandier et al., 2003] Geandier, G., Denis, S., and Mocellin, a. (2003). Float glass fracture toughness determination by hertzian contact: experiments and analysis. *Journal of non-crystalline solids*, 318(3):284–295.

[Gere and Goodno, 2013] Gere, J. and Goodno, B. (2013). *Mechanics of Materials, eigth ed*. Cengage Learning, Stamford, CT.

[Geurts et al., 1994] Geurts, B., Vreman, B., and Kuerten, H. (1994). Comparison of dns and les of transitional and turbulent compressible flow: flat plate and mixing layer. *Application of Direct and Large Eddy Simulation to Transition and Turbulence*, pages 1–14.

[Gibbings et al., 1986] Gibbings, J., Goksel, O., and Hall, D. (1986). The influence of roughness trips upon boundary-layer transition part 2. characteristics of single spherical trips. *The Aeronautical Journal*, 90(899):357–367.

[Goldstein and Hultgren, 1987] Goldstein, M. and Hultgren, L. S. (1987). A note on the generation of tollmien-schlichting waves by sudden surface-curvature change. *Journal of Fluid Mechanics*, 181:519–525.

[Goldstein, 1985] Goldstein, M. E. (1985). Scattering of acoustic waves into tollmien-schlichting waves by small streamwise variations in surface geometry. *Journal of Fluid Mechanics*, 154:509–529.

[Griffiths, 1968] Griffiths, J. E. (1968). Simple photoelectric laser raman spectrophotometer. *Applied Spectroscopy*, 22(5):472–476.

[Guneshasa, Hasan, 2009] Guneshasa, Hasan (2009). Boundary Layer Theory. https://web.itu.edu.tr/ guneshasa/viscous/blt.pdf. Online; accessed 28 October 2019.

[Haddad and Corke, 1998] Haddad, O. M. and Corke, T. C. (1998). Boundary layer receptivity to free-stream sound on parabolic bodies. *Journal of Fluid Mechanics*, 368:1–26.

[Hambleton et al., 2006] Hambleton, W., Hutchins, N., and Marusic, I. (2006). Simultaneous orthogonal-plane particle image velocimetry measurements in a turbulent boundary layer. *Journal of Fluid Mechanics*, 560:53–64.

[Hanson et al., 2012] Hanson, R. E., Buckley, H. P., and Lavoie, P. (2012). Aerodynamic optimization of the flat-plate leading edge for experimental studies of laminar and transitional boundary layers. *Experiments in fluids*, 53(4):863–871.

[Hinch, 1991] Hinch, E. (1991). *Perturbation methods. 1991*. Cambridge University Press.

[Hinze, 1972] Hinze, J. (1972). *Turbulence*. McGraw-Hill.

[Hutchins and Marusic, 2007] Hutchins, N. and Marusic, I. (2007). Large-scale influences in near-wall turbulence. *Philosophical Transactions of the Royal Society A: Mathematical, Physical and Engineering Sciences*, 365(1852):647–664.

[Jacobs, Jason, 2007] Jacobs, Jason (2007). Iced Airfoil Separation Measurements by Particle Image Velocimetry, PhD Thesis. https://www.ideals.illinois.edu/handle/2142/85103. Online; accessed 23 September 2018.

[Klebanoff and Diehl, 1951] Klebanoff, P. and Diehl, Z. (1951). Some features of artificially thickened fully developed turbulent boundary layers with zero pressure gradient. Technical report, National Bureau Of Standards Gaithersburg, MD.

[Kolmogorov and Nikolaevich, 1962] Kolmogorov and Nikolaevich, A. (1962). A refinement of previous hypotheses concerning the local structure of turbulence in a viscous incompressible fluid at high reynolds number. *Journal of Fluid Mechanics*, 13(1):82–85.

[Kraichnan, 1976] Kraichnan, R. (1976). J. fluid mech., 75, 657.. 1976b. *J. Fluid Mech*, 77:753.

[LaVision, 2020] LaVision (2020). Imager sCMOS. https://www.lavision.de/en/products/cameras/cameras-for-piv/. Online; accessed 22 January 2020.

[Livesey et al., 1962] Livesey, J., Jackson, J., and Southern, C. (1962). The static hole error problem. *Aircraft Engineering and Aerospace Technology*.

[Louhichi et al., 2007] Louhichi, H., Fournel, T., Lavest, J., and Aissia, H. B. (2007). Self-calibration of scheimpflug cameras: an easy protocol. *Measurement Science and Technology*, 18(8):2616.

[Lumley, 1992] Lumley, J. (1992). Some comments on turbulence. *Physics of Fluids A: Fluid Dynamics*, 4(2):203–211.

[Lyn et al., 1995] Lyn, D. A., Einav, S., Rodi, W., and Park, J.-H. (1995). A laser-doppler velocimetry study of ensemble-averaged characteristics of the turbulent near wake of a square cylinder. *Journal of Fluid Mechanics*, 304:285–319.

[Marusic et al., 2010] Marusic, I., Mathis, R., and Hutchins, N. (2010). Predictive model for wall-bounded turbulent flow. *Science*, 329(5988):193–196.

[Mathis et al., 2009] Mathis, R., Hutchins, N., and Marusic, I. (2009). Large-scale amplitude modulation of the small-scale structures in turbulent boundary layers. *Journal of Fluid Mechanics*, 628:311–337.

[McKeon and Smits, 2002] McKeon, B. and Smits, A. (2002). Static pressure correction in high reynolds number fully developed turbulent pipe flow. *Measurement Science and Technology*, 13(10):1608.

[Measurement Specialties, 2007] Measurement Specialties (2007). Model 9116 Intelligent Pressure Scanner. https://www.chell.co.uk/phpmedia/docs/9116_users_manual.pdf. Online; accessed 3 February 2020.

[Melling, 1997] Melling, A. (1997). Tracer particles and seeding for particle image velocimetry. *Measurement science and technology*, 8(12):1406.

[Monty et al., 2011] Monty, J., Harun, Z., and Marusic, I. (2011). A parametric study of adverse pressure gradient turbulent boundary layers. *International Journal of Heat and Fluid Flow*, 32(3):575–585.

[Morkovin, 1969] Morkovin, M. V. (1969). *On the many faces of transition*. Springer.

[North Carolina State Climate Office, 2016] North Carolina State Climate Office (2016). Composition of Atmosphere. https://climate.ncsu.edu/edu/Composition. Online; accessed 15 November 2019.

[Orszag, 1969] Orszag, S. A. (1969). Numerical methods for the simulation of turbulence. *The Physics of Fluids*, 12(12):II–250.

[Oweis et al., 2010] Oweis, G. F., Winkel, E. S., Cutbrith, J. M., Ceccio, S. L., Perlin, M., and Dowling, D. R. (2010). The mean velocity profile of a smooth-flat-plate turbulent boundary layer at high reynolds number. *Journal of fluid mechanics*, 665:357–381.

[Parthasarathy, Aadhy, 2020] Parthasarathy, Aadhy (2020). Effect of Unsteady Pressure Gradients on Coherent Structures in Turbulent Boundary Layers.

[Patel, 1965] Patel, V. (1965). Calibration of the preston tube and limitations on its use in pressure gradients. *Journal of Fluid Mechanics*, 23(1):185–208.

[Paterna et al., 2013] Paterna, E., Moonen, P., Dorer, V., and Carmeliet, J. (2013). Mitigation of surface reflection in piv measurements. *Measurement science and technology*, 24(5):057003.

[Perry and Mueller, 1987] Perry, M. and Mueller, T. (1987). Leading-and trailing-edge flaps on a low reynolds number airfoil. *Journal of aircraft*, 24(9):653–659.

[Platzman, 1967] Platzman, G. W. (1967). A retrospective view of richardson's book on weather prediction. *Bulletin of the American Meteorological Society*, pages 514–550.

[Quimby, 2008] Quimby, T. B. (2008). A beginner's guide to the steel construction manual. *An introduction to designing steel structures using the AISC Steel Construction Manual,*.

[Rae et al., 1999] Rae, W. H., Pope, A., and Barlow, J. B. (1999). *Low-speed wind tunnel testing*. John wiley & sons.

[Raffel and Kost, 1998] Raffel, M. and Kost, F. (1998). Investigation of aerodynamic effects of coolant ejection at the trailing edge of a turbine blade model by piv and pressure measurements. *Experiments in Fluids*, 24(5-6):447–461.

[Ragni et al., 2011] Ragni, D., Schrijer, F., Van Oudheusden, B., and Scarano, F. (2011). Particle tracer response across shocks measured by piv. *Experiments in fluids*, 50(1):53–64.

[Rengasamy and Mandal, 2017] Rengasamy, K. and Mandal, A. C. (2017). Experiments on effective tripping device in a zero pressure gradient turbulent boundary layer. 822(1):012016.

[Reynolds, 1883] Reynolds, O. (1883). An experimental investigation of the circumstances which determine whether the motion of water shall be direct or sinuous, and of the law of resistance in parallel channels. *Philosophical Transactions of the Royal society of London*, (174):935–982.

[Rieth et al., 2014] Rieth, M., Proch, F., Stein, O., Pettit, M., and Kempf, A. (2014). Comparison of the sigma and smagorinsky les models for grid generated turbulence and a channel flow. *Computers Fluids*.

[Satyanarayana and Davis, 1978] Satyanarayana, B. and Davis, S. (1978). Experimental studies of unsteady trailing-edge conditions. *AIAA Journal*, 16(2):125–129.

[Schlatter and Örlü, 2012] Schlatter, P. and Örlü, R. (2012). Turbulent boundary layers at moderate reynolds numbers: inflow length and tripping effects. *Journal of Fluid Mechanics*, 710:5–34.

[Serrin, 1967] Serrin, J. (1967). Asymptotic behaviour of velocity profiles in the prandtl boundary layer theory. *Proceedings of the Royal Society of London. Series A. Mathematical and Physical Sciences*, 299(1459):491–507.

[Stewartson, 1969] Stewartson, K. (1969). On the flow near the trailing edge of a flat plate ii. *Mathematika*, 16(1):106–121.

[Tani and Sato, 1956] Tani, I. and Sato, H. (1956). Boundary-layer transition by roughness element. *Journal of the Physical Society of Japan*, 11(12):1284–1291.

[Tavoularis, 2005] Tavoularis, S. (2005). *Measurement in fluid mechanics*. Cambridge University Press.

[Theodorsen, 1955] Theodorsen, T. (1955). The structure of turbulence. In *50 Jahre Grenzschichtforschung*, pages 55–62. Springer.

[Townsend, 1961] Townsend, A. (1961). Equilibrium layers and wall turbulence. *Journal of Fluid Mechanics*, 11(1):97–120.

[Townsend, 1980] Townsend, A. (1980). *The structure of turbulent shear flow*. Cambridge university press.

[Von Kármán, 1931] Von Kármán, T. (1931). Mechanical similitude and turbulence.

[Warburton, 1954] Warburton, G. (1954). The vibration of rectangular plates. *Proceedings of the Institution of Mechanical Engineers*, 168(1):371–384.

[White and Corfield, 2006] White, F. M. and Corfield, I. (2006). *Viscous fluid flow*, volume 3. McGraw-Hill New York.

[Wiscombe, 1980] Wiscombe, W. (1980). Improved mie scattering algorithms. *Applied Optics*, 19(9):1505–1509.

[Young, 1981] Young, A. (1981). Rayleigh scattering. *Applied Optics*, 20(4):533–535.

[Zhou et al., 1999] Zhou, J., Adrian, R. J., Balachandar, S., and Kendall, T. (1999). Mechanisms for generating coherent packets of hairpin vortices in channel flow. *Journal of fluid mechanics*, 387:353–396.

[Zhou, 2018] Zhou, L. (2018). *Theory and modeling of dispersed multiphase turbulent reacting flows*. Butterworth-Heinemann.